

THE DISCONTINUOUS ENRICHMENT METHOD FOR
MULTI-SCALE TRANSPORT PROBLEMS

A DISSERTATION
SUBMITTED TO THE INSTITUTE FOR COMPUTATIONAL
AND MATHEMATICAL ENGINEERING
AND THE COMMITTEE ON GRADUATE STUDIES
OF STANFORD UNIVERSITY
IN PARTIAL FULFILLMENT OF THE REQUIREMENTS
FOR THE DEGREE OF
DOCTOR OF PHILOSOPHY

Irina Kalashnikova

June 2011

© Copyright by Irina Kalashnikova 2011
All Rights Reserved

I certify that I have read this dissertation and that, in my opinion, it is fully adequate in scope and quality as a dissertation for the degree of Doctor of Philosophy.

(Charbel Farhat) Principal Adviser

I certify that I have read this dissertation and that, in my opinion, it is fully adequate in scope and quality as a dissertation for the degree of Doctor of Philosophy.

(Matthew F. Barone)

I certify that I have read this dissertation and that, in my opinion, it is fully adequate in scope and quality as a dissertation for the degree of Doctor of Philosophy.

(George C. Papanicolaou)

Approved for the University Committee on Graduate Studies.

Abstract

A discontinuous enrichment method (DEM) for the efficient finite element solution of advection-dominated transport problems in fluid mechanics whose solutions are known to possess multi-scale features is developed. Attention is focused specifically on the two-dimensional (2D) advection-diffusion equation $-\kappa\Delta c(\mathbf{x}) + \mathbf{a}(\mathbf{x}) \cdot \nabla c(\mathbf{x}) = f(\mathbf{x})$, the usual scalar model for the Navier-Stokes equations. Following the basic DEM methodology [1], the usual Galerkin polynomial approximation is locally enriched by the free-space solutions to the governing homogeneous partial differential equation (PDE). For the constant-coefficient advection-diffusion equation, several families of free-space solutions are derived. These include a family of exponential functions that exhibit a steep gradient in some flow direction, and a family of discontinuous polynomials. A parametrization of the former class of functions with respect to an angle parameter θ_i is developed, so as to enable the systematic design and implementation of DEM elements of arbitrary orders. It is shown that the original constant-coefficient methodology has a natural extension to variable-coefficient advection-diffusion problems. For variable-coefficient transport problems, the approximation properties of DEM can be improved by augmenting locally the enrichment space with a “higher-order” enrichment function that solves the governing PDE with $\mathbf{a}(\mathbf{x})$ linearized to second order. A space of Lagrange multipliers, introduced at the element interfaces to enforce a weak continuity of the solution and related to the normal derivatives of the enrichment functions, is developed. The construction of several low and higher-order DEM elements fitting this paradigm is discussed in detail. Numerical results for several constant as well as variable-coefficient advection-diffusion benchmark problems reveal that these DEM elements outperform their standard Galerkin and stabilized

Galerkin counterparts of comparable computational complexity by a large margin, especially when the flow is advection-dominated.

Acknowledgements

First and foremost, I would like to acknowledge my advisor, Professor Charbel Farhat. Your keen insight and fundamental questions helped me greatly to improve my work, as well as to grow as a researcher. Thank you for all your guidance, for your support, and for encouraging me to aim high.

I have been fortunate enough to have had several mentors during my graduate studies at Stanford, in addition to Professor Farhat:

- Dr. Radek Tezaur, my mentor in the Farhat Research Group (FRG). Radek, thank you for your continued mentorship during the past four years, for the regular brain-storming sessions on DEM, and for sharing with me your ideas, knowledge and experience. Thank you also for inspiring me to embark on some once-in-a-lifetime adventures in the southwest.
- Dr. Matthew Barone, my mentor at Sandia National Lab. Thank you for providing me with a unique opportunity to gain a wider breadth of research experience while still a graduate student, for introducing me to a number of interesting research areas, and for putting the national labs on my radar.
- Professor James Lambers, an additional research collaborator and former professor at Stanford. I found our collaboration, and our discussions on the mathematics of KSS and the FEM interesting and refreshing, Jim. Thank you for all the advice. I truly admire your enthusiasm for research and education.

I would like to acknowledge also:

- Stanford’s Institute for Computational & Mathematical Engineering (ICME). I knew ICME was the program for me when I visited as a prospective student during the process of choosing graduate schools. What impressed me the most – and what continues to impress me today – was the wide range of interdisciplinary research taking place here, and the genuine enthusiasm ICME students and faculty have for their work, the program, and the University. Thank you in particular:
 - Former directors, Professor Peter Glynn and Professor Walter Murray, and current director, Professor Margot Gerritsen, for your leadership and guidance.
 - ICME Student Services Coordinator, Indira Choudhury, for taking the time to answer my numerous questions about various University policies and procedures, starting before I was even a student in ICME.
- My lab mates at Stanford in the Farhat Research Group (FRG), for many valuable discussions and suggestions, and for some good times down in the basement of Durand: Radek Tezaur, Paolo Massimi, David Powell, Kevin Carlberg, David Amsallem, Jón Tómas Gretarsson, Sebastien Brogniez, Jari Toivanen, Julien Cortial, Kevin Wang, Meir Lang, Phil Avery, Edmond Chiu, Xianyi Zeng, Alex Main, Harsh Menon, Arthur Rallu, and Dalei Wang.
- My colleagues at Sandia National Lab: Jeff Payne, Basil Hassan, Matt Barone, Dan Segalman, Matt Brake, Heidi Thornquist, Larry DeChant, Steve Beresh, Katya Casper, Justin Smith, Ryan Bond, Jerry Rouse, and Rich Field. It was a pleasure to work with you, and I hope that we may continue our collaborations in the future.
- The members of my thesis oral exam committee: Dr. Matthew Barone, Professor Charbel Farhat, Professor Adrian Lew, Professor George Papanicolaou, and Professor Michael Saunders.
- The funding sources that made my Ph.D. work possible: the U.S. Department of Defense NDSEG fellowship, and the National Physical Science Consortium

(NPSC) Graduate Fellowship, funded by the Engineering Sciences Center at Sandia National Laboratories.

The friends and acquaintances who have helped me get through the various challenges in my life are too numerous to name here. Thank you for keeping me sane, and for at least pretending to understand why I chose to remain a student for twenty-two consecutive years.

Last but not least, I would like to thank my parents: Olga Firsova and Sergei Kalashnikov. Words cannot express how much I appreciate the sacrifices you have made for me. You are largely responsible for making me the person I am today.

Contents

Abstract	iv
Acknowledgements	vi
1 Introduction	1
1.1 The finite element method (FEM) in fluid mechanics	2
1.2 Alternatives to the classical Galerkin FEM for advection-dominated flow problems	3
1.3 The discontinuous enrichment method (DEM)	5
1.3.1 Comparison of DEM to other methods	6
1.3.2 History of DEM and its success	7
1.3.3 DEM for problems in fluid mechanics	8
2 Theoretical Framework of DEM	10
2.1 Functional settings and notation for a canonical advection-diffusion boundary value problem	11
2.2 Hybrid variational formulation of DEM	15
2.3 Approximation spaces in DEM	19
2.3.1 The primal approximation space \mathcal{V}^h	19
2.3.2 Babuška-Brezzi <i>inf-sup</i> condition	21
2.3.3 The dual space of Lagrange multiplier approximations \mathcal{W}^h	24
2.4 Galerkin formulation and implementation of DEM	25
2.4.1 Integration of $a(\cdot, c^E)$	26
2.4.2 Static condensation at the element level	27

2.4.3	Computational complexity	29
2.5	Linear least squares “qualifying test” for enrichment functions	30
3	Free-Space Solutions to 2D Advection-Diffusion	33
3.1	Free-space solutions to the 2D advection-diffusion equation with constant $\mathbf{a} \in \mathbb{R}^2$	33
3.1.1	Separation of variables solutions	34
3.1.2	Polynomial solutions	40
3.2	Free-space solutions to the 2D advection-diffusion equation with $\mathbf{a}(\mathbf{x}) = \mathbf{Ax} + \mathbf{b}$	44
4	Constant-Coefficient Advection-Diffusion	48
4.1	The enrichment space \mathcal{V}^E	48
4.2	The Lagrange multiplier approximation space \mathcal{W}^h	52
4.2.1	Derivation of the Lagrange multiplier approximations on an element edge	53
4.2.2	Lagrange multiplier selection and truncation	55
4.3	DGM and DEM element design	57
4.3.1	General and mesh independent element design procedure	57
4.3.2	Some 2D DGM and DEM elements for constant-coefficient advection-diffusion	58
4.3.3	Element design for $Pe \leq 10^3$	59
4.3.4	Element design for $Pe > 10^3$	60
4.4	Implementation and computational properties	62
4.4.1	Computational complexity	62
4.4.2	Analytical evaluation of element-level arrays	62
4.4.3	Selection of reference points	63
4.5	Numerical results	64
4.5.1	Homogeneous boundary layer problem with a flow aligned with the advection direction	66
4.5.2	Homogeneous boundary layer problem with a flow not aligned with the advection direction	71

4.5.3	Two-scale inhomogeneous problem	74
4.5.4	Double ramp problem on an L -shaped domain	78
5	Variable-Coefficient Advection-Diffusion	84
5.1	The enrichment space \mathcal{V}^E	84
5.2	The Lagrange multiplier approximation space \mathcal{W}^h	87
5.2.1	Exponential Lagrange multiplier approximations	88
5.2.2	Lagrange multiplier selection	90
5.3	Augmentation of \mathcal{V}^E	94
5.3.1	Augmentation of \mathcal{V}^E by polynomial free-space solutions to the 2D advection-diffusion equation	94
5.3.2	Augmentation of \mathcal{V}^E by a “higher order” enrichment function	96
5.4	DGM and DEM element design	98
5.4.1	Nomenclature and computational complexity	98
5.4.2	Lagrange multiplier selection	101
5.5	Implementation and computational properties	102
5.5.1	Analytical evaluation of element-level arrays	102
5.5.2	Scaling of enrichment functions	104
5.5.3	Interpolation of advection field	104
5.6	Numerical results	105
5.6.1	Inhomogeneous problem with a rotating advection field and an L -shaped domain	106
5.6.2	Thermal boundary layer problem	110
5.6.3	Lid-driven cavity flow problem	112
5.6.4	Differentially-heated cavity problem	119
6	Conclusions and future work	128
6.1	Summary of dissertation contributions	128
6.2	Future work	129
7	Appendix	131
7.1	Review of the classical Galerkin FEM and stabilized FEMs	131

7.1.1	The classical Galerkin finite element method (FEM)	131
7.1.2	Stabilized finite element methods	138
7.2	Free-space solutions to the constant-coefficient advection-diffusion equation in 3D	141
7.3	Free-space solutions to the 2D advection-diffusion equation with $\mathbf{a}(\mathbf{x}) = \mathbf{Ax} + \mathbf{b}$ and orthogonally diagonalizable \mathbf{A}	142
7.4	Free-space solutions to the unsteady 2D constant-coefficient advection-diffusion equation	146

List of Tables

2.1	Correspondence between the local matrices in (2.56) and the bilinear/linear forms in (2.55)	27
2.2	Computational complexity of some DGM, DEM and standard Galerkin elements (assuming a discretization into n^{el} quadrilateral elements)	31
3.1	Forms of the free-space solution c^E to $\mathbf{a} \cdot \nabla c^E - \kappa \Delta c^E = 0$	35
4.1	DGM and DEM Element Nomenclature	58
4.2	Higher-order DGM and DEM elements	60
4.3	Advection directions $\phi/\pi \in \{0, 1/6, 1/4\}$ for which $\nabla c_{ex} \cdot \mathbf{n} \in \mathcal{W}^h$ for uniform discretizations of Ω for the homogeneous boundary layer problem of Section 4.5.1	67
4.4	Homogeneous boundary layer problem of Section 4.5.1 with $Pe \leq 10^3$: relative errors in the $L^2(\Omega)$ broken norm for uniform discretizations with approximately 400 dofs (non-stabilized and stabilized Galerkin Q_1 elements vs. DGM Q -4-1 element)	68
4.5	Homogeneous boundary layer problem of Section 4.5.1 with $Pe = 10^6$: relative errors in the $L^2(\Omega)$ broken norm for uniform discretizations with approximately 400 dofs (non-stabilized and stabilized Galerkin Q_1 elements vs. advection-limited DGM \overline{Q} -4-1 element)	68
4.6	Homogeneous boundary layer problem of Section 4.5.1 with $Pe \leq 10^3$: relative errors in the $L^2(\Omega)$ broken norm for uniform discretizations with approximately 400 dofs (non-stabilized Galerkin vs. DGM elements)	70

4.7	Homogeneous boundary layer problem of Section 4.5.1 with $Pe \leq 10^3$: relative errors in the $L^2(\Omega)$ broken norm for unstructured discretizations with approximately 400 dofs (non-stabilized Galerkin vs. DGM elements)	71
4.8	Homogeneous boundary layer problem of Section 4.5.1 with $Pe = 10^6$: relative errors in the $L^2(\Omega)$ broken norm for unstructured discretizations with approximately 400 dofs (non-stabilized Galerkin vs. advection-limited DGM elements)	71
4.9	Homogeneous boundary layer problem of Section 4.5.2 with $\phi = \pi/7$ and $Pe \leq 10^3$: relative errors in the $L^2(\Omega)$ broken norm for unstructured discretizations with approximately 1,600 dofs (non-stabilized Galerkin vs. DGM elements)	73
4.10	Homogeneous boundary layer problem of Section 4.5.2 with $\phi = \pi/7$ and $Pe = 10^6$: relative errors in the $L^2(\Omega)$ broken norm for unstructured discretizations with approximately 1,600 dofs (non-stabilized Galerkin vs. advection-limited DGM elements)	74
4.11	Convergence rates on unstructured meshes for the homogeneous boundary layer problem of Section 4.5.2 with $\phi = \pi/7$, and $\psi = 0$	75
4.12	Inhomogeneous boundary layer problem of Section 4.5.3 with $Pe \leq 10^3$: relative errors in the $L^2(\Omega)$ broken norm for uniform discretizations with approximately 1,600 dofs (non-stabilized Galerkin vs. DEM elements)	76
4.13	Inhomogeneous boundary layer problem of Section 4.5.3 with $Pe = 10^6$: relative errors in the $L^2(\Omega)$ broken norm for uniform discretizations with approximately 1,600 dofs (non-stabilized Galerkin vs. advection-limited DEM elements)	77
4.14	Convergence rates for the inhomogeneous boundary layer problem of Section 4.5.3 with $\phi = \pi/4$	78
4.15	Double ramp problem of Section 4.5.4: relative errors in the $L^2(\Omega)$ broken norm ($Pe = 10^3$, uniform discretizations, non-stabilized Galerkin vs. DGM and DEM elements)	81

5.1	DGM and DEM Element Nomenclature	98
5.2	Enrichment spaces of the proposed DGM and DEM elements for variable-coefficient transport problems	100
5.3	Lagrange multiplier approximation spaces of the DGM and DEM elements in Table 5.2 (identified here by the number of Lagrange multiplier dofs per edge, n^λ)	101
5.4	Inhomogeneous problem of Section 5.6.1 defined on an L -shaped domain ($Pe = 10^3$): relative solution errors	108
5.5	Inhomogeneous problem of Section 5.6.1 defined on an L -shaped domain ($Pe = 10^3$): convergence rates	109
5.6	Thermal boundary layer problem of Section 5.6.2 ($Pe = 10^3$): relative solution errors	113
5.7	Lid-driven cavity flow problem of Section 5.6.3 ($\kappa = 10^{-2}$, $Pe \approx 260$): relative solution errors	117
7.1	Summary of Galerkin quadrilateral isoparametric elements: notation and convergence properties	137

List of Figures

2.1	Decomposition of domain Ω into elements Ω^e	13
2.2	Illustration of stencils for first order Galerkin and DGM elements	30
3.1	Plots of free-space solutions $c^E(\mathbf{x}; \theta_k)$ to the constant-coefficient advection-diffusion equation for Case 1 ($a_1/\kappa = 20, a_2/\kappa = 0$)	37
3.2	Plots of free-space solutions $c^E(\mathbf{x}; \theta_i)$ to the constant-coefficient advection-diffusion equation for Case 2 ($a_1/\kappa = 20, a_2/\kappa = 0$)	39
3.3	Plots of free-space solutions $c^E(\mathbf{x}; \theta_i)$ to the constant-coefficient advection-diffusion equation for Case 3 ($a_1/\kappa = 20, a_2/\kappa = 0$)	41
3.4	Plots of polynomial free-space solutions to the constant-coefficient advection-diffusion equation ($a_1/\kappa = 10, a_2/\kappa = 5$)	43
3.5	Free-space solution (3.51) for $\sigma_i \in \mathbb{R}$	47
3.6	Free-space solution (3.51) for $\sigma_i \in \mathbb{C}$	47
4.1	Graphical representation of enrichment arguments (4.3) as a circle of radius $ \mathbf{a} $ centered at $\mathbf{a} \in \mathbb{R}^2$	50

4.2	Flow at an angle ϕ over $\Omega^e = (x_j, x_{j+1}) \times (y_j, y_{j+1})$	51
4.3	Sample unstructured mesh of 100 quadrilateral elements	52
4.4	Straight edge of element Ω^{e_i} oriented at angle α^{ij}	53
4.5	Illustration of the sets Θ^c and Θ^λ that define the Q -8-2 element . . .	61
4.6	Plots of approximated and exact solutions of the homogeneous bound- ary layer problem of Section 4.5.1 with $\phi = 0$, 1,600 dofs and $Pe = 10^3$	72
4.7	Plots of approximated and exact solutions of the homogeneous bound- ary layer problem of Section 4.5.2 with $\phi = \pi/7$, $\psi = 0$, 1,600 dofs and $Pe = 10^3$	74
4.8	Convergence rates on unstructured meshes for the homogeneous bound- ary layer problem of Section 4.5.2 with $\phi = \pi/7$, $\psi = 0$ and $Pe = 10^2$	75
4.9	Convergence rates for the inhomogeneous boundary layer problem of Section 4.5.3 with $\phi = \pi/4$ and $Pe = 10^2$	78
4.10	Plots of approximated and exact solutions of the inhomogeneous bound- ary layer problem of Section 4.5.3 with $\phi = 0$, 1,600 dofs and $Pe = 10^3$	79
4.11	L -shaped domain for the double ramp problem of Section 4.5.4	80
4.12	Plots of approximated solutions of the double ramp problem of Section 4.5.4 with $Pe = 10^3$ and 1,200 elements	80

4.13	Nodal values of approximated solutions of the double ramp problem of Section 4.5.4 along the line $y = 0.25$ with 1,200 elements	82
4.14	Nodal values of approximated solutions of the double ramp problem of Section 4.5.4 along the line $y = 0.5$ with 1,200 elements	82
4.15	Nodal values of approximated solutions of the double ramp problem of Section 4.5.4 along the line $x = 0.5$ using 1,200 elements	82
4.16	Plots of approximated solutions of the double ramp problem of Section 4.5.4 along the line $x = 0.95$ using 1,200 elements	83
5.1	Locally frozen advection fields to enable the construction of enrichment functions as free-space solutions inside the two adjacent elements $\Omega^e = (x_j, x_j + h) \times (y_j, y_j + h)$ and $\Omega^{e'} = (x_j + h, x_j + 2h) \times (y_j, y_j + h)$ for an example advection field $\mathbf{a}(\mathbf{x}) = (-y, x)^T$	87
5.2	$\Lambda^{e,e'}(\theta)$ for the case of a quadrilateral element — extrema are marked by circles ($a_1 = a_2 = \kappa = 1$)	92
5.3	Illustration of the Lagrange multiplier selection procedure (Algorithm 4) for $n^\lambda = 4$	93
5.4	L -shaped domain and rotating velocity field, with curved lines indicating streamlines (Section 5.6.1)	107
5.5	Inhomogeneous problem of Section 5.6.1 defined on an L -shaped domain ($Pe = 10^3$): decrease of the relative solution error with the mesh size	110
5.6	Thermal boundary layer problem of Section 5.6.2: domain and boundary conditions	111
5.7	Thermal boundary layer problem of Section 5.6.2 $\left(Pe = 10^3, h = \frac{1}{30} \right)$: front views of the computed solutions	114
5.8	Thermal boundary layer problem of Section 5.6.2 $\left(Pe = 10^3, h = \frac{1}{30} \right)$: rear views of the computed solutions	115
5.9	Domain, boundary conditions and $\mathbf{a}(\mathbf{x})$ for the lid-driven cavity flow problem of Section 5.6.3	116

5.10	Components a_1 and a_2 of the advection field for the lid-driven cavity flow problem of Section 5.6.3	116
5.11	Solution plots $c(\mathbf{x})$ to the advection-diffusion equation for the lid-driven cavity flow problem of Section 5.6.3 ($\kappa = 0.005$ and 40×40 uniform mesh)	119
5.12	Lid-driven cavity flow problem of Section 5.6.3: decrease of the relative solution error with the mesh size ($\kappa = 0.01$, $Pe \approx 260$) for the pure DGM elements	120
5.13	Lid-driven cavity flow problem of Section 5.6.3: decrease of the relative solution error with the mesh size ($\kappa = 0.01$, $Pe \approx 260$) for the pure DGM elements with higher order enrichment function	121
5.14	Lid-driven cavity flow problem of Section 5.6.3: decrease of the relative solution error with the mesh size ($\kappa = 0.01$, $Pe \approx 260$) for the true DEM elements	122
5.15	Domain, boundary conditions and $\mathbf{a}(\mathbf{x})$ for the differentially-heated cavity problem of Section 5.6.4	122
5.16	Components a_1 and a_2 of the advection field for the differentially-heated cavity problem of Section 5.6.4	123
5.17	Differentially-heated cavity problem of Section 5.6.4: decrease of the relative solution error with the mesh size ($\kappa = 2.22 \times 10^{-5}$, $Pe \approx 1530$) for the true DEM elements	123
5.18	Differentially-heated cavity problem of Section 5.6.4: decrease of the relative solution error with the mesh size ($\kappa = 2.22 \times 10^{-5}$, $Pe \approx 1530$) for the pure DGM elements	124
5.19	Contours of advection-diffusion solution $c(\mathbf{x})$ for the differentially-heated cavity problem of Section 5.6.4 ($\kappa = 2.22 \times 10^{-5}$, $Pe \approx 1530$, 16×16 uniform mesh)	125
5.20	Differentially-heated cavity problem of Section 5.6.4: decrease of the relative solution error with the mesh size ($\kappa = 2.22 \times 10^{-5}$, $Pe \approx 1530$) for the pure DGM elements with higher order enrichment function	126

7.1	Bilinear quadrilateral element Q_1 domain and local node ordering in the parent domain (left) and in the physical domain (right)	137
7.2	Shape functions of the bilinear quadrilateral Q_1 element	139
7.3	Azimuth and inclination angles specifying a 3D advection direction field $\mathbf{a} \in \mathbb{R}^3$	142
7.4	Plots of free-space solutions to (7.40) of the form (7.66) for different values of θ_i	146

Chapter 1

Introduction

The *Navier-Stokes equations* are the fundamental *partial differential equations* (*PDEs*) in fluid mechanics. These celebrated equations are useful in modeling many physical phenomena of interest in modern day science and engineering applications. For example, they can help with the design of aircraft and cars, as they are often used to model air flow around such vehicles. They can also be used to model the weather, ocean currents, flow in a pipe or cavity, among many other things. Obtained by considering the mass, momentum, and energy balances for an infinitesimal control volume over which these principles apply, the equations describe the velocity, pressure, temperature and density of a moving fluid. In dimensionless form, assuming an incompressible Newtonian fluid, they state that the fluid velocity $\mathbf{u} \in \mathbb{R}^d$, for $d = 1, 2, 3$ spatial dimensions, and the fluid pressure p satisfy

$$\begin{aligned} \frac{\partial \mathbf{u}}{\partial t} + \mathbf{u} \cdot \nabla \mathbf{u} + \nabla p - \frac{1}{Re} \Delta \mathbf{u} &= \mathbf{f}, \\ \nabla \cdot \mathbf{u} &= 0, \end{aligned} \tag{1.1}$$

where Re is a dimensionless parameter known as the *Reynolds number*, and $\mathbf{f} \in \mathbb{R}^d$ is a vector of body forces.

Because the Navier-Stokes equations are, in practice, too difficult to solve using analytic techniques, engineers and applied mathematicians have devoted a tremendous effort to developing numerical methods to solve these equations approximately

on a computer. The branch of fluid mechanics that uses numerical methods and algorithms to solve and analyze fluid problems is known as *Computational Fluid Dynamics* (*CFD*). Examples of some common numerical techniques in CFD, each with its own strengths depending on the application, include *spectral methods* [2, 3], *finite difference methods* [4], *finite volume methods* [5], and *finite element methods* [6, 7, 8, 9, 10, 11, 12].

1.1 The finite element method (FEM) in fluid mechanics

The method developed in this dissertation falls in the family of numerical methods known as finite element methods. The standard Galerkin finite element method is based on a variational framework (or weak formulation), and a continuous, piecewise polynomial, Galerkin approximation. Since it was first developed in the field of structural engineering during the 1940s, the Galerkin finite element method has been applied to solve complicated engineering problems in a plethora of structural (e.g., stress analysis, buckling, vibrational analysis) as well as non-structural (e.g., heat transfer, fluid flow, distribution of magnetic potential) applications [9]. One of the main advantages of the FEM over other methods is its ability to handle very complex geometries and varied boundary conditions. In addition, the theoretical framework and approximation properties of the standard Galerkin FEM is at the present time well established. It can be shown that the approach is optimal for the Laplace operator in the sense that it minimizes the error in the energy norm. This property assures good performance of the computation for elliptic problems at any mesh resolution; in other words, the method gives high coarse-mesh accuracy.

In deciding how to begin the task of building an accurate and efficient finite element method for the Navier-Stokes equations, it is useful to write down a discretization of these equations, and remark that the *advection-diffusion equation*

$$\underbrace{-\kappa\Delta c(\mathbf{x})}_{\text{diffusion}} + \underbrace{\mathbf{a} \cdot \nabla c(\mathbf{x})}_{\text{advection}} = f(\mathbf{x}), \quad \mathbf{x} \in \Omega \subset \mathbb{R}^d, \quad d = 1, 2, 3, \quad (1.2)$$

arises in its vector form in the linearization steps of the discretization. This observation suggests that having a method that can solve the much simpler transport problem (1.2) accurately and efficiently is essential to fluid mechanics applications.

It is well known that the standard FEM can be inadequate when applied to (1.2) in certain regimes. The character of the solutions of (1.2) depends on the magnitude of a dimensionless parameter known as the the **Péclet number** (Pe). The Péclet number is defined by

$$Pe \equiv \frac{\text{rate of advection}}{\text{rate of diffusion}} = \frac{l_{\Omega} \max_{\mathbf{x} \in \Omega} \|\mathbf{a}(\mathbf{x})\|}{\kappa} = Re \cdot \begin{cases} Pr & \text{(thermal diffusion)} \\ Sc & \text{(mass diffusion)}, \end{cases} \quad (1.3)$$

where Re , Pr and Sc are the Reynolds, **Prandtl** and **Schmidt** numbers respectively, l_{Ω} is a characteristic length scale of the domain Ω on which the problem is posed and $\|\cdot\|$ is some vector norm. At low values of Pe , diffusion dominates and the equation is close to the elliptic Laplace equation. As $\kappa \rightarrow 0$ ($Pe \rightarrow \infty$), however, the exact solutions of **boundary value problems (BVPs)** based on (1.2) exhibit boundary layers, much like solutions to the Navier-Stokes equations in the high Reynolds number regime. A **boundary layer** is a very narrow region, typically near a physical boundary or corner and having a width of $\mathcal{O}(Pe^{-1/2})$ [13], where the solution and its derivatives change abruptly. In order to resolve the boundary layers that can form using standard Galerkin piecewise polynomial finite elements, the mesh size would have to be the same size as the ratio between the diffusion and convection [14]. In many applications, this requirement leads to a huge number of degrees of freedom (dofs), making the FEM not only inefficient, but sometimes simply unfeasible.

1.2 Alternatives to the classical Galerkin FEM for advection-dominated flow problems

A number of different finite element approaches have been proposed for addressing the challenge of solving (1.2) accurately and efficiently in the high Pe regime. These alternatives to the standard FEM fall roughly into two categories: those based on a

modified variational formulation, and those based on a modified finite element basis. These methods are described briefly below.

One popular class of alternatives that falls into the first category of the methods described above is the class of so-called *stabilized finite element methods*. Some examples of stabilized finite elements methods are:

- The *Streamline Upwind Petrov-Galerkin (SUPG, or Streamline Diffusion)* method [15, 16, 6].
- The *Spotted Petrov-Galerkin (SPG)* [17].
- The *Galerkin Least-Squares (GLS)* Method [18, 19].
- The *Unusual Stabilized Finite Element Method (USFEM)* [20, 21].
- The *Conformal Petrov-Galerkin (CPG)* method [22, 23].

The basic idea of stabilized methods is to add weighted residual terms, representing numerical (or artificial) diffusion, to the standard weak formulation of the problem in order to enhance stability without losing consistency. The modification to the standard Galerkin FEM is in the variational formulation only, as stabilized methods rely on the same polynomial basis functions as those employed in the standard FEM.

In contrast with the first category of alternatives to the standard FEM, the second category is essentially based on non-standard finite element bases. Examples of methods that fall into this second category of methods are:

- The method of *Residual-Free Bubbles (RFB)* [24, 14].
- The *Partition of Unity Method (PUM)* [25, 26].
- *Variational Multi-Scale Methods (VMS)* [27].
- *Discontinuous Galerkin Methods (DGMs)* [28, 29, 30, 31, 32, 33, 34].

The former three methods are conforming methods: the finite element spaces employed in these methods are constructed so that the solution produced by the methods is automatically continuous. In contrast, DGMs constitute a class of finite element

methods that use *discontinuous* functions to approximate the solution. The continuity of the solution in these methods is often enforced weakly using a framework in which appropriate numerical fluxes are defined and computed on the element boundaries [30, 31, 32]. DG methods can provide great advantages in solving problems with solutions that exhibit shocks or discontinuities.

Remark 1.2.1. *Although the two “classes” of methods described above are presented as fundamentally different, there is a deep connection between some of the methods in the former and the latter categories; cf. [35] for connections between multi-scale formulations and stabilized FEMs, and between RFB and stabilized FEMs.*

Remark 1.2.2. *Note also that methods that cannot easily be placed into either one of the two “classes” described above have been proposed. For instance:*

- *The **Scharfetter-Gummel**, or exponential-fitting, method, based on a change of variables that transforms the advection-diffusion equation (1.2) into a variable-coefficient Poisson equation [36].*
- *Methods which use asymptotic analysis to construct approximate problems for (1.2) in the streamline coordinates [13].*
- *The recently-proposed DG Petrov-Galerkin method, based on “optimal” discontinuous test functions that are computed for each given BVP and guarantee stability by effectively incorporating an upwind effect into the design of the test function space [37].*

1.3 The discontinuous enrichment method (DEM)

The method developed in this dissertation, referred to as the *discontinuous enrichment method (DEM)*, falls into the second class of alternatives for the finite element solution of (1.2) in an advection-dominated regime described above, namely those in which *non*-standard finite element bases are constructed for approximating the solution. DEM was motivated by PUM, RFB, the Finite Element Tearing and Interconnect (FETI) method for non-conforming domain decomposition with Lagrange

multipliers [38, 39, 40, 41], as well as the work on discontinuous Galerkin methods (DGMs) for second-order equations [28, 29, 42, 43]. The main idea of DEM is to enrich the standard piecewise polynomial approximations by the non-conforming and in general *non*-polynomial space of free-space solutions of the homogeneous form of the governing PDE, obtained in analytical form using standard techniques such as separation of variables. Since these functions are related to the problem being solved, they have a natural potential for effectively resolving sharp gradients and rapid oscillations when these are present in the computational domain. However, since the functions are not required to satisfy any local boundary conditions that would ensure inter-element continuity, the method is by construction discontinuous; inter-element continuity in DEM is enforced weakly using Lagrange multipliers. Due to this formulation, DEM can be characterized as a *hybrid finite element method*: an FEM with two unknown fields, a primal field and a secondary field, with the secondary field defined on the element interfaces [12].

1.3.1 Comparison of DEM to other methods

The discontinuous enrichment method distinguishes itself from the methods that motivated it in several ways. Whereas RFB and PUM are continuous methods, DEM is, by construction, discontinuous. Unlike in PUM, the enrichment in DEM is performed in an additive rather than multiplicative manner. Unlike in RFB, it is *not* constrained to vanish at the element boundaries and therefore can propagate its beneficial effect to the neighboring elements. Unlike in both PUM and RFB, the enrichment in DEM leads to a discontinuous, rather than a continuous, approximation in which the enrichment dofs can be eliminated at the element level by a static condensation. This reduces the computational complexity of the method, and alleviates some of the ill-conditioning that is inherent to most enriched methods – for example, PUM, known to suffer from severe ill-conditioning that can make the method ineffective in practice [44, 1, 45]. The definition of the enrichment in DEM also allows the method to circumvent both the difficulty in approximating the global fine-scale Green’s function of VMS [27], and the loss of global effects suffered by RFB methods

because of the requirement that the bubble functions have a vanishing trace on the element boundaries. Although DEM can be classified as a discontinuous Galerkin method (DGM), DEM distinguishes itself from earlier [28, 29] as well as recently proposed [33, 34, 30, 31, 32, 37] DG methods either by its special shape functions, which are typically non-polynomial, and/or by the Lagrange multiplier degrees of freedom (dofs) it introduces at the element interfaces to enforce a weak inter-element continuity of the numerical solution.

1.3.2 History of DEM and its success

DEM was first proposed approximately ten years ago by Farhat *et al.* [1]. Initially, the method was developed for the Helmholtz equation, $\mathcal{L}u = -\Delta u - k^2 u = f$, which describes acoustic vibrations in a fluid medium. Since the Helmholtz operator tends to lose ellipticity with an increasing wave number k , the Galerkin solution of Helmholtz problems is tainted by spurious dispersion in the upper end of the low-frequency regime, and is intractable in the medium and high frequency regimes.

Since it was first proposed, the discontinuous enrichment method has matured in the following areas.

- Acoustic scattering (the Helmholtz equation) [46, 47].
- Wave propagation in elastic media (Navier’s equation) [48, 49].
- Fluid-structure interaction problems (coupling of Navier’s equation and the Helmholtz equation) [50].

For these applications, the enrichment spaces consist of a superposition of plane and/or evanescent waves. In general, it was found that DEM can achieve the same accuracy as the p -finite element method [51] using a similar computational complexity but with much fewer dofs. In [46], a family of three-dimensional (3D) hexahedral DEM elements of increasing order of convergence was proposed for the solution of acoustic scattering problems in the medium frequency regime. When compared with standard high-order polynomial Galerkin elements of comparable convergence order, the DEM elements achieved the same solution accuracy using, however, four to eight times

fewer dofs, and most importantly, *up to 60 times less CPU time* [46]. More recently, a domain decomposition-based iterative solver for 2D and 3D acoustic scattering problems in medium/high frequency regimes has been developed, and shown to be superior to the classical high-order finite element method [47]. This solver was shown to be numerically scalable with respect to the mesh size as well as the number of enrichment functions.

An attempt to bridge the gap between numerical experimentation and mathematical analysis was made by Amara *et al.* [52] in the specific context of the 2D low-order DGM element with four plane waves first proposed in [1] for solving 2D Helmholtz problems at relatively high wave numbers. This analysis resulted in a formal proof of the convergence of this element and revealed its theoretical order of accuracy.

1.3.3 DEM for problems in fluid mechanics

The excellent performance of DEM for acoustic scattering and wave propagation problems is the main motivation behind the present work, in which DEM is developed for constant and variable-coefficient advection-diffusion transport problems (1.2) in two-dimensions (2D). The development of this method for this equation can be viewed as a first step towards the more challenging task of building a DEM for the key equations in fluid mechanics, namely the Navier-Stokes equations (1.1). To this effect, the body of this dissertation is organized as follows:

- In Chapter 2, the hybrid variational formulation of a canonical 2D advection-diffusion boundary value problem discretized by DEM is presented. The approximation spaces for the primal unknown as well as the Lagrange multiplier approximations are defined, and an efficient implementation procedure is outlined.
- Chapter 3 focuses on the derivation of the enrichment field. Several families of enrichment functions for constant- as well as variable-coefficient transport problems are derived.
- In Chapter 4, the method is developed specifically for the equation (1.2) with

constant coefficients. Appropriate enrichment and Lagrange multiplier approximation spaces are developed, and an algorithm that makes possible the systematic design and implementation of DEM elements of arbitrary orders is described. The proposed DEM elements are evaluated on a number of challenging constant-coefficient problems.

- In Chapter 5, attention is turned to the variable-coefficient advection-diffusion equation (1.2). It is shown that the methodology developed specifically for the constant-coefficient case (Chapter 4) has a natural extension to variable-coefficient problems. It is also shown that, in the variable-coefficient scenario, the approximation can be improved by augmenting the enrichment space with additional families of free-space solutions to variants of the governing PDE, derived in Chapter 3. The DEM elements developed in Chapter 5 are evaluated on several challenging variable-coefficient problems possessing boundary, internal, and crosswind layers, and compared to their Galerkin and stabilized Galerkin counterparts.
- A summary of the method, the contributions of this dissertation, and some discussion of possible future research directions is given in Chapter 6. The development and numerical study of higher-order DEM elements is one of the novel accomplishments presented in this dissertation, which distinguishes it from prior works, namely [1, 53].
- A review of some fundamental concepts pertaining to the finite element method can be found in the Appendix (Chapter 7).

Chapter 2

Theoretical framework of the discontinuous enrichment method (DEM)

In this chapter, the theoretical framework of the *discontinuous enrichment method (DEM)* is developed. This framework is presented in the context of a specific boundary value problem (BVP) for the advection-diffusion equation (1.2). A brief review of the classical Galerkin finite element method (FEM) and some of its stabilized variants, based on the classical texts [6, 7, 8, 10, 54, 55], can be found in the Appendix (Section 7.1). For additional reading on the theoretical framework of DEM, including its formulation for other partial differential equations (PDEs) (e.g., the Helmholtz equation), the reader is referred to the journal articles [1, 56, 57, 58, 46, 48, 50] and the Ph.D. thesis of Oliveira [53].

2.1 Functional settings and notation for a canonical advection-diffusion boundary value problem

Let $\Omega \subset \mathbb{R}^d$, for $d = 1, 2$ or 3 , be an open bounded domain with a Lipschitz continuous, smooth boundary $\Gamma \equiv \partial\Omega$. As a canonical example, consider the following all-Dirichlet boundary value problem (BVP) for the advection-diffusion equation in its strong form (S).

$$(S) : \begin{cases} \text{Find } c : \bar{\Omega} \rightarrow \mathbb{R} \text{ such that } c \in H^1(\Omega) \text{ and} \\ \mathcal{L}c \equiv -\kappa\Delta c + \mathbf{a} \cdot \nabla c = f \text{ in } \Omega, \\ c = g \text{ on } \Gamma, \end{cases} \quad (2.1)$$

where $\bar{\Omega}$ denotes the closure of Ω . The diffusivity κ is assumed to be constant and positive, and the advection field $\mathbf{a}(\mathbf{x}) \in \mathbb{R}^d$ in $d = 1, 2, 3$ spatial directions is assumed to be continuous over the entire domain Ω , with its i^{th} component denoted by $a_i(x)$, for $i = 1, \dots, d$. In (2.1), $f : \Omega \rightarrow \mathbb{R}$ and $g : \Gamma \rightarrow \mathbb{R}$ are given functions specifying a source and Dirichlet data respectively, and $H^1(\Omega)$ denotes the **Sobolev space** of order one. Recall that a **Sobolev space of order m** is the (vector) space of functions

$$H^m(\Omega) \equiv \left\{ v \in L^2(\Omega) : \frac{\partial^{(i+j)}v}{\partial x^i \partial y^j} \in L^2(\Omega), 0 \leq i + j \leq m \right\}, \quad (2.2)$$

equipped with the inner product

$$(u, v)_{m,\Omega} \equiv (u, v) \equiv \sum_{i,j} \left(\frac{\partial^{(i+j)}u}{\partial x^i \partial y^j}, \frac{\partial^{(i+j)}v}{\partial x^i \partial y^j} \right)_{0,\Omega}, \quad (2.3)$$

and corresponding norm

$$\|u\|_{m,\Omega} \equiv (u, u)_{m,\Omega}^{1/2}, \quad (2.4)$$

where $L^2(\Omega)$ is the space of measurable, square integrable functions in Ω , equipped with the inner product

$$(u, v)_{0, \Omega} \equiv \int_{\Omega} uv d\Omega. \quad (2.5)$$

From this point onwards, the subscript Ω will be dropped unless the domain of integration is a subset of Ω , e.g., $\|u\|_{m, \Omega} \equiv \|u\|_m$.

The process of discretizing a linear BVP in its strong form (S), e.g. (2.1), by a finite element method (FEM) consists of the following four steps [6].

Step 1: Constructing a **triangulation** \mathcal{T}_h of the domain, that is, partitioning Ω into n^{el} disjoint **element** domains Ω^e , each with a boundary $\Gamma^e \equiv \partial\Omega^e$ (Figure 2.1), so that

$$\bar{\Omega} = \overline{\cup_{e=1}^{n^{el}} \Omega^e} \quad \text{with} \quad \cap_{e=1}^{n^{el}} \Omega^e = \emptyset. \quad (2.6)$$

Step 2: Obtaining the equivalent **weak** (or **variational**) **form** (W) of (2.1).

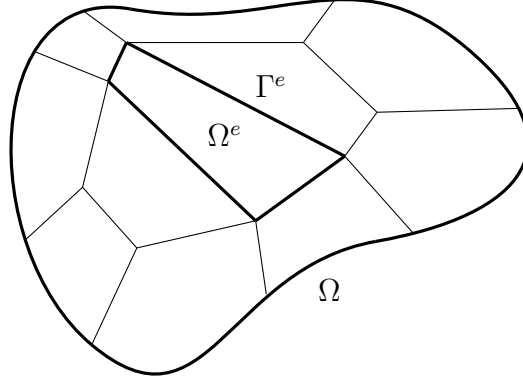
Step 3: Projecting the continuous variational problem into a finite dimensional space through **finite element shape functions** used to approximate the solution, to yield a linear system of the form

$$\mathbf{Kd} = \mathbf{F}. \quad (2.7)$$

Step 4: Solving the system (2.7) for the unknown **degrees of freedom (dofs)** \mathbf{d} .

The matrix \mathbf{K} and vector \mathbf{F} in (2.7) are commonly referred to as the **stiffness matrix** and **load vector** respectively.

To define the weak or variational counterpart of (S) (2.1) (Step 2 above), two classes of functions must be characterized: the space of **trial** (or **candidate**) **functions** and the space of **test** (or **weighting**) **functions**, denoted commonly by \mathcal{S} and \mathcal{V} respectively. In the classical Galerkin FEM (Section 7.1.1), given a partial

Figure 2.1: Decomposition of domain Ω into elements Ω^e

differential equation (PDE) or order $2m$, the spaces \mathcal{S} and \mathcal{V} are defined by:

$$\mathcal{S} = \{u : u \in H^m(\Omega), u \text{ satisfies all essential (Dirichlet) BCs of the problem}\}, \quad (2.8)$$

and

$$\mathcal{V} = \{u : u \in H^m(\Omega), u \text{ satisfies all homogeneous essential (Dirichlet) BCs of the problem}\}, \quad (2.9)$$

where $H^m(\Omega)$ is the Sobolev space defined in (2.2). In the classical Galerkin FEM, the basic requirements on the shape functions chosen to represent the solution to ensure convergence are:

1. [**Smoothness**] The shape functions must be *smooth* (at least C^1) on each element interior, Ω^e .
2. [**Continuity**] The shape functions must be *continuous* across each element boundary Γ^e .
3. [**Completeness**] The space of shape functions must be *complete* (that is, capable of exactly representing an arbitrary linear polynomial when the nodal

degrees of freedom are assigned values in accordance with it).

A finite element method is known as a *Galerkin finite element method* when $\mathcal{S} = \mathcal{V}$ (modulo boundary conditions), that is, when the space of trial functions and the space of test functions are the same. Otherwise, that is when $\mathcal{S} \neq \mathcal{V}$, the resulting method is known as a *Petrov-Galerkin finite element method*.

As will become apparent in Section 2.2, the discontinuous enrichment method (DEM) can be characterized as a *hybrid finite element method*, that is, a two field *mixed finite element method* with the secondary unknown field defined at the element interfaces [12]. The variational formulation of DEM will require the introduction of some additional functional spaces, denoted by $H^{-1/2}(\Gamma)$ and $H^{1/2}(\Gamma)$. The latter space is defined as

$$\begin{aligned} H^{1/2}(\Gamma) &= \{g \in L^2(\Gamma) : v|_{\Gamma} = g, v \in H^1(\Omega)\}, \\ \|g\|_{1/2} &= \inf_{v \in \mathcal{V}_g} |v|_1, \quad \mathcal{V}_g = \{v \in H^1(\Omega) : v|_{\Gamma} = g\}, \end{aligned} \quad (2.10)$$

where $|\cdot|_1$ denotes the following *semi-norm* in $H^1(\Omega)$:

$$|v|_1^2 \equiv \int_{\Omega} |\nabla v|^2 d\Omega. \quad (2.11)$$

The space $H^{-1/2}(\Gamma)$ is the dual space of $H^{1/2}(\Gamma)$, with its norm given by

$$\|g'\|_{-1/2} = \sup_{g \in H^{1/2}(\Gamma)} \frac{\langle g', g \rangle}{\|g\|_{1/2}} = \sup_{v \in H^1(\Omega)} \frac{\langle g', v \rangle}{|v|_1}. \quad (2.12)$$

Here, $\langle \cdot, \cdot \rangle$ denotes the $L^2(\Gamma)$ inner product over the space of measurable, square integrable functions on the domain Γ :

$$\langle c, v \rangle = \int_{\Gamma} cv d\Gamma. \quad (2.13)$$

2.2 Hybrid variational formulation of DEM

To facilitate the presentation in this section, the following notation is introduced. The union of element interiors and element boundaries will be denoted $\tilde{\Omega}$ and $\tilde{\Gamma}$, respectively,

$$\tilde{\Omega} = \cup_{e=1}^{n_{el}} \Omega^e, \quad \tilde{\Gamma} = \cup_{e=1}^{n_{el}} \Gamma^e. \quad (2.14)$$

The set of element interfaces (or interior element boundaries) will be denoted by

$$\Gamma_{\text{int}} = \tilde{\Gamma} \setminus \Gamma, \quad (2.15)$$

and the intersection between two adjacent boundaries Γ^e and $\Gamma^{e'}$ will be denoted by

$$\Gamma^{e,e'} = \Gamma^e \cap \Gamma^{e'}. \quad (2.16)$$

The formulation of DEM is obtained by rewriting the strong form (S) of the BVP (2.1) in its *weak variational form*. To this effect, two functional spaces are introduced

$$\mathcal{V} \equiv \left\{ v \in L^2(\tilde{\Omega}) : v|_{\Omega^e} \in H^1(\Omega^e) \right\}, \quad (2.17)$$

$$\mathcal{W} = \Pi_e \Pi_{e' < e} H^{-1/2}(\Gamma^{e,e'}) \times H^{-1/2}(\Gamma). \quad (2.18)$$

\mathcal{V} is a space of element approximations of the solution and \mathcal{W} is a space of *Lagrange multipliers*. DEM is a Galerkin method, so that $\mathcal{S} = \mathcal{V}$; that is, the space of test and trial functions do not differ. Hence, from this point forward, both spaces will be denoted by \mathcal{V} (2.17).

A key feature of DEM is that the space of element approximations — that is, the discrete analog of \mathcal{V} (2.17) — is allowed to be discontinuous across element interfaces. That is, the second property of the three shape function criteria enumerated in Section 2.1 (Smoothness, Continuity and Completeness) can be violated. Since it is typically desired that the numerical solution remain continuous across the element interfaces in some sense, the following inter-element continuity constraint is added to the BVP

(2.1):

$$\llbracket c(\mathbf{x}) \rrbracket \equiv \left| \lim_{[\mathbf{x} \in \Omega^e] \rightarrow \Gamma^{e,e'}} c(\mathbf{x}) - \lim_{[\mathbf{x} \in \Omega^{e'}] \rightarrow \Gamma^{e,e'}} c(\mathbf{x}) \right| = 0, \quad \mathbf{x} \in \Gamma_{\text{int}}. \quad (2.19)$$

The constraint (2.19) may be enforced weakly using Lagrange multipliers or by the penalty method. In DEM, the former weak enforcement is adopted – that is, (2.19) is enforced weakly using Lagrange multipliers belonging to the space \mathcal{W} (2.18).

The weak form of the BVP (2.1) is obtained first by multiplying the first equation in (2.1) by a test function $v \in \mathcal{V}$ and integrating the diffusion term by parts:

$$\int_{\Omega} (-\kappa \Delta c + \mathbf{a} \cdot \nabla c) v d\Omega = -\kappa \int_{\Gamma} \underbrace{(\nabla c \cdot \mathbf{n})}_{\equiv \mathcal{L}_b c} v d\Gamma + \int_{\Omega} (\kappa \nabla c \cdot \nabla v + \mathbf{a} \cdot \nabla c v) d\Omega. \quad (2.20)$$

Here, \mathcal{L}_b is the boundary operator corresponding to \mathcal{L} . Constraining the solution to remain continuous across the element interfaces, that is, the addition of the constraint (2.19), leads to the following weak hybrid variational formulation

$$(W) : \begin{cases} \text{Find } (c, \lambda) \in \mathcal{V} \times \mathcal{W} \text{ such that} \\ a(v, c) + b(\lambda, v) = r(v) \quad \forall v \in \mathcal{V}, \\ b(\mu, c) = -r_d(\mu) \quad \forall \mu \in \mathcal{W}, \end{cases} \quad (2.21)$$

where $a(\cdot, \cdot)$ and $b(\cdot, \cdot)$ are **bilinear forms** on $\mathcal{V} \times \mathcal{V}$ and $\mathcal{W} \times \mathcal{V}$ respectively. They are given by

$$a(v, c) \equiv (\kappa \nabla v + v \mathbf{a}, \nabla c)_{\tilde{\Omega}} = \int_{\tilde{\Omega}} (\kappa \nabla v \cdot \nabla c + v \mathbf{a} \cdot \nabla c) d\Omega, \quad (2.22)$$

$$b(\lambda, v) \equiv \sum_e \sum_{e' < e} \int_{\Gamma^{e,e'}} \lambda (v_{e'} - v_e) d\Gamma + \int_{\Gamma} \lambda v d\Gamma, \quad (2.23)$$

In (2.21), $r(v)$ and $r_d(\mu)$ (d for “Dirichlet”) are the following **linear forms**

$$r(v) \equiv (f, v) = \int_{\Omega} f v d\Omega, \quad (2.24)$$

$$r_d(\mu) \equiv \langle \mu, g \rangle = \int_{\Gamma} \mu g d\Gamma. \quad (2.25)$$

In (2.22) and (2.24), (\cdot, \cdot) denotes the usual L^2 inner product over Ω (2.5) and $\langle \cdot, \cdot \rangle$ denotes the usual L^2 inner product over Γ (2.13); in (2.23), $v_e \equiv v|_{\Omega^e}$. Note that the bilinear form $a(\cdot, \cdot)$ in (2.22) is *not* symmetric ($a(v, c) \neq a(c, v)$) for the advection-diffusion operator due to the presence of the first order advection term.

Remark 2.2.1. *The variational form (2.21) is not unique. Assuming \mathbf{a} is divergence-free (or incompressible), that is $\nabla \cdot \mathbf{a} = 0$, the following identity holds:*

$$\mathbf{a} \cdot \nabla c = \nabla \cdot (\mathbf{a}c), \quad (2.26)$$

so that

$$\mathbf{a} \cdot \nabla c = \alpha \mathbf{a} \cdot \nabla c + (1 - \alpha) \nabla \cdot (\mathbf{a}c), \quad (2.27)$$

for $\alpha \in [0, 1]$. Substituting (2.27) into the first equation in (2.1), multiplying this equation by a test function $v \in \mathcal{V}$, and performing an integration by parts not only on the diffusion term but also the advection term $(1 - \alpha) \nabla \cdot (\mathbf{a}c)$ gives:

$$\begin{aligned} \int_{\Omega} (-\kappa \Delta c + \mathbf{a} \cdot \nabla c) v d\Omega &= \int_{\Gamma} [(1 - \alpha) \mathbf{a} \cdot \mathbf{n}c - \kappa \nabla c \cdot \mathbf{n}] v d\Gamma \\ &+ \underbrace{\int_{\Omega} [\alpha (\mathbf{a} \cdot \nabla c) v - (1 - \alpha) (\mathbf{a} \cdot \nabla v) c + \kappa \nabla c \cdot \nabla v] d\Omega}_{a_{\alpha}(v, c)}. \end{aligned} \quad (2.28)$$

Comparing (2.28) with (2.20), the reader may observe that the procedure just outlined has resulted in a modified bilinear form $a_{\alpha}(\cdot, \cdot)$, defined in (2.28). The form (2.22) can be recovered from (2.28) by setting $\alpha = 1$, and is commonly referred to as the **convective form**. When $\alpha = \frac{1}{2}$, the form (2.28) is referred to as the **skew-symmetric form** [59], due to the property that

$$\tilde{a}(v, c) \equiv \frac{1}{2} \int_{\Omega} [(\mathbf{a} \cdot \nabla c) v - (\mathbf{a} \cdot \nabla v) c] d\Omega \quad (2.29)$$

is skew-symmetric, that is $\tilde{a}(c, v) = -\tilde{a}(v, c)$.

Remark 2.2.2. *The weak form (W) (2.21) is equivalent to a constrained minimization problem, namely*

$$\begin{aligned} & \text{minimize} && J(v), \\ & \text{s.t.} \begin{cases} v \in \mathcal{V}, \\ [[v]] = 0, & \text{on } \Gamma_{\text{int}}, \\ v = g & \text{on } \Gamma \end{cases} \end{aligned} \quad (2.30)$$

where

$$J(v) \equiv \frac{1}{2}a_{1/2}(v, v) - r(v) = \frac{\kappa}{2}(\nabla v, \nabla v) - r(v). \quad (2.31)$$

(2.30) can be transformed into an unconstrained minimization problem [53, 1] through the definition of the **Lagrangian**:

$$\mathcal{L}(v, \mu) \equiv J(v) + b(\mu, v) + r_d(\mu), \quad (2.32)$$

so that (2.30) is equivalent to

$$\min_{v \in \mathcal{V}} \max_{\mu \in \mathcal{W}} \mathcal{L}(v, \mu). \quad (2.33)$$

The saddle point equations for (2.33) give rise to the weak formulation (2.21) as well as the Euler-Lagrange equations (2.34).

Denoting the jump at an element boundary by $[[\cdot]]$, the **Euler-Lagrange equations** corresponding to (W) are

$$\begin{aligned} \mathcal{L}c &\equiv -\kappa\Delta c + \mathbf{a} \cdot \nabla c = f && \text{in } \tilde{\Omega}, \\ [[c]] &= 0 && \text{on } \Gamma_{\text{int}}, \\ c &= g && \text{on } \Gamma, \\ \lambda &= \mathcal{L}_b c = \nabla c \cdot \mathbf{n} && \text{on } \tilde{\Gamma}. \end{aligned} \quad (2.34)$$

The last equation in (2.34) provides an interpretation of the Lagrange multiplier field: since for this problem the boundary operator \mathcal{L}_b corresponding to \mathcal{L} is the normal derivative of the solution (see (2.20)), the Lagrange multiplier field is the normal derivative of the solution to the BVP (2.1) on the element interfaces.

2.3 Approximation spaces in DEM

The finite-dimensional analog of the hybrid DEM formulation (2.21) is obtained by selecting finite dimensional solution spaces for the primal unknown and dual Lagrange multiplier fields, denoted respectively by

$$\mathcal{V}^h \subset \mathcal{V}, \quad \mathcal{W}^h \subset \mathcal{W}, \quad (2.35)$$

where h denotes the generic size of a typical element Ω^e . Once the approximation spaces \mathcal{V}^h and \mathcal{W}^h are constructed, an approximate solution $(c^h, \lambda^h) \in (\mathcal{V}^h, \mathcal{W}^h)$ of the Galerkin problem corresponding to (2.21) is sought.

2.3.1 The primal approximation space \mathcal{V}^h

In the classical Galerkin finite element method, the trial functions are continuous piecewise polynomials within each element Ω^e — that is, $c^h = c^P$ with

$$c^P \in \mathcal{V}^P \subset P_n(x, y) \subset H^1(\Omega), \quad (2.36)$$

where

$$P_n(x, y) \equiv \left\{ p \in H^1(\Omega^e) : p(x, y) = \sum_{i=0}^n a_i x^i y^i, (x, y) \in \Omega^e, a_i \in \mathbb{R}, n \in \mathbb{N} \right\}, \quad (2.37)$$

is a polynomial interpolation space satisfying the three properties enumerated in Section 2.1 (Smoothness, Continuity and Completeness). A popular class of shape functions that satisfies these properties is the set of *isoparametric shape functions* (Chapter 3 of [6]). These shape functions are reviewed briefly in Section 7.1.1 of the Appendix.

In DEM [1, 56, 57, 58, 46, 48, 50], the primal unknown c^h which defines the approximation space \mathcal{V}^h has one of the following two forms

$$c^h = \begin{cases} c^P + c^E, & \text{if } f \neq 0 \text{ in (2.1) } \textit{(true DEM element)}, \\ c^E, & \text{if } f \equiv 0 \text{ in (2.1) } \textit{(pure DGM element)}. \end{cases} \quad (2.38)$$

$c^P \in \mathcal{V}^P \subset H^1(\Omega)$ are standard, continuous, piecewise polynomial finite element shape functions (2.36), and $c^E \in \mathcal{V}^E$ are the so-called **enrichment functions**.

The weak enforcement of continuity through the constraint (2.19) leaves much flexibility as to the design of the space \mathcal{V}^E . At the heart of DEM is the idea that \mathcal{V}^E should be designed in a way that incorporates some information about the particular BVP being solved. To this effect, \mathcal{V}^E is defined in DEM as the set of free-space solutions of the homogeneous PDE to be solved which are not represented in \mathcal{V}^P (so as to avoid linear dependencies with functions already represented in \mathcal{V}^P). Mathematically,

$$\mathcal{V}^E \subset \{\mathcal{L}c^E = 0 \text{ in } \mathbb{R}^d\}, \quad (2.39)$$

for a generic linear PDE $\mathcal{L}c = f$ in $d = 1, 2, 3$ spatial dimensions.

As (2.38) suggests, two varieties of DEM can be defined: a true or “full” DEM, and an enrichment-only DEM referred to in the remainder of this dissertation as “DGM” (for **discontinuous Galerkin method**). In variational multiscale (VMS) [27] terminology, the splitting of the approximation into polynomials and enrichment functions, as done in the first line of (2.38), can be viewed as a decomposition of the numerical solution into coarse (polynomial) and fine (enrichment) scales. Elements for which the solution space \mathcal{V}^h is constructed as a direct sum of \mathcal{V}^P and \mathcal{V}^E are termed “full” or **true DEM** elements. The general rule of thumb is to employ these elements when solving inhomogeneous problems, as the enrichment field defined by (2.39) is not guaranteed to span the particular solutions to these PDEs. If the PDE to be solved is homogeneous to begin with, however, the enrichment field (2.39) may entirely capture the solution to the problem, rather than merely enhance the polynomial field. This motivates the construction of so-called **pure DGM** elements (second line of (2.38)), for which the contribution of the standard polynomial field \mathcal{V}^P is dropped from \mathcal{V}^h , resulting in improved computational efficiency without a loss of accuracy (Section 2.4.3).

The careful reader may observe that in defining the enrichment space \mathcal{V}^E as in (2.39), it has been assumed that the homogeneous free-space solutions to $\mathcal{L}c = 0$ are available in closed analytical form for the given operator \mathcal{L} . In general, it is

possible to obtain these solutions analytically primarily for linear PDEs with constant coefficients. As discussed in detail in Chapter 5, since the enrichment functions in DEM are to be employed at the *element* level, it is natural to use the solutions of the constant-coefficient version of the PDE of interest — that is, use a fixed value of the advection field $\mathbf{a}(\mathbf{x}) \equiv \mathbf{a}$ in (1.2) inside each element — to define the enrichment field \mathcal{V}^E in the more general variable-coefficient context.

2.3.2 Babuška-Brezzi *inf-sup* condition

As DEM is a hybrid method, care must be taken to design the space \mathcal{W}^h such that the well known ***Babuška-Brezzi inf-sup*** condition [12, 55, 60], a necessary condition for ensuring a non-singular global interface problem from the discrete form of (2.21), is upheld. This condition is reviewed briefly in this section.

Recall the bilinear forms $a : \mathcal{V} \times \mathcal{V}$ and $b : \mathcal{V} \times \mathcal{W}$ defined in (2.22) and (2.23) respectively. Let $A : \mathcal{V} \rightarrow \mathcal{V}$ and $B : \mathcal{W} \rightarrow \mathcal{V}$ denote linear bounded operators associated with these forms, that is

$$\begin{aligned} a(v, c) &= (v, Ac)_{\mathcal{V} \times \mathcal{V}}, \\ b(\lambda, v) &= (\lambda, Bv)_{\mathcal{W} \times \mathcal{W}} = (B^T \lambda, v)_{\mathcal{V} \times \mathcal{V}}, \end{aligned} \tag{2.40}$$

where $(\cdot, \cdot)_{\mathcal{V} \times \mathcal{V}}$ and $(\cdot, \cdot)_{\mathcal{W} \times \mathcal{W}}$ denote the inner products on $\mathcal{V} \times \mathcal{V}$ and $\mathcal{W} \times \mathcal{W}$ respectively. It is well known [54] that

$$\begin{cases} Ac + B^T \lambda &= f \\ Bc &= 0, \end{cases} \tag{2.41}$$

has a unique solution, that is, is a well-posed problem, if

- (i) The bilinear form $a(\cdot, \cdot)$ is coercive on $\ker B = \{v \in \mathcal{V} : b(\mu, v) = 0, \forall \mu \in \mathcal{W}\}$.
- (ii) The map B is surjective.

If B has a closed range, typically (ii) can be replaced with the condition that B^T is injective. The condition (ii) is commonly referred to as the Babuška-Brezzi, or *inf-sup* condition.

To extend this condition to the discrete problem, let $A_h : \mathcal{V}^h \rightarrow \mathcal{V}^h$ and $B_h : \mathcal{W}^h \rightarrow \mathcal{V}^h$ denote the discrete versions of the operators defined in (2.40). Then, the following theorem describes the existence and uniqueness of solutions of the discrete version of the variational problem (2.21) (Prop. II.2.1 in [12]).

Theorem 2.3.1. *If there exists $v^h \in \mathcal{V}^h$ such that $b(\mu^h, v^h) = -r_d(\mu^h)$ for any $\mu^h \in \mathcal{W}^h$ and there exist positive constants α and γ independent of h such that*

$$\inf_{c^h \in \text{Ker}B_h} \sup_{v^h \in \text{Ker}B_h} \frac{a(v^h, c^h)}{\|c^h\|_{\mathcal{V}} \|v^h\|_{\mathcal{V}}} \geq \alpha, \quad (2.42)$$

and

$$\inf_{\mu^h \in \mathcal{W}^h} \sup_{v^h \in \mathcal{V}^h} \frac{b(\mu^h, v^h)}{\|v^h\|_{\mathcal{V}} \|\mu^h\|_{\mathcal{W} \setminus \text{Ker}B^T}} \geq \gamma, \quad (2.43)$$

then the discrete analog of (2.21) has a unique solution $(c^h, \lambda^h) \in \mathcal{V}^h \times \mathcal{W}^h \setminus \text{Ker}B_h^T$, where

$$\begin{aligned} \text{Ker}B_h &\equiv \{v^h \in \mathcal{V}^h : b(\mu^h, v^h) = 0, \forall \mu^h \in \mathcal{W}^h\}, \\ \text{Ker}B_h^T &\equiv \{\mu^h \in \mathcal{W}^h : b(\mu^h, v^h) = 0, \forall v^h \in \mathcal{V}^h\}. \end{aligned} \quad (2.44)$$

Moreover,

$$\|c - c^h\|_{\mathcal{V}} + \|\lambda - \lambda^h\|_{\mathcal{W}^h \setminus \text{Ker}B_h^T} \leq C \left(\inf_{v^h \in \mathcal{V}^h} \|c - v^h\|_{\mathcal{V}} + \inf_{\mu^h \in \mathcal{W}^h} \|\lambda - \mu^h\|_{\mathcal{W}} \right), \quad (2.45)$$

for some constant $C \in \mathbb{R}$.

Condition (2.43) is the discrete version of the as the Babuška-Brezzi or *inf-sup* condition. Care must be taken to design the spaces \mathcal{V}^h and \mathcal{W}^h such that this condition is upheld, as the failure of the condition can put into jeopardy the solvability of the system arising from the discrete form of (2.21). An extensive survey for discretizing a Lagrange multiplier field of a form similar to that considered herein can be found in Section 3.3 of [12]. Most, if not all, of these established techniques and theoretical results are for standard polynomial approximations of the solution c^h . Extending these ideas, namely designing the approximation spaces such that it can be proven *a priori* that the bilinear form $b(\cdot, \cdot)$ satisfies the condition (2.43), to the typically non-polynomial approximations c^E employed in DEM is not a straightforward

task. Some progress has been made by Amara *et al.* in the context of low-order DEM elements for the Helmholtz equation and plane wave enrichment functions [52], but the task of showing that (2.42) holds for the advection-diffusion DEM elements developed in this dissertation remains an open problem at the present time.

The elements proposed in this dissertation are developed to satisfy an *inf-sup* condition for the discrete, finite dimensional problem of (2.21). This algebraic *inf-sup* condition is a necessary condition for (2.43) to hold. By inspection, assuming without loss of generality that $g = 0$, it is straightforward to see that this (global) system will have the form:

$$\left(\begin{array}{c|c} \mathbf{A} & \mathbf{B}^T \\ \hline \mathbf{B} & \mathbf{0} \end{array} \right) \begin{pmatrix} \mathbf{c}^h \\ \boldsymbol{\lambda}^h \end{pmatrix} = \begin{pmatrix} \mathbf{f} \\ \mathbf{0} \end{pmatrix}, \quad (2.46)$$

where $\mathbf{c}^h \in \mathbb{R}^n$ and $\boldsymbol{\lambda}^h \in \mathbb{R}^p$ are vectors containing the primal unknown and Lagrange multiplier unknown dofs respectively, so that the matrices \mathbf{A} and \mathbf{B} are $n \times n$ and $p \times n$ respectively, and $\mathbf{f} \in \mathbb{R}^n$, for $n, p \in \mathbb{N}$ are the number of enrichment equations and the number of Lagrange multiplier equations, respectively. It is possible to derive conditions on \mathcal{V}^h and \mathcal{W}^h for this discrete condition to hold by examining the matrix form of the problem arising from the discretization of (2.21). The system (2.46) has no solution if it is over-determined (and inconsistent). The matrix \mathbf{A} represents the global stiffness matrix and must be non-singular by construction. It is straightforward to see, from basic linear algebra, that, assuming \mathbf{A} is non-singular, (2.46) is over-determined if $p > n$. The outcome of this condition puts the following bound on the dimension of the Lagrange multiplier approximation space \mathcal{W}^h given an enrichment space \mathcal{V}^E of n^E linearly independent basis functions:

$$\left\{ \begin{array}{l} \# \text{ of enrichment} \\ \text{equations} \end{array} \right\} \geq \left\{ \begin{array}{l} \# \text{ Lagrange multiplier} \\ \text{constraint equations} \end{array} \right\}. \quad (2.47)$$

Assuming a mesh of $n^{el} = n^2$ quadrilateral elements, with n^E enrichment functions in each element, and n^λ Lagrange multiplier approximations per edge, the left hand side of (2.47) is $n^E n^2$ and the right hand side is $2n(n+1)n^\lambda$, so that (2.47) implies

that

$$n^E n^2 \geq 2n(n+1)n^\lambda \approx 2n^2 n^\lambda. \quad (2.48)$$

It follows from (2.48) that the asymptotic bound on the number of Lagrange multipliers per edge (n^λ) is given by

$$n^\lambda \leq \frac{n^E}{2}, \quad (2.49)$$

almost everywhere in the mesh.

In Section 2.3.3, a space of Lagrange multiplier approximations for the 2D advection-diffusion equation that is related to the normal derivatives of the enrichment functions c^E on the element edges in a well-defined way is constructed, taking care to limit its cardinality to avoid violating the bound (2.49).

Remark 2.3.2. *The condition (2.49) is a necessary, but in general not a sufficient, condition for ensuring that a non-singular global interface problem arises in the application of the DEM on a mesh of quadrilateral elements. In practice, fewer than $n^\lambda = \frac{n^E}{2}$ Lagrange multipliers per edge will be used. Numerical tests (Sections 4.5 and 5.6) show that the general rule of thumb is to limit*

$$n^\lambda = \left\lfloor \frac{n^E}{4} \right\rfloor, \quad (2.50)$$

where $\lfloor x \rfloor \equiv \max\{n \in \mathbb{Z} | n \leq x\}$ for any $x \in \mathbb{R}$.

Remark 2.3.3. *Another algebraic version of the inf-sup condition (2.43) is $\ker \mathbf{B}^T = \mathbf{0}$. If this holds, (2.46) will be an under-determined system with an infinite number of solutions. This can result in the presence of **spurious modes** in the computation (Chapter 4 of [54]).*

2.3.3 The dual space of Lagrange multiplier approximations

\mathcal{W}^h

An expression for the Lagrange multiplier approximations constituting the space \mathcal{W}^h given an approximation space \mathcal{V}^h can be derived from the weak form (2.21) using some

variational calculus. Applying the bilinear form $a(\cdot, \cdot)$ defined in (2.22) to $c, v \in \mathcal{V}$ and integrating by parts the $\int_{\tilde{\Omega}} \nabla v \cdot \nabla c d\Omega$ term gives

$$a(c, v) = \int_{\tilde{\Omega}} (-\kappa \Delta c + \mathbf{a} \cdot \nabla c) v d\Omega + \int_{\Gamma} \kappa \nabla c \cdot \mathbf{n} v d\Gamma + \sum_e \sum_{e'} \int_{\Gamma^{e,e'}} \kappa (\nabla c^e \cdot \mathbf{n}^e v^e + \nabla c^{e'} \cdot \mathbf{n}^{e'} v^{e'}) d\Gamma, \quad (2.51)$$

where \mathbf{n}^e is the outward unit normal to Γ^e (and similarly for $\mathbf{n}^{e'}$ and $\Gamma^{e'}$). Substituting (2.51) into the first equation in the weak form (2.21) leads to

$$\lambda = \nabla c_e \cdot \mathbf{n}^e = -\nabla c_{e'} \cdot \mathbf{n}^{e'} \quad \text{on } \Gamma^{e,e'}, \quad (2.52)$$

and

$$\lambda = -\nabla c \cdot \mathbf{n} \quad \text{on } \Gamma, \quad (2.53)$$

if a Dirichlet boundary condition is to be enforced on Γ . (2.52) suggests choosing

$$\lambda^h \approx \nabla c_e^E \cdot \mathbf{n}^e = -\nabla c_{e'}^E \cdot \mathbf{n}^{e'} \quad \text{on } \Gamma^{e,e'}, \quad (2.54)$$

as a good approximation of the Lagrange multiplier on an edge $\Gamma^{e,e'}$; that is, defining the space \mathcal{W}^h to consist of the approximate normal derivatives of c^E on the element edges – but being careful not to violate the bound (2.49) arising from the discrete form of the Babuška-Brezzi *inf-sup* condition (2.43). In practice, the number of Lagrange multiplier approximations allowed per edge given n^E enrichment functions will be set according to the rule of thumb (2.50) (Remark 2.3.2).

2.4 Galerkin formulation and implementation of DEM

Assuming the more general case of the full DEM and substituting the approximation c^h (the first row of (2.38)) into the weak form (2.21) results in the following discrete

Galerkin problem

$$(G) : \begin{cases} \text{Find } (c^h, \lambda^h) \in \mathcal{V}^h \times \mathcal{W}^h \text{ such that} \\ a(v^P, c^P) + a(v^P, c^E) + b(\lambda^h, v^P) = r(v^P), \\ a(v^E, c^P) + a(v^E, c^E) + b(\lambda^h, v^E) = r(v^E), \\ b(\mu^h, c^P) + b(\mu^h, c^E) = -r_d(\mu^h), \\ \text{holds } \forall (v^h, \mu^h) \in \mathcal{V}^h \times \mathcal{W}^h. \end{cases} \quad (2.55)$$

The above system of Galerkin equations (G) gives rise to the element matrix equation

$$\underbrace{\begin{pmatrix} \mathbf{k}^{PP} & \mathbf{k}^{PE} & \mathbf{k}^{PC} \\ \mathbf{k}^{EP} & \mathbf{k}^{EE} & \mathbf{k}^{EC} \\ \mathbf{k}^{CP} & \mathbf{k}^{CE} & \mathbf{0} \end{pmatrix}}_{\equiv \mathbf{k}^e} \begin{pmatrix} \mathbf{c}^P \\ \mathbf{c}^E \\ \boldsymbol{\lambda}^h \end{pmatrix} = \underbrace{\begin{pmatrix} \mathbf{r}^P \\ \mathbf{r}^E \\ \mathbf{r}^C \end{pmatrix}}_{\equiv \mathbf{r}^e}, \quad (2.56)$$

where \mathbf{c}^P , \mathbf{c}^E and $\boldsymbol{\lambda}^h$ are vectors containing the local dofs c^P , c^E and λ^h , respectively. The superscript e designates the element domain and the superscript C designates the continuity constraints enforced by the Lagrange multipliers. The correspondence between the matrices and the Galerkin equations is obtained by comparing (2.55) and (2.56), and is summarized in Table 2.1.

Note that $\mathbf{k}^{EP} \neq \mathbf{k}^{PE^T}$ as a result of the asymmetry of the bilinear form $a(\cdot, \cdot)$ for the advection-diffusion operator. In the case of a pure DGM implementation, \mathbf{k}^{PP} , \mathbf{k}^{PE} , \mathbf{k}^{PC} , \mathbf{k}^{EP} , \mathbf{k}^{CP} , $\mathbf{r}^P = \{\emptyset\}$ (that is, they are empty and can be omitted) and therefore the three-by-three block system (2.56) reduces to a two-by-two block system, namely

$$\begin{pmatrix} \mathbf{k}^{EE} & \mathbf{k}^{EC} \\ \mathbf{k}^{CE} & \mathbf{0} \end{pmatrix} \begin{pmatrix} \mathbf{c}^E \\ \boldsymbol{\lambda}^h \end{pmatrix} = \begin{pmatrix} \mathbf{r}^E \\ \mathbf{r}^C \end{pmatrix}. \quad (2.57)$$

2.4.1 Integration of $a(\cdot, c^E)$

If the enrichment field \mathcal{V}^E is comprised of free-space solutions to (2.1), the volume integrals appearing in the bilinear forms $a(\cdot, c^E)$ (2.22) can be converted to integrals

Table 2.1: Correspondence between the local matrices in (2.56) and the bilinear/linear forms in (2.55)

Matrix	Galerkin Term
\mathbf{k}^{PP}	$a(v^{\text{P}}, c^{\text{P}})$
\mathbf{k}^{PE}	$a(v^{\text{P}}, c^{\text{E}})$
\mathbf{k}^{PC}	$\langle v^{\text{P}}, \lambda^{\text{h}} \rangle_{\Gamma_{\text{int}}}$
\mathbf{k}^{EP}	$a(v^{\text{E}}, c^{\text{P}})$
\mathbf{k}^{EE}	$a(v^{\text{E}}, c^{\text{E}})$
\mathbf{k}^{EC}	$\langle c^{\text{E}}, \lambda^{\text{h}} \rangle_{\Gamma_{\text{int}}}$
\mathbf{k}^{CP}	$\langle \mu^{\text{h}}, c^{\text{P}} \rangle_{\Gamma_{\text{int}}}$
\mathbf{k}^{CE}	$\langle \mu^{\text{h}}, c^{\text{E}} \rangle_{\Gamma_{\text{int}}}$
\mathbf{r}^{P}	$r(c^{\text{P}})$
\mathbf{r}^{E}	$r(c^{\text{E}})$
\mathbf{r}^{C}	$-r_d(\lambda^{\text{h}})$

over the edges of each element. That is, if $\mathcal{L}c^{\text{E}} = 0$, then, for $v^{\text{h}} \in \mathcal{V}^{\text{h}}$:

$$0 = \int_{\Omega^e} [\mathbf{a} \cdot \nabla c^{\text{E}} - \kappa \Delta c^{\text{E}}] v^{\text{h}} d\Omega = \underbrace{\int_{\Omega^e} [\mathbf{a} \cdot \nabla c^{\text{E}} v^{\text{h}} + \kappa \nabla c^{\text{E}} \nabla v^{\text{h}}] d\Omega}_{a(v^{\text{h}}, c^{\text{E}})_{\Omega^e}} - \kappa \int_{\Gamma^e} \nabla c^{\text{E}} \cdot \mathbf{n} v^{\text{h}} d\Gamma. \quad (2.58)$$

Rearranging (2.58) gives

$$a(v^{\text{h}}, c^{\text{E}})_{\Omega^e} = \kappa \int_{\Gamma^e} \nabla c^{\text{E}} \cdot \mathbf{n} v^{\text{h}} d\Gamma. \quad (2.59)$$

Thus, integration in element domains can be replaced by integration along element boundaries. It follows that, from Table 2.1, in the case of a homogeneous constant-coefficient BVP and a pure DGM element, no volume integrals need to be computed at all.

2.4.2 Static condensation at the element level

Due to the discontinuous nature of \mathcal{V}^{E} , \mathbf{c}^{E} can be eliminated at the element level by a *static condensation*. For a full DEM element, taking the Schur complement of the second equation in (2.56) and substituting this expression into the first and third

equations leads to the following (local) statically-condensed system

$$\underbrace{\begin{pmatrix} \tilde{\mathbf{k}}^{\text{PP}} & \tilde{\mathbf{k}}^{\text{PC}} \\ \tilde{\mathbf{k}}^{\text{CP}} & \tilde{\mathbf{k}}^{\text{CC}} \end{pmatrix}}_{\equiv \tilde{\mathbf{k}}^e} \begin{pmatrix} \mathbf{c}^{\text{P}} \\ \boldsymbol{\lambda}^h \end{pmatrix} = \underbrace{\begin{pmatrix} \tilde{\mathbf{r}}^{\text{P}} \\ \tilde{\mathbf{r}}^{\text{C}} \end{pmatrix}}_{\equiv \tilde{\mathbf{r}}^e}, \quad (2.60)$$

where

$$\tilde{\mathbf{k}}^{\text{PP}} = \mathbf{k}^{\text{PP}} - \mathbf{k}^{\text{PE}}(\mathbf{k}^{\text{EE}})^{-1}\mathbf{k}^{\text{EP}}, \quad (2.61)$$

$$\tilde{\mathbf{k}}^{\text{PC}} = \mathbf{k}^{\text{PC}} - \mathbf{k}^{\text{PE}}(\mathbf{k}^{\text{EE}})^{-1}\mathbf{k}^{\text{EC}}, \quad (2.62)$$

$$\tilde{\mathbf{k}}^{\text{CP}} = \mathbf{k}^{\text{CP}} - \mathbf{k}^{\text{CE}}(\mathbf{k}^{\text{EE}})^{-1}\mathbf{k}^{\text{EP}}, \quad (2.63)$$

$$\tilde{\mathbf{k}}^{\text{CC}} = -\mathbf{k}^{\text{CE}}(\mathbf{k}^{\text{EE}})^{-1}\mathbf{k}^{\text{EC}}, \quad (2.64)$$

and

$$\tilde{\mathbf{r}}^{\text{P}} = \mathbf{r}^{\text{P}} - \mathbf{k}^{\text{PE}}(\mathbf{k}^{\text{EE}})^{-1}\mathbf{r}^{\text{E}}, \quad (2.65)$$

$$\tilde{\mathbf{r}}^{\text{C}} = \mathbf{r}^{\text{C}} - \mathbf{k}^{\text{CE}}(\mathbf{k}^{\text{EE}})^{-1}\mathbf{r}^{\text{E}}. \quad (2.66)$$

In the case of a DGM element, there is no polynomial field and therefore $\tilde{\mathbf{k}}^{\text{PP}}$, $\tilde{\mathbf{k}}^{\text{PC}}$, $\tilde{\mathbf{k}}^{\text{CP}}$, $\tilde{\mathbf{r}}^{\text{P}} = \{\emptyset\}$. Since $\tilde{\mathbf{k}}^{\text{CC}}$ reduces to $\tilde{\mathbf{k}}^{\text{CC}} = -\mathbf{k}^{\text{CE}}(\mathbf{k}^{\text{EE}})^{-1}\mathbf{k}^{\text{EC}}$, the statically-condensed system for a DGM element is therefore simply

$$\underbrace{-\mathbf{k}^{\text{CE}}(\mathbf{k}^{\text{EE}})^{-1}\mathbf{k}^{\text{EC}}}_{=\mathbf{k}^e=\tilde{\mathbf{k}}^{\text{CC}}} \boldsymbol{\lambda}^h = \underbrace{\mathbf{r}^{\text{C}} - \mathbf{k}^{\text{CE}}(\mathbf{k}^{\text{EE}})^{-1}\mathbf{r}^{\text{E}}}_{=\tilde{\mathbf{r}}^e=\tilde{\mathbf{r}}^{\text{C}}}. \quad (2.67)$$

Equations (2.60) and (2.67) give rise either to a $\mathbf{c}^{\text{P}}\text{-}\boldsymbol{\lambda}^h$ formulation for the full DEM approximation, or simply to a $\boldsymbol{\lambda}^h$ -formulation for its DGM variant. The global condensed system is obtained from an assembly of the statically-condensed element arrays $\tilde{\mathbf{k}}^e$ and $\tilde{\mathbf{r}}^e$. From this system, the Lagrange multiplier dofs, and, when applicable, the polynomial dofs, are solved for, after which the enrichment dofs are computed by means of a post-processing step local to each element. The key steps of this implementation are summarized in Algorithm 1.

Algorithm 1 Element-level static condensation algorithm

Compute the entries of the element matrices in (2.56) (Table 2.1).

Compute the local Schur complements in (2.61)-(2.66).

Assemble the global interface problem (2.60).

Solve for the vector $\boldsymbol{\lambda}^h$ (and the vector \mathbf{c}^P , if applicable, i.e., in the case of the full DEM).

for each element Ω^e , $e = 1, \dots, n^{el}$ **do**

 Compute \mathbf{c}^E as a post-processing step within Ω^e as follows

$$\mathbf{k}^{EE} \mathbf{c}^E = \mathbf{r}^E - \mathbf{k}^{EP} \mathbf{c}^P - \mathbf{k}^{EC} \boldsymbol{\lambda}^h, \quad (2.68)$$

 (with $\mathbf{k}^{EP} = \{\emptyset\}$ in the case of a DGM element.)

end for

2.4.3 Computational complexity

An important remark at this point in the discussion is that the cost of solving the global interface problem (2.60) is not directly determined by the dimension of \mathcal{V}^E . Instead, it depends on the total number of Lagrange multiplier dofs — that is, on $\dim \mathcal{W}^h$. This property is a result of the element-level static condensation which is enabled by the discontinuous nature of the approximation of the solution (Section 2.4.2). As discussed in Section 2.3.2, the Babuška-Brezzi *inf-sup* condition must be satisfied to ensure that the global interface problem is non-singular. In particular, by (2.49), the dimension of the space \mathcal{W}^h will necessarily be less than the dimension of the primal unknown space \mathcal{V}^E . Note that this property brings a major computational advantage over PUM [25, 26].

Table 2.2 summarizes the computational complexities of some DGM and DEM elements having n^λ Lagrange multipliers per edge, compared to their standard quadrilateral Galerkin FEM counterparts, denoted by Q_n (described in Section 7.1.1 of the Appendix), for $n = 1, 2, 3, 4$. The table reports also the elements' stencil widths assuming an $n \times n$ uniform mesh of quadrilateral elements. The *stencil width* is essentially the maximum number of non-zero entries in the rows of the global system matrix that comes from assembling the local matrices (2.60). Figure 2.2 illustrates the stencils of a first order Galerkin quadrilateral element, referred to as Q_1 , and a pure DGM element having $n^\lambda = 1$ Lagrange multiplier approximations per element edge.

The reader may observe by examining Table 2.2 that the stencil width of a DGM element with n^λ Lagrange multipliers per edge is smaller than that of a Galerkin element Q_{n^λ} element; however the pure DGM element contains n^{el} more total dofs. As computational complexity depends on the total number of dofs *and* the sparsity pattern of the system matrices (measured by the finite element stencil width), it can be reasonably assumed that the computational complexities of a pure DGM element with n^λ Lagrange multipliers is roughly comparable to the computational complexity of a Galerkin Q_{n^λ} element.

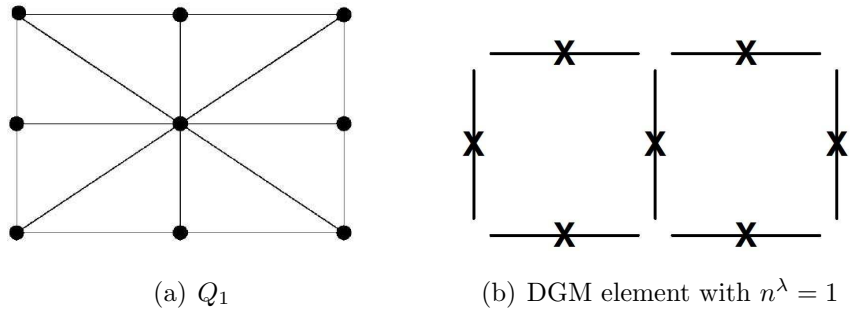


Figure 2.2: Illustration of stencils for first order Galerkin and DGM elements

2.5 Linear least squares “qualifying test” for enrichment functions

The enrichment in DEM, defined as the set of free-space solutions to the governing constant-coefficient homogeneous PDE, is intuitively appealing, as these solutions are related to the operator governing the problem to be solved. Unlike the standard finite element polynomial interpolants, however, it is unclear what can be said about the completeness property of a proposed enrichment space (Property 3 in Section 2.1). The following question arises: how capable are the enrichment functions comprising \mathcal{V}^E of representing the exact (or reference) solution to a particular BVP?

Given an exact (or reference) solution to a BVP, the answer to this question can be studied *a posteriori* by formulating and solving the following **linear least squares**

Table 2.2: Computational complexity of some DGM, DEM and standard Galerkin elements (assuming a discretization into n^{el} quadrilateral elements)

	Element	Asymptotic # of dofs	Stencil width for uniform $n \times n$ mesh
Galerkin	Q_1	n^{el}	9
	Q_2	$3n^{el}$	21
	Q_3	$5n^{el}$	33
	Q_4	$7n^{el}$	45
DGM with	$n^\lambda = 1$	$2n^{el}$	7
	$n^\lambda = 2$	$4n^{el}$	14
	$n^\lambda = 3$	$6n^{el}$	21
	$n^\lambda = 4$	$8n^{el}$	28
DEM with	$n^\lambda = 1$	$3n^{el}$	21
	$n^\lambda = 2$	$5n^{el}$	33
	$n^\lambda = 3$	$7n^{el}$	45
	$n^\lambda = 4$	$9n^{el}$	57

(*L**L**S*) optimization problem in each element Ω^e

$$\min_{a_i^e \in \mathbb{R}} \left\| \underbrace{\sum_{i=1}^{n^E} a_i^e c_i^{E,e}(\mathbf{x}) - c_{\text{ref}}^e(\mathbf{x})}_{\mathbf{r} \equiv \mathbf{A}\mathbf{y} - \mathbf{b}} \right\|_2, \quad \mathbf{x} \in \mathbb{R}^2. \quad (2.69)$$

Here, c_{ref}^e is a reference (or exact) solution to a particular BVP in element Ω^e , the a_i^e are the computed enrichment degrees of freedom, and $c_i^{E,e}(\mathbf{x})$ are the enrichment functions inside that element. If the norm in (2.69) is taken to be the discrete vector two-norm, the (2.69) can be solved using the singular value decomposition (SVD). In particular, if $\mathbf{A} = \mathbf{U}\mathbf{\Sigma}\mathbf{V}^T$ is the SVD of the matrix \mathbf{A} defined in (2.69), then this

argument can be written as:

$$\begin{aligned}
\|\mathbf{A}\mathbf{y} - \mathbf{b}\|_2 &= \|\mathbf{U}\boldsymbol{\Sigma}\mathbf{V}^T\mathbf{y} - \mathbf{b}\|_2 \\
&= \|\mathbf{U}[\boldsymbol{\Sigma}\mathbf{V}^T\mathbf{y} - \mathbf{U}^T\mathbf{b}]\|_2 \\
&= \|\underbrace{\boldsymbol{\Sigma}\mathbf{V}^T\mathbf{y}}_{\equiv \mathbf{z}} - \underbrace{\mathbf{U}^T\mathbf{b}}_{\equiv \mathbf{b}'}\|_2.
\end{aligned} \tag{2.70}$$

From (2.70), it is straightforward to see that the solution to (2.69) is $\mathbf{y} = \mathbf{V}\mathbf{z}$ where, letting z_i and b'_i denote the i^{th} entry of the vectors \mathbf{z} and \mathbf{b}' respectively, and letting σ_i denote the i^{th} singular value of \mathbf{A} ,

$$z_i = \frac{b'_i}{\sigma_i}, \quad i = 1, \dots, r \equiv \text{rank}(\boldsymbol{\Sigma}). \tag{2.71}$$

The minimum value of the residual in (2.69) is

$$\|\mathbf{r}\|_2 = \sum_{i=r+1}^n b'_i, \tag{2.72}$$

where n is the number of points at which \mathbf{x} is sampled in element Ω^e .

The solution to (2.69) gives some insight into how well the enrichment functions employed in element Ω^e are capable of representing the reference solution in that element. Provided a reference solution (or some solution believed to be similar in character to the exact solution to a BVP) is available, it can be worthwhile, especially for variable-coefficient problems, to perform the test (2.69) for a proposed enrichment basis of functions $\{c_i^E(\mathbf{x})\}$ prior to implementing DEM in order to determine if the proposed enrichment functions are capable of representing the reference solution to the problem better than the standard Galerkin polynomial shape functions.

Remark 2.5.1. *The LLS test described here is used to provide justification for omitting certain classes of free-space solutions (derived in Chapter 3) – namely functions with behavior deemed uncharacteristic of the solution to the boundary value problems considered herein – from the design of the space \mathcal{V}^E .*

Chapter 3

Free-space solutions to the 2D advection-diffusion equation

In this chapter, several families of free-space solutions to the advection-diffusion equation (1.2) in two-dimensions (2D) are derived. These functions will be used to define the enrichment spaces \mathcal{V}^E of various DGM and DEM elements in subsequent chapters.

3.1 Free-space solutions to the 2D advection-diffusion equation with constant $\mathbf{a} \in \mathbb{R}^2$

First, some free-space solutions to the constant-coefficient version of (1.2) are derived. These solutions fall into three families:

1. Functions that are exponential in both the x - and y -coordinate directions.
2. Functions that are exponential in one variable and trigonometric in the other.
3. Polynomial functions.

The first two families are derived by the standard PDE solution technique known as *separation of variables* (Section 3.1.1); the third is derived by assuming a finite power series solution and solving a system of equations for the unknown coefficients in this series (Section 3.1.2).

3.1.1 Separation of variables solutions

Suppose $\mathbf{a}^T = (a_1, a_2) \in \mathbb{R}^2$, and assume the following functional form for the solution to $\mathcal{L}c^E = -\kappa\Delta c^E + \mathbf{a} \cdot \nabla c^E = 0$:

$$c^E(x, y) = F(x)G(y). \quad (3.1)$$

Here, $F, G : \mathbb{R} \rightarrow \mathbb{R}$ are some $C^2(\mathbb{R})$ functions that will be determined such that $\mathcal{L}c^E = 0$ is satisfied. Substituting (3.1) into (1.2) implies

$$\frac{\frac{a_1}{\kappa}F'(x) - F''(x)}{F(x)} = \frac{G''(y) - \frac{a_2}{\kappa}G'(y)}{G(y)} \equiv k \in \mathbb{R}. \quad (3.2)$$

(3.2) can be decomposed into the following two ordinary differential equations (ODEs) for the functions unknown $F(x)$ and $G(y)$, to be determined

$$\begin{aligned} F''(x) - \frac{a_1}{\kappa}F'(x) + kF(x) &= 0, \\ G''(y) - \frac{a_2}{\kappa}G'(y) - kG(y) &= 0. \end{aligned} \quad (3.3)$$

The solutions to (3.3) are $\text{span}\{F_k(x)\}$ and $\text{span}\{G_k(y)\}$, where

$$F_k(x) = \begin{cases} \exp\left\{\frac{a_1x}{2\kappa} \pm \frac{\sqrt{a_1^2 - 4k\kappa^2}}{2\kappa}x\right\} & \text{if } k \leq \frac{a_1^2}{4\kappa^2}, \\ \exp\left\{\frac{a_1x}{2\kappa} \pm \frac{i\sqrt{-a_1^2 + 4k\kappa^2}}{2\kappa}x\right\} & \text{if } k > \frac{a_1^2}{4\kappa^2}, \end{cases} \quad (3.4)$$

$$G_k(y) = \begin{cases} \exp\left\{\frac{a_2y}{2\kappa} \pm \frac{\sqrt{a_2^2 + 4k\kappa^2}}{2\kappa}y\right\} & \text{if } k \geq -\frac{a_2^2}{4\kappa^2}, \\ \exp\left\{\frac{a_2y}{2\kappa} \pm \frac{i\sqrt{-a_2^2 - 4k\kappa^2}}{2\kappa}y\right\} & \text{if } k < -\frac{a_2^2}{4\kappa^2}, \end{cases} \quad (3.5)$$

and $i \equiv \sqrt{-1}$. The form of the solution (3.1) thus depends on the value of the separation of variables constant k relative to the given advection velocities a_1 and a_2 . The expressions (3.4) and (3.5) imply that the solution can take on one of three forms, summarized in Table 3.1. In the first case, the enrichment function c^E is a rapidly rising or falling exponential in both the x - and y -coordinate directions. In the

second and third cases, the enrichment is oscillatory in one direction.

Table 3.1: Forms of the free-space solution c^E to $\mathbf{a} \cdot \nabla c^E - \kappa \Delta c^E = 0$

k		$F_k(x)$	$G_k(y)$
\in	$\left[-\frac{a_2^2}{4\kappa^2}, \frac{a_1^2}{4\kappa^2}\right]$	Exponential	Exponential
\in	$\left(-\infty, -\frac{a_2^2}{4\kappa^2}\right)$	Exponential	Trigonometric
\in	$\left(\frac{a_1^2}{4\kappa^2}, \infty\right)$	Trigonometric	Exponential

While the expressions in (3.4)–(3.5) are correct mathematically and $c_k^E(x, y) = F_k(x)G_k(y)$ solves $\mathcal{L}c_k^E = 0$ for any choice of $k \in \mathbb{R}$, there is a practical issue that is worth addressing: it is unclear how the parameter k should be selected to generate a particular enrichment basis, since this parameter can take on any real value from $-\infty$ to ∞ . To this effect, it is recalled here that when DEM was tailored to the 2D Helmholtz equation $-\Delta c - k^2 c = 0$ in [56], the enrichment space \mathcal{V}^E consisted of a superposition of two-dimensional plane waves $c^E|_{\Omega^e} = e^{ikx \cos \theta_p} e^{iky \sin \theta_p}$ (where, again, $i \equiv \sqrt{-1}$), propagating in directions $\theta_p \in [0, 2\pi)$. The fact that the basis functions for the Helmholtz equation were specified by an angle proved to be very convenient as it made possible the systematic design of DEM elements of arbitrary orders: to design an element of order n^E , one simply selected n^E plane waves propagating in n^E different directions. Guided by DEM for the Helmholtz equation, an expression for c^E is sought after here in which the constant k is replaced by some angle parameter. The derivation of a parametrization of this sort is detailed below.

Case 1: Free-space solutions that are exponential in x and y

Suppose $k \in \left[-\frac{a_2^2}{4\kappa^2}, \frac{a_1^2}{4\kappa^2}\right]$. Defining $\mu_1, \mu_2 \in \mathbb{R}$ by

$$\mu_1^2 \equiv a_2^2 + 4k\kappa^2, \quad \mu_2^2 \equiv a_1^2 - 4k\kappa^2, \quad (3.6)$$

the following identity holds

$$\mu_1^2 + \mu_2^2 = a_1^2 + a_2^2 \equiv |\mathbf{a}|^2. \quad (3.7)$$

Relation (3.7) motivates the following definition

$$\mu_1 \equiv |\mathbf{a}| \cos \theta_k, \quad \mu_2 \equiv |\mathbf{a}| \sin \theta_k, \quad (3.8)$$

for some angle parameter $\theta_k \in [0, 2\pi)$. Given this parameterization, equations (3.4) and (3.5) can be rewritten in terms of μ_1 and μ_2 as

$$F_k(x) = \exp \left\{ \frac{a_1 x}{2\kappa} \pm \frac{\mu_1}{2\kappa} x \right\}, \quad G_k(y) = \exp \left\{ \frac{a_2 y}{2\kappa} \pm \frac{\mu_2}{2\kappa} y \right\}, \quad (3.9)$$

so that

$$c^E(\mathbf{x}; \theta_k) = \text{span} \left\{ e^{\left(\frac{a_1 \pm |\mathbf{a}| \cos \theta_k}{2\kappa}\right)x} e^{\left(\frac{a_2 \pm |\mathbf{a}| \sin \theta_k}{2\kappa}\right)y} \right\}. \quad (3.10)$$

The natural interpretation of the angles θ_k is that they are flow directions. Each angle θ_k that appears in (3.10) specifies a function that “slopes” — that is, exhibits a sharp gradient — in some direction in \mathbb{R}^2 . Figure 3.1 shows plots of the enrichment basis functions for several angles θ_k .

Remark 3.1.1. *The parametrization of the exponential free-space solutions (3.10) has a natural extension to the constant-coefficient advection-diffusion equation (1.2) in three dimensions (3D) (Section 7.2 of the Appendix).*

Case 2: Free-space solutions that are exponential in x and trigonometric in y

Suppose $k < -\frac{a_2^2}{4\kappa^2}$. It follows that $a_1^2 - 4k\kappa^2 > 0$ and $a_2^2 + 4k\kappa^2 < 0$. Defining μ_3 and μ_4 as follows

$$\mu_3^2 \equiv a_1^2 - 4k\kappa^2 > 0, \quad \mu_4^2 \equiv -a_2^2 - 4k\kappa^2 > 0, \quad (3.11)$$

the following identity holds

$$\mu_3^2 - \mu_4^2 = a_1^2 + a_2^2 = |\mathbf{a}|^2. \quad (3.12)$$

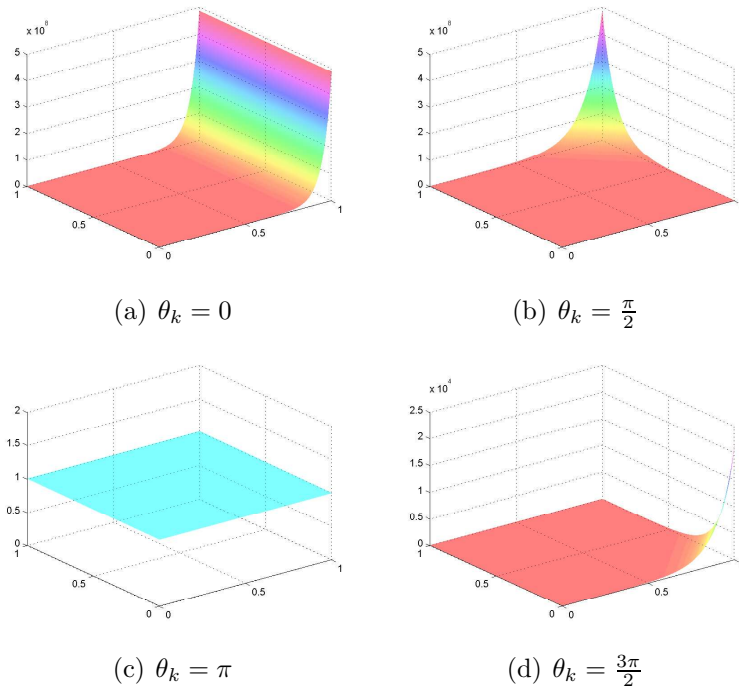


Figure 3.1: Plots of free-space solutions $c^E(\mathbf{x}; \theta_k)$ to the constant-coefficient advection-diffusion equation for Case 1 ($a_1/\kappa = 20$, $a_2/\kappa = 0$)

(3.12) motivates the definition of the following parametrization for Case 2:

$$\mu_3 \equiv |\mathbf{a}| \sec \theta_k, \quad \theta_k \neq \frac{n\pi}{2}, n \in \mathbb{Z}, \quad (3.13)$$

$$\mu_4 \equiv |\mathbf{a}| \tan \theta_k, \quad \theta_k \neq \frac{n\pi}{2}, n \in \mathbb{Z}. \quad (3.14)$$

Now, (3.4) and (3.5) can be rewritten in terms of μ_3 and μ_4 using (3.11):

$$F_k(x) = \exp \left\{ \frac{a_1 x}{2\kappa} \pm \frac{\mu_3}{2\kappa} x \right\}, \quad G_k(y) = \exp \left\{ \frac{a_2 y}{2\kappa} \pm i \frac{\mu_4}{2\kappa} y \right\}, \quad (3.15)$$

so that

$$c^E(\mathbf{x}; \theta_k) = \text{span} \left\{ e^{\left(\frac{a_1 + |\mathbf{a}| \sec \theta_k}{2\kappa} \right) x} e^{\left(\frac{a_2 + i |\mathbf{a}| \tan \theta_k}{2\kappa} \right) y} \right\}. \quad (3.16)$$

Using Euler's identity, (3.16) is equivalent to

$$c^E(\mathbf{x}; \theta_k) = \text{span} \left\{ e^{\left(\frac{a_1 + |\mathbf{a}| \sec \theta_k}{2\kappa} \right) x} e^{\frac{a_2}{2\kappa} y} \sin \left(\frac{|\mathbf{a}| \tan \theta_k}{2\kappa} y \right) \right\}. \quad (3.17)$$

Several representative functions (3.17) are plotted in Figure 3.2.

Case 3: Free-space solutions that are trigonometric in x and exponential in y

Suppose $k > \frac{a_1^2}{4\kappa^2}$. Now $a_1^2 - 4k\kappa^2 < 0$, so that $-a_1^2 + 4k\kappa^2 > 0$, and $a_2^2 + 4k\kappa^2 > 0$. Defining μ_5 and μ_6 by

$$\mu_5^2 \equiv -a_1^2 + 4k\kappa^2 > 0, \quad \mu_6^2 \equiv a_2^2 + 4k\kappa^2 > 0. \quad (3.18)$$

the following identity holds

$$\mu_6^2 - \mu_5^2 = a_1^2 + a_2^2 = |\mathbf{a}|^2. \quad (3.19)$$

Letting θ_k be an angle between 0 and 2π , define

$$\mu_5 \equiv |\mathbf{a}| \tan \theta_k, \quad \theta_k \neq \frac{n\pi}{2}, n \in \mathbb{Z}, \quad (3.20)$$

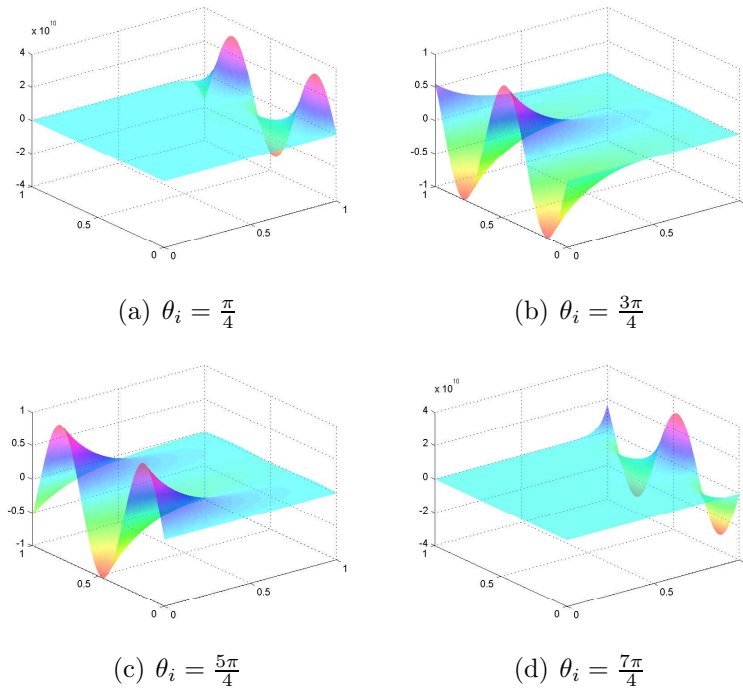


Figure 3.2: Plots of free-space solutions $c^E(\mathbf{x}; \theta_i)$ to the constant-coefficient advection-diffusion equation for Case 2 ($a_1/\kappa = 20, a_2/\kappa = 0$)

$$\mu_6 \equiv |\mathbf{a}| \sec \theta_k, \quad \theta_k \neq \frac{n\pi}{2}, n \in \mathbb{Z}. \quad (3.21)$$

In this case, (3.4) and (3.5) can be written in terms of μ_5 and μ_6 as

$$F_k(x) = \exp \left\{ \frac{a_1 x}{2\kappa} \pm \frac{i\mu_5}{2\kappa} x \right\}, \quad (3.22)$$

$$G_k(y) = \exp \left\{ \frac{a_2 y}{2\kappa} \pm \frac{\mu_6}{2\kappa} y \right\}, \quad (3.23)$$

so that

$$c^E(\mathbf{x}; \theta_k) = \text{span} \left\{ e^{\left(\frac{a_1 + i|\mathbf{a}| \tan \theta_k}{2\kappa}\right)x} e^{\left(\frac{a_2 + |\mathbf{a}| \sec \theta_k}{2\kappa}\right)y} \right\}, \quad (3.24)$$

or, employing Euler's identity,

$$c^E(\mathbf{x}; \theta_k) = \text{span} \left\{ e^{\frac{a_1}{2\kappa}x} \sin \left(\frac{|\mathbf{a}| \tan \theta_k}{2\kappa} x \right) e^{\left(\frac{a_2 + |\mathbf{a}| \sec \theta_k}{2\kappa}\right)y} \right\}. \quad (3.25)$$

The functions (3.25) are shown in Figure 3.3 for several angles θ_k .

3.1.2 Polynomial solutions

There exists also a family of polynomial free-space solutions to (1.2) with spatially-constant \mathbf{a} . The two lowest degree polynomials that solve this PDE can be found by inspection:

$$c_1^E = 1, \quad (3.26)$$

$$c_2^E = |\tilde{\mathbf{a}} \times \mathbf{x}| = |\tilde{a}_2 x - \tilde{a}_1 y|, \quad (3.27)$$

in 2D (up to an additive and multiplicative constant), where

$$\tilde{\mathbf{a}} \equiv \frac{\mathbf{a}}{\kappa}. \quad (3.28)$$

Higher degree polynomial free-space solutions to (1.2) can be derived as well. In general, an n^{th} degree polynomial of the form

$$c_n^E(x, y) = |\tilde{\mathbf{a}} \times \mathbf{x}|^n + f_n(x, y), \quad (3.29)$$

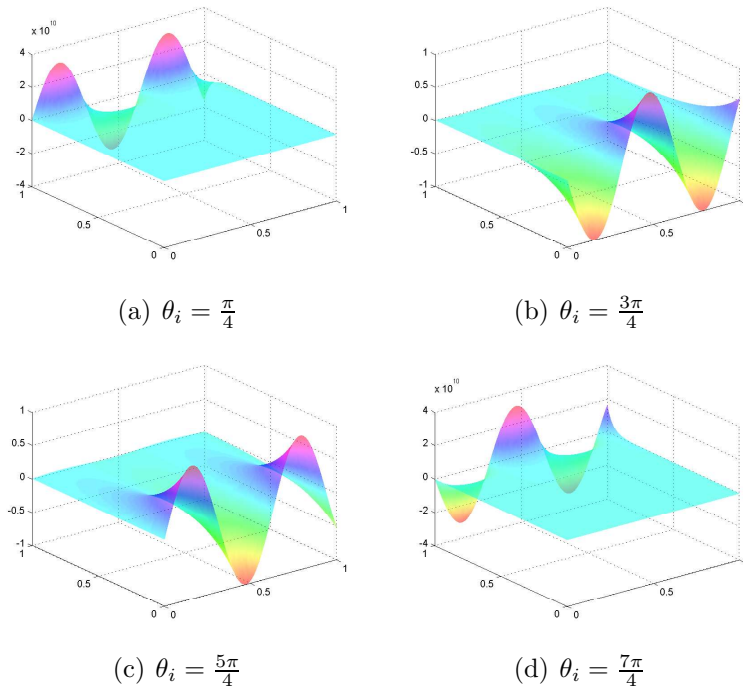


Figure 3.3: Plots of free-space solutions $c^E(\mathbf{x}; \theta_i)$ to the constant-coefficient advection-diffusion equation for Case 3 ($a_1/\kappa = 20, a_2/\kappa = 0$)

solves (1.2) where f_n is an $(n - 1)$ order polynomial that satisfies

$$\mathcal{L}f_n = n(n - 1)(\tilde{a}_2x - \tilde{a}_1y)^{n-2}|\tilde{\mathbf{a}}|^2. \quad (3.30)$$

Solutions to (3.30) can be obtained by assuming the following functional form for f_n

$$f_n(x, y) = \sum_{m=0}^{n-1} \sum_{k=0}^m c_{km} x^{m-k} y^k, \quad (3.31)$$

substituting (3.31) into (3.30), matching coefficients and solving a linear system for the coefficients c_{km} . Although this algebra is admittedly cumbersome, it is possible to semi-automate the derivation process using a symbolic software, such as Maple [61] or MATLAB's [62] symbolic toolbox. The second through fifth degree polynomial solutions to (1.2) derived in this way are given below.

$$c_2^E = (\tilde{a}_2x - \tilde{a}_1y)^2 + 2(\tilde{\mathbf{a}} \cdot \mathbf{x}), \quad (3.32)$$

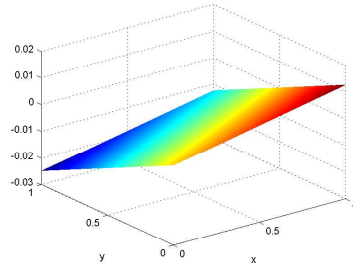
$$c_3^E = (\tilde{a}_2x - \tilde{a}_1y)^3 + 6(\tilde{a}_2x - \tilde{a}_1y)(\tilde{\mathbf{a}} \cdot \mathbf{x}), \quad (3.33)$$

$$c_4^E = \begin{cases} (\tilde{a}_2x - \tilde{a}_1y)^4 + 8\tilde{a}_1\tilde{a}_2^2x^3 + (-12\tilde{a}_1^2 - 12\tilde{a}_2^2)x^2 + \\ (12\tilde{a}_2^3 - 12\tilde{a}_1^2\tilde{a}_2)yx^2 + \left(24\frac{\tilde{a}_1^3}{\tilde{a}_2} + 24\tilde{a}_1\tilde{a}_2\right)yx - \\ 24\tilde{a}_1\tilde{a}_2^2xy^2 + \left(4\frac{\tilde{a}_1^4}{\tilde{a}_2} + 12\tilde{a}_1^2\tilde{a}_2\right)y^3 + (12\tilde{a}_1^2 + 12\tilde{a}_2^2)y^2, & \text{if } \tilde{a}_2 \neq 0 \\ \tilde{a}_1^4y^4 + 12\tilde{a}_1^3xy^2 + \frac{1}{6}\tilde{a}_1^3y^3 + 12\tilde{a}_1^2x^2 + \tilde{a}_1^2xy - 12\tilde{a}_1^2y^2, & \text{if } \tilde{a}_2 = 0 \end{cases}, \quad (3.34)$$

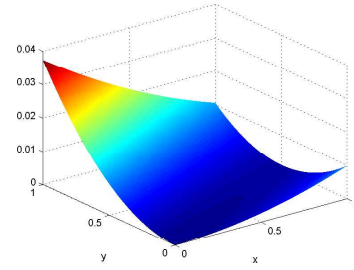
$$c_5^E = (\tilde{a}_2x - \tilde{a}_1y)^5 + 20\tilde{a}_1\tilde{a}_2^3x^4 + (-60\tilde{a}_1^2\tilde{a}_2^2 + 20\tilde{a}_2^4)x^3y + (60\tilde{a}_1^3\tilde{a}_2 - 60\tilde{a}_1\tilde{a}_2^3)x^2y^2 - \\ 20\tilde{a}_1^2(-3\tilde{a}_2^2 + \tilde{a}_1^2)xy^3 - 20\tilde{a}_1^3\tilde{a}_2y^4 + 20\tilde{a}_2(3\tilde{a}_1^2 - \tilde{a}_2^2)x^3 + (-60\tilde{a}_1^3 + 180\tilde{a}_2^2\tilde{a}_1)x^2y - \\ 60\tilde{a}_2(3\tilde{a}_1^2 - \tilde{a}_2^2)xy^2 + (20\tilde{a}_1^3 - 60\tilde{a}_2^2\tilde{a}_1)y^3. \quad (3.35)$$

The functions (3.27) and (3.32)–(3.35) are shown in Figure 3.4 for some specified values of a_1, a_2 and κ .

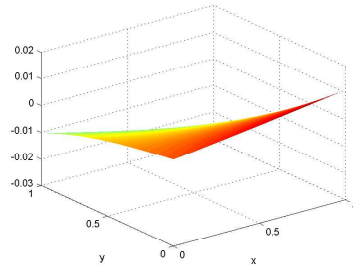
Remark 3.1.2. *A careful inspection of polynomial free-space solutions to (1.2) up to degree nine suggests that there is only one linearly independent polynomial that solves*



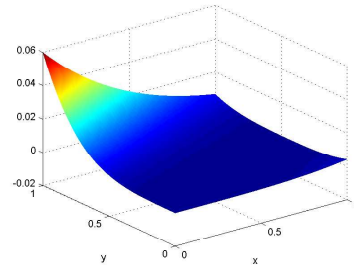
(a) Degree 1



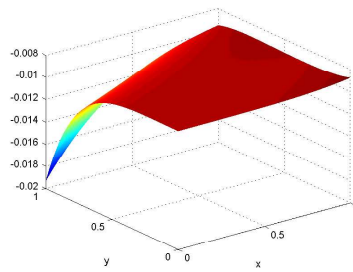
(b) Degree 2



(c) Degree 3



(d) Degree 4



(e) Degree 5

Figure 3.4: Plots of polynomial free-space solutions to the constant-coefficient advection-diffusion equation ($a_1/\kappa = 10, a_2/\kappa = 5$)

(1.2) of each order. In particular, assuming a polynomial of the form

$$c_n^E(x, y) = \sum_{m=0}^n \sum_{k=0}^m c_{km} x^{m-k} y^k \quad (3.36)$$

instead of the more specific functional form (3.29) yields the same polynomial, up to an additive and/or multiplicative constant.

3.2 Free-space solutions to the 2D advection-diffusion equation with $\mathbf{a}(\mathbf{x}) = \mathbf{A}\mathbf{x} + \mathbf{b}$

Consider now an advection-diffusion equation in which the advection field is linear in \mathbf{x} , that is:

$$[\mathbf{A}\mathbf{x} + \mathbf{b}] \cdot \nabla c^E - \Delta c^E = 0, \quad (3.37)$$

where \mathbf{A} is a constant 2×2 matrix, and $\mathbf{b} \in \mathbb{R}^2$ is a vector of constants¹. Assume \mathbf{A} is diagonalizable, and let \mathbf{v}_i for $i = 1, 2$ be the eigenvectors of \mathbf{A}^T , with corresponding eigenvalues², denoted by σ_i :

$$\mathbf{A}^T \mathbf{v}_i = \sigma_i \mathbf{v}_i. \quad (3.38)$$

It is possible to derive analytically free-space solutions to the variable-coefficient advection-diffusion equation (3.37).

Define first the change of variables, for $i = 1, 2$:

$$z_i \equiv \mathbf{v}_i \cdot \mathbf{x} = v_i(1)x + v_i(2)y, \quad (3.39)$$

where $v_i(j)$ denotes the j^{th} component of the eigenvector \mathbf{v}_i for $j = 1, 2$, so that, by the chain rule:

$$\begin{pmatrix} \frac{\partial}{\partial x} \\ \frac{\partial}{\partial y} \end{pmatrix} = \begin{pmatrix} \frac{\partial z_i}{\partial x} \frac{\partial}{\partial z_i} \\ \frac{\partial z_i}{\partial y} \frac{\partial}{\partial z_i} \end{pmatrix} = \begin{pmatrix} v_i(1) \frac{\partial}{\partial z_i} \\ v_i(2) \frac{\partial}{\partial z_i} \end{pmatrix}, \quad (3.40)$$

¹Note that the diffusivity κ in (3.37) has been absorbed into the matrix \mathbf{A} and vector \mathbf{b} .

²Note that there is no implied summation on repeated indices i in (3.38) and the subsequent expressions in Section 3.2.

or

$$\nabla_{\mathbf{x}} = \mathbf{v}_i \frac{\partial}{\partial z_i}, \quad (3.41)$$

for $i = 1, 2$. Also by the chain rule,

$$\frac{\partial^2}{\partial x^2} = \frac{\partial}{\partial x} \left(\frac{\partial}{\partial x} \right) = \frac{\partial z_i}{\partial x} \frac{\partial}{\partial z_i} \left(\frac{\partial}{\partial x} \right) = v_i(1) \frac{\partial}{\partial z_i} \left(v_i(1) \frac{\partial}{\partial z_i} \right) = v_i^2(1) \frac{\partial^2}{\partial z_i^2}, \quad (3.42)$$

and similarly

$$\frac{\partial^2}{\partial y^2} = v_i^2(2) \frac{\partial^2}{\partial z_i^2}, \quad (3.43)$$

so that

$$\frac{\partial^2}{\partial x^2} + \frac{\partial^2}{\partial y^2} = \underbrace{|\mathbf{v}_i|^2}_{=1} \frac{\partial^2}{\partial z_i^2} = \frac{\partial^2}{\partial z_i^2}, \quad (3.44)$$

assuming the eigenvectors of \mathbf{A} have been normalized.

Now, substituting (3.44), (3.41) and (3.38) into (3.37) gives

$$[\mathbf{x}^T \mathbf{A}^T + \mathbf{b}^T] \mathbf{v}_i \frac{\partial c}{\partial z_i} - \frac{\partial^2 c}{\partial z_i^2} = [\mathbf{x}^T \underbrace{\mathbf{A}^T \mathbf{v}_i}_{\sigma_i \mathbf{v}_i} + \mathbf{b}^T \mathbf{v}_i] \frac{\partial c}{\partial z_i} - \frac{\partial^2 c}{\partial z_i^2} = 0, \quad (3.45)$$

for $i = 1, 2$. By (3.39), $\mathbf{x}^T \sigma_i \mathbf{v}_i = \sigma_i \mathbf{x}^T \mathbf{v}_i = \sigma_i z_i$, so that (3.45) can be written in terms of z_i only:

$$\frac{\partial^2 c}{\partial z_i^2} - [\sigma_i z_i + \mathbf{v}_i \cdot \mathbf{b}] \frac{\partial c}{\partial z_i} = 0, \quad (3.46)$$

for $i = 1, 2$.

To solve (3.46), let $\tilde{c}_i \equiv \frac{\partial c}{\partial z_i}$. Then (3.46) becomes

$$\frac{\partial \tilde{c}_i}{\partial z_i} - [\sigma_i z_i + \mathbf{v}_i \cdot \mathbf{b}] \tilde{c}_i = 0. \quad (3.47)$$

(3.47) is a separable ODE, that can be integrated:

$$\int \frac{\partial \tilde{c}_i}{\tilde{c}_i} = \int [\sigma_i z_i + \mathbf{v}_i \cdot \mathbf{b}] dz_i \quad \Rightarrow \quad \ln \tilde{c}_i = \frac{\sigma_i z_i^2}{2} + (\mathbf{v}_i \cdot \mathbf{b}) z_i + \text{const}_1, \quad (3.48)$$

or

$$\frac{\partial c}{\partial z_i} \equiv \tilde{c}_i = K_1 \exp \left\{ \frac{\sigma_i z_i^2}{2} + (\mathbf{v}_i \cdot \mathbf{b}) z_i \right\}, \quad (3.49)$$

for some constant K_1 . Integrating (3.49), the solution

$$c(z_i) = K_1 \int_0^{z_i} \exp \left\{ \frac{\sigma_i w^2}{2} + (\mathbf{v}_i \cdot \mathbf{b}) w \right\} dw + K_2, \quad (3.50)$$

is obtained, for some other constant K_2 . Finally, substituting the transformation (3.39) into (3.50), the solution to (3.37) is obtained, namely

$$c^E(\mathbf{x}) = K_1 \int_0^{\mathbf{v}_i \cdot \mathbf{x}} \exp \left\{ \frac{\sigma_i w^2}{2} + (\mathbf{v}_i \cdot \mathbf{b}) w \right\} dw + K_2. \quad (3.51)$$

By definition, the eigenvalues σ_i of \mathbf{A} are roots of the characteristic polynomial of \mathbf{A} , that is, they are solutions to the following quadratic equation

$$\sigma_i^2 - \underbrace{\text{tr}(\mathbf{A})}_{\equiv \tau} \sigma_i + \underbrace{\det(\mathbf{A})}_{\equiv \Delta} = 0, \quad (3.52)$$

where $\text{tr}(\cdot)$ and $\det(\cdot)$ denote the trace and determinant of a matrix, respectively. By the quadratic formula:

$$\sigma_i = \frac{\tau \pm \sqrt{\tau^2 - 4\Delta}}{2}. \quad (3.53)$$

For $\sigma_i \neq 0$, (3.51) can be simplified nicely using the *error function* $\text{erf}(\cdot)$:

$$\int_0^{\mathbf{v}_i \cdot \mathbf{x}} \exp \left\{ \frac{\sigma_i w^2}{2} + (\mathbf{v}_i \cdot \mathbf{b}) w \right\} dw = \frac{1}{2} \sqrt{\frac{2\pi}{-\sigma_i}} e^{-\frac{(\mathbf{v}_i \cdot \mathbf{b})^2}{2\sigma_i}} \left[\text{erf} \left\{ \frac{\sqrt{-2\sigma_i}}{2} \left((\mathbf{v}_i \cdot \mathbf{x}) + \frac{\mathbf{v}_i \cdot \mathbf{b}}{\sigma_i} \right) \right\} - \text{erf} \left\{ \frac{\sqrt{-2\sigma_i}}{2} \left(\frac{\mathbf{v}_i \cdot \mathbf{b}}{\sigma_i} \right) \right\} \right], \quad (3.54)$$

where

$$\text{erf}(x) \equiv \frac{2}{\sqrt{\pi}} \int_0^x e^{-t^2} dt. \quad (3.55)$$

The character of the solutions (3.51) depends on the eigenvalues of \mathbf{A} . Figure 3.5 illustrates a typical function (3.51) for $\sigma_i \in \mathbb{R}$; Figure 3.6 illustrates this function for $\sigma_i \in \mathbb{C}$ with $\mathcal{I}(\sigma_i) \neq 0$, where $\mathcal{I}(z)$ denotes the imaginary part of a complex number

$z \in \mathbb{C}$. Note that, in this latter case, the function $c^E(\mathbf{x})$ (3.54) is complex-valued.

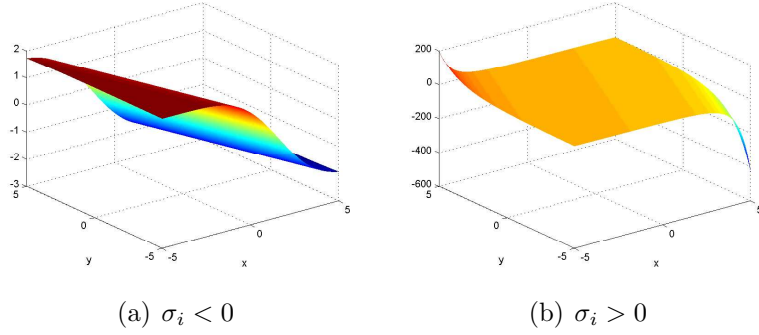


Figure 3.5: Free-space solution (3.51) for $\sigma_i \in \mathbb{R}$

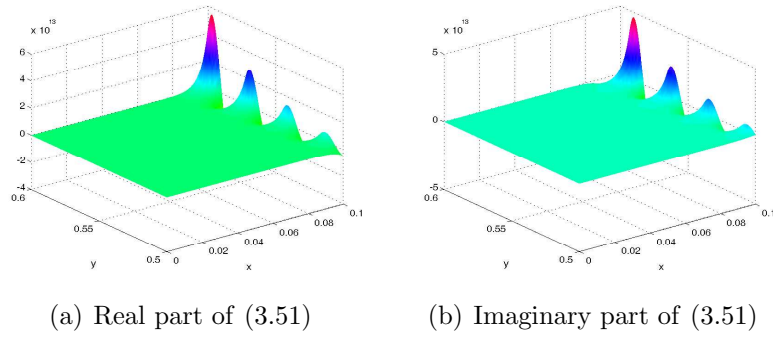


Figure 3.6: Free-space solution (3.51) for $\sigma_i \in \mathbb{C}$

In the case when $\sigma_i = 0$ but $\mathbf{v}_i \cdot \mathbf{b} \neq 0$, the free-space solutions (3.51) evaluate to:

$$c^E(\mathbf{x}) = K_1 \int_0^{\mathbf{v}_i \cdot \mathbf{x}} e^{\mathbf{v}_i \cdot \mathbf{b} w} dw + K_2 = \frac{K_1}{\mathbf{v}_i \cdot \mathbf{b}} [e^{(\mathbf{v}_i \cdot \mathbf{b})(\mathbf{v}_i \cdot \mathbf{x})} - 1] + K_2. \quad (3.56)$$

Remark 3.2.1. Another family of free-space solutions to (3.37) is given in Section 7.3 of the Appendix for the specific case when \mathbf{A} is orthogonally diagonalizable, that is, \mathbf{A} is diagonalizable by an orthogonal matrix. This is the case if \mathbf{A} is, for example, symmetric.

Chapter 4

DEM for the 2D constant-coefficient advection-diffusion equation

This chapter is devoted specifically to the development of DEM for constant-coefficient transport problems. The methodology described in this chapter has a natural extension to variable-coefficient problems, discussed specifically in Chapter 5.

4.1 The enrichment space \mathcal{V}^E

In Section 3.1, several families of free-space solutions to (1.2) when $\mathbf{a} \in \mathbb{R}^2$ is spatially constant were derived. In DEM, these free-space solutions are used to define the enrichment space $\mathcal{V}^E \subset \mathcal{V}^h$ (Section 2.3). In this chapter, only the exponential free-space solutions derived in Section 3.1.1 (Case 1) will be employed in the design of the enrichment space \mathcal{V}^E . In particular, the oscillatory functions derived in Section 3.1.1 (Cases 2 and 3) will be omitted from the enrichment space \mathcal{V}^E on grounds that, unless there is a trigonometric source in equation (2.1), the solutions of these BVPs do *not* exhibit an oscillatory behavior. Rather, they exhibit however sharp *exponential* boundary layers (*cf.* Section 4.5.1–4.5.3) in which the velocity profile rises or falls sharply, much like the functions in the first case of Table 3.1. Since the objective here

is to capture exponential layers, the polynomial free-space solutions to (2.1) with $\mathbf{a} \in \mathbb{R}^2$ derived in Section 3.1.2 will not be employed in the design of \mathcal{V}^E either.

To this effect, let

$$\mathcal{V}^E \equiv \left\{ c^E \in L^2(\tilde{\Omega}) : c|_{\Omega^e}^E(x, y) = \sum_{i=1}^{n^E} c_i e^{\left(\frac{a_1 + |\mathbf{a}| \cos \theta_i}{2\kappa}\right)(x - x_{r,i}^e)} e^{\left(\frac{a_2 + |\mathbf{a}| \sin \theta_i}{2\kappa}\right)(y - y_{r,i}^e)}, \right. \\ \left. c_i \in \mathbb{R}, 0 \leq \theta_i \leq 2\pi \right\}. \quad (4.1)$$

The constants c_i that appear in (4.1) are the unknown degrees of freedom (dofs) to be solved for in computing the solution by DEM. The integer n^E is the number of enrichment functions (the dimension of the space \mathcal{V}^E), selected *a priori* in designing an enriched element. In (4.1), $\mathbf{x}_r^e = (x_{r,i}^e \ y_{r,i}^e)^T \in \mathbb{R}^2$ is an arbitrary reference point assigned to element Ω^e for the i^{th} enrichment. This reference point has the practical purpose of scaling the enrichment functions to prevent them from evaluating to a very large number on a finite precision arithmetic machine. Further discussion of the reference point is deferred until Section 4.4.3. The Greek letter ϕ will be used to denote the given advection direction, implied by the advection coefficients a_1 and a_2 , and defined by

$$a_1 = |\mathbf{a}| \cos \phi, \quad a_2 = |\mathbf{a}| \sin \phi, \quad (4.2)$$

(Figure 4.2).

The natural interpretation of the angles θ_i that appear in (4.1) is that they are flow directions. Figure 4.1 displays a graphical representation of the argument of the exponential in (4.1), namely

$$\mathbf{a}_\phi + \mathbf{a}_{\theta_i} \equiv \begin{pmatrix} a_1 + |\mathbf{a}| \cos \theta_i \\ a_2 + |\mathbf{a}| \sin \theta_i \end{pmatrix} \in \mathbb{R}^2, \quad (4.3)$$

where

$$\mathbf{a}_{\theta_i}^T \equiv |\mathbf{a}| \begin{pmatrix} \cos \theta_i, & \sin \theta_i \end{pmatrix}. \quad (4.4)$$

In particular, for $\theta_i \in [0, 2\pi)$, the vectors (4.3) can be represented by a circle of radius $|\mathbf{a}|$ centered at (a_1, a_2) in the Euclidian plane. Each exponential enrichment

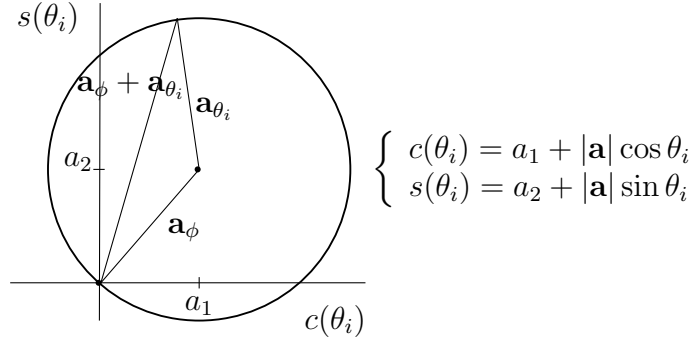


Figure 4.1: Graphical representation of enrichment arguments (4.3) as a circle of radius $|\mathbf{a}|$ centered at $\mathbf{a} \in \mathbb{R}^2$

function (3.10) specified by an angle $\theta_i \in [0, 2\pi)$ exhibits a boundary layer in the direction of the vector (4.3) (Figure 3.1). Not only does the parameterization of the exponential enrichment functions (4.1) with respect to an angle parameter fit in nicely with the problem at hand, it also facilitates the design and implementation of DGM/DEM elements of arbitrary orders: to design an element of order n^E , one simply selects n^E angles $\theta_i \in [0, 2\pi)$. Each of these angles defines a basis function of the form (3.10). The set of angles $\{\theta_i\}$ specifying an enrichment basis is denoted by

$$\Theta^c \equiv \left\{ \text{set of angles } \{\theta_i \in [0, 2\pi)\}_{i=1}^{n^E} \text{ defining } \mathcal{V}^E \right\}. \quad (4.5)$$

One strategy for constructing a space \mathcal{V}^E of dimension n^E is to select the angles $\{\theta_i\} \in \Theta^c$ such that the enrichment functions specify “slope” — that is, exhibit a sharp gradient — in n^E different directions (Section 4.3).

Remark 4.1.1. *Of particular interest is the relationship between θ_i and the advection direction ϕ implied by the advection coefficients a_1 and a_2 . Setting $\theta_i = \phi$, where ϕ (4.2) is the advection direction defined by (4.2), in (3.10), one finds that $c^E(\mathbf{x}; \phi)$ simplifies to*

$$c^E(\mathbf{x}; \phi) = e^{a_1(x-x_r^e)} e^{a_2(y-y_r^e)}. \quad (4.6)$$

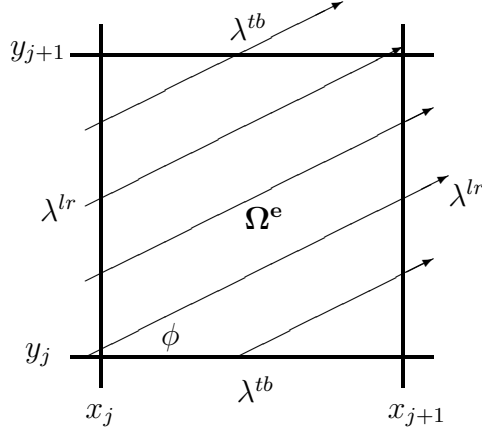


Figure 4.2: Flow at an angle ϕ over $\Omega^e = (x_j, x_{j+1}) \times (y_j, y_{j+1})$

The function (4.6) has the property that

$$\nabla c^E(\mathbf{x}; \phi) = \mathbf{a}c^E(\mathbf{x}; \phi). \quad (4.7)$$

The gradient of a function points in the direction in which that function changes most rapidly; therefore (4.7) implies that the enrichment function specified by $\theta_i = \phi$ rises most rapidly precisely in the direction of the advection ϕ . There is therefore the motivation to always include $\theta_i = \phi$ in the set Θ^c specifying the enrichment basis of a DGM or DEM element designed to solve a problem with advection velocities a_1 and a_2 . This idea is explored further in Section 4.3.

Remark 4.1.2. Note that a constant is a free-space solution of the advection-diffusion equation (1.2) and

$$c^E(\mathbf{x}; \phi + \pi) = 1. \quad (4.8)$$

This property will be exploited in designing certain kinds of DGM elements (Section 4.3).

4.2 The Lagrange multiplier approximation space

 \mathcal{W}^h

As outlined in Section 2.3.3, the variational form of the problem suggests appropriate Lagrange multiplier approximations are the normal derivatives of the enrichment functions on the element interfaces. In the case of a spatially-constant coefficient transport problem, the Lagrange multiplier approximations (2.54) are well defined given the enrichment space \mathcal{V}^E (4.1) – in fact they can be computed from (4.1) simply by taking the normal derivatives of these functions on each element edge. In the following subsection, an appropriate functional form for the Lagrange multiplier approximations on unstructured meshes of quadrilateral straight-edged elements (Figure 4.3) is inferred by computing these normal derivatives analytically per the formula suggested by (2.54).

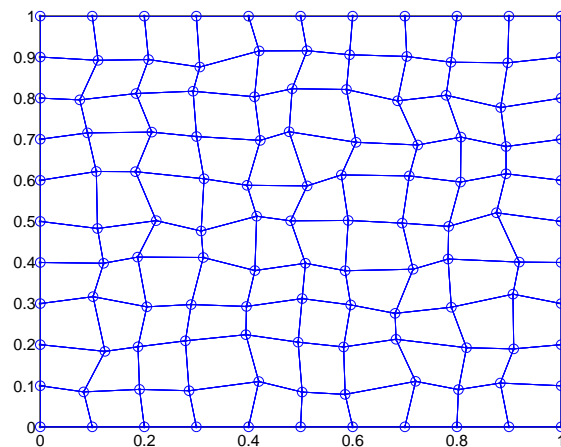


Figure 4.3: Sample unstructured mesh of 100 quadrilateral elements

4.2.1 Derivation of the Lagrange multiplier approximations on an element edge

Let Γ^{ij} be a straight edge separating two adjacent elements Ω^{e_i} and Ω^{e_j} , but viewed as an edge belonging to Ω^{e_i} . Let $\mathbf{x}_0^{ij} = (x_0^{ij}, y_0^{ij})$ and $\mathbf{x}_1^{ij} = (x_1^{ij}, y_1^{ij})$ be the coordinates of this edge, labeled with respect to a right-handed coordinate system so that the outward normal \mathbf{n}^{ij} to Ω^{e_i} points to the right of Ω^{e_i} (Figure 4.4). Parameterize this edge with respect to an arc-length coordinate $0 \leq s \leq l^{ij}$, where l^{ij} is the length of this edge. Let $\alpha^{ij} \in [0, \frac{\pi}{2}]$ denote the angle Γ^{ij} makes with the x -axis, defined by

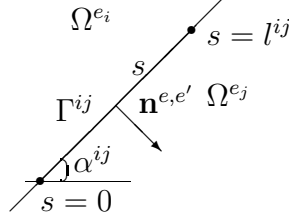


Figure 4.4: Straight edge of element Ω^{e_i} oriented at angle α^{ij}

$$\begin{cases} \Delta x^{ij} = l^{ij} \cos \alpha^{ij}, \\ \Delta y^{ij} = l^{ij} \sin \alpha^{ij}, \end{cases} \quad (4.9)$$

where

$$\Delta x^{ij} \equiv x_1^{ij} - x_0^{ij}, \quad \Delta y^{ij} \equiv y_1^{ij} - y_0^{ij}. \quad (4.10)$$

Then the unit tangent vector to Γ^{ij} , \mathbf{t}^{ij} , is given by

$$\mathbf{t}^{ij} = \frac{1}{l^{ij}} \begin{pmatrix} \Delta x^{ij} & \Delta y^{ij} \end{pmatrix}^T = \begin{pmatrix} \cos \alpha^{ij} & \sin \alpha^{ij} \end{pmatrix}^T \equiv \begin{pmatrix} t_1^{ij} & t_2^{ij} \end{pmatrix}^T, \quad (4.11)$$

so that

$$\mathbf{n}^{ij} = \begin{pmatrix} t_2^{ij} & -t_1^{ij} \end{pmatrix}^T. \quad (4.12)$$

Now, Γ^{ij} can be parameterized with respect to the arc length coordinate s as follows

$$\Gamma^{ij} : \begin{cases} x = x_0^{ij} + t_1^{ij} s \\ y = y_0^{ij} + t_2^{ij} s \end{cases}, \quad 0 \leq s \leq l^{ij}. \quad (4.13)$$

As outlined in Section 4.1, the first step in defining the space \mathcal{V}^E of a DGM or DEM element is to select the set Θ^c that defines the element's enrichment basis. Given the parametrization of Γ^{ij} (4.13) and the set Θ^c (4.5), one can begin by computing the corresponding Lagrange multiplier approximations according to (2.54)

$$\lambda^h(s)|_{\Gamma^{ij}} = \sum_{k=1}^{n^E} \lambda_k \exp \left\{ \underbrace{\frac{1}{2} [(\mathbf{a}_\phi + \mathbf{a}_{\theta_k}) \cdot \mathbf{t}^{ij}] (s - s_{r,k}^{ij})}_{\equiv \lambda^h(s; \theta_k)} \right\}, \quad 0 \leq s \leq l^{ij}, \quad (4.14)$$

where \mathbf{t}^{ij} is the unit tangent vector to Γ^{ij} defined in (4.11), $s_{r,k}^{ij}$ is an arbitrary reference point and the λ_k are the unknown multiplier dofs. Substituting the expression of \mathbf{t}^{ij} (4.11) into the above result and applying some trigonometric identities transforms (4.14) into

$$\lambda^h(s)|_{\Gamma^{ij}} = \sum_{k=1}^{n^E} \lambda_k \exp \left\{ \underbrace{\frac{|\mathbf{a}|}{2} [\cos(\phi - \alpha^{ij}) + \cos(\theta_k - \alpha^{ij})] (s - s_{r,k}^{ij})}_{\equiv \lambda^h(s; \theta_k)} \right\}, \quad 0 \leq s \leq l^{ij}. \quad (4.15)$$

Example 4.2.1. *In a uniform mesh aligned with the x - and y -coordinate axes, $\alpha^{ij} = 0, \pi$ for the top/bottom edges of each element and $\alpha^{ij} = \frac{\pi}{2}, \frac{3\pi}{2}$ for the left/right edges of each element. For these values, (4.15) reduces to the formulas*

$$\begin{aligned} \lambda^{tb} &= \sum_{i=1}^{n^E} \lambda_i^{tb} \exp \left\{ \frac{|\mathbf{a}|}{2} (\cos \phi + \cos \theta_i) (x - x_{r,i}) \right\}, \quad x_j \leq x \leq x_{j+1}, \\ \lambda^{lr} &= \sum_{i=1}^{n^E} \lambda_i^{lr} \exp \left\{ \frac{|\mathbf{a}|}{2} (\sin \phi + \sin \theta_i) (y - y_{r,i}) \right\}, \quad y_j \leq y \leq y_{j+1}, \end{aligned} \quad (4.16)$$

for an element $\Omega^e = (x_j, x_{j+1}) \times (y_j, y_{j+1}) \subset \mathbb{R}^2$. Here, λ^{tb} and λ^{lr} denote the Lagrange multiplier approximations on the top/bottom and left/right edges in the mesh,

respectively (Figure 4.2).

4.2.2 Lagrange multiplier selection and truncation

Before presenting a general algorithm for designing a DGM or DEM element of an arbitrary order (Algorithm 2 in Section 4.3.1), two problems that can be encountered in element design are illustrated.

Problem 1: Too many Lagrange multipliers

As it turns out, The set Θ^c (4.5) typically leads to too many Lagrange multiplier dofs (4.14) in the sense that condition (2.49) fails. For this reason, the space of approximation of the Lagrange multiplier field is constructed as $\mathcal{W}^h = \cup_e \cup_{e_j < e_i} \mathcal{W}_{ij}^h$ where

$$\mathcal{W}_{ij}^h = \left\{ \lambda^h \in L^2(\Gamma^{ij}) : \lambda^h(s)|_{\Gamma^{ij}} = \sum_{k=1}^{n^\lambda} \lambda_k \exp\left(\frac{1}{2} \left[(\mathbf{a}_\phi + \mathbf{a}_{\theta_k^\lambda}) \cdot \mathbf{t}^{ij} \right] (s - s_{r,k}^{ij}) \right), \right. \\ \left. 0 \leq s \leq l^{ij}, 0 \leq \theta_k^\lambda < 2\pi, \lambda_k \in \mathbb{R} \right\}. \quad (4.17)$$

Here, $\{\theta_k^\lambda\}_{k=1}^{n^\lambda} = \Theta^\lambda$ is another set of angles that is defined *a priori* and independently from Θ^c , and n^λ is the number of Lagrange multiplier dofs *per edge*. This is discussed in more detail in Section 4.3, and illustrated in Figure 4.5 (b).

Problem 2: Lagrange multiplier redundancy (when $n^\lambda > 1$)

It is often the case that a “naïve” selection of the set Θ^λ to define \mathcal{W}^h causes a Lagrange multiplier redundancy on some edge in the mesh. For example, suppose $\Theta^\lambda = \{\theta_1^\lambda = 0, \theta_2^\lambda = \pi\}$ and $\alpha^{ij} = \frac{\pi}{2}$ for a particular edge Γ^{ij} . Suppose the flow is being advected from left to right, so $\phi = 0$. Then, from (4.15),

$$\lambda^h|_{\Gamma^{ij}}(s; \theta_1^\lambda = 0) = \lambda^h|_{\Gamma^{ij}}(s; \theta_2^\lambda = \pi) = 1 \quad (4.18)$$

Both angles $\theta_1^\lambda = 0$ and $\theta_2^\lambda = \pi$ define the same, constant Lagrange multiplier; that

is, they define Lagrange multipliers that are redundant. Including the Lagrange multipliers corresponding to these two angles will result in a singular global interface problem. This situation must therefore be avoided.

The following lemma defines a set of necessary conditions for the set Θ^λ to generate redundant Lagrange multiplier approximations. When $n^\lambda > 2$, one must check that *each pair* of angles in the proposed set Θ^λ does not verify any of these conditions before finalizing the design of a DGM or DEM element.

Lemma 4.2.2. *Two Lagrange multipliers $\lambda^h(s; \theta_1^\lambda)$ and $\lambda^h(s; \theta_2^\lambda)$ given by (4.14) (or equivalently (4.15)) on a straight edge Γ^{ij} parameterized by (4.13) are redundant (that is, $\lambda^h(s; \theta_1^\lambda) = C\lambda^h(s; \theta_2^\lambda)$ for some real constant C) if*

$$\frac{\theta_1^\lambda - \theta_2^\lambda}{2} = n\pi, \quad (4.19)$$

or

$$\frac{\theta_1^\lambda + \theta_2^\lambda}{2} = \alpha^{ij} + n\pi, \quad (4.20)$$

for any $n \in \mathbb{Z}$, where α^{ij} is the angle at which Γ^{ij} is oriented (Figure 4.4).

Proof. From (4.15), $\lambda^h(s; \theta_1^\lambda) = \lambda^h(s; \theta_2^\lambda)$ if

$$\cos(\theta_1^\lambda - \alpha^{ij}) = \cos(\theta_2^\lambda - \alpha^{ij}). \quad (4.21)$$

Clearly (4.21) holds if $\theta_1^\lambda = \theta_2^\lambda + 2n\pi$ for any $n \in \mathbb{Z}$, which proves (4.19). Since $\cos(\cdot)$ is even, (4.21) is equivalent to

$$\cos(\theta_1^\lambda - \alpha^{ij}) = \cos(\alpha^{ij} - \theta_2^\lambda), \quad (4.22)$$

which holds if $\theta_1^\lambda - \alpha^{ij} = \alpha^{ij} - \theta_2^\lambda + 2n\pi$ or $\frac{\theta_1^\lambda + \theta_2^\lambda}{2} = \alpha^{ij} + n\pi$ for $n \in \mathbb{Z}$. \square

4.3 DGM and DEM element design

4.3.1 General and mesh independent element design procedure

A general procedure for designing a DGM or DEM element with an enrichment space containing n^E exponential basis functions (4.1) is summarized in Algorithm 2. Condition (4.20) of Lemma 4.1 motivates choosing Θ^λ as a set of angles that are clustered around α^{ij} — that is,

$$\Theta^\lambda = \alpha^{ij} + \{\beta_k^\lambda\}_{k=1}^{n^\lambda}, \quad \{\beta_k^\lambda\}_{k=1}^{n^\lambda} \in [0, 2\pi), \quad (4.23)$$

in which case (4.15) simplifies to

$$\lambda^h(s)|_{\Gamma^{ij}} = \sum_{k=1}^{n^\lambda} \lambda_k \exp\left(\frac{|\mathbf{a}|}{2} [\cos(\phi - \alpha^{ij}) + \cos \beta_k^\lambda] (s - s_{r,k})\right), \quad (4.24)$$

for $0 \leq s \leq l^{ij}$. For the choice of angles (4.23), the necessary condition for redundancy (4.20) becomes

$$\frac{\theta_k^\lambda + \theta_l^\lambda}{2} = \alpha^{ij} + n\pi \quad \Leftrightarrow \quad \frac{\beta_k^\lambda + \beta_l^\lambda}{2} = n\pi, \quad (4.25)$$

for any two distinct $k, l \in \{1, 2, \dots, n^\lambda\}$. Since condition (4.25) is independent of α^{ij} , condition (4.20) is in this case (quadrilateral) mesh independent.

Remark 4.3.1. *A consequence of the element design approach outlined in Algorithm 1 is that, in general,*

$$\Theta^\lambda \not\subset \Theta^c. \quad (4.26)$$

Selecting Θ^λ independently of Θ^c is actually rather intuitive: since there are almost always more normal derivatives of the enrichment functions in \mathcal{V}^E than allowed by (2.49) and one does not know a priori which of these Lagrange multipliers are more important and should be kept in Θ^λ , and which are less important and can be omitted, a reasonable compromise is to define Θ^λ as some average of the angles in Θ^c . Indeed, in practice, the angles $\{\beta_k^\lambda\}_{k=1}^{n^\lambda}$ that define the set Θ^λ (4.23) are selected uniformly

Algorithm 2 DGM/DEM element design

Fix $n^E \in \mathbb{N}$, the desired number of angles defining the enrichment space \mathcal{V}^E (4.1).
 Select a set $\Theta^c = \{\theta_i\}_{i=1}^{n^E}$ of n^E distinct angles between $[0, 2\pi)$ which:
if designing a pure DGM element **then**
 Includes $\theta_i = \phi + \pi$ in Θ^c
else
 Omits $\theta_i = \phi + \pi$ from Θ^c .
end if
 Let $n^\lambda = \lfloor \frac{n^E}{4} \rfloor$.
 Choose a set of n^λ distinct angles $\{\beta_k^\lambda\}_{k=1}^{n^\lambda}$ between $[0, \pi)$.
for each edge $\Gamma^{ij} \in \Gamma_{\text{int}}$ having slope α^{ij} **do**
 Let $\Theta^\lambda = \alpha^{ij} + \{\beta_k^\lambda\}_{k=1}^{n^\lambda}$ be the set of angles defining the Lagrange multiplier approximations (4.17) on Γ^{ij} .
end for

between the angles $[0, \pi)$ so as to “cover” the \mathbb{R}^2 space in some way (Table 4.2).

4.3.2 Some 2D DGM and DEM elements for constant-coefficient advection-diffusion

Here, several low and higher-order quadrilateral DGM and DEM elements are proposed for the finite element solution of 2D constant-coefficient advection-diffusion problems on unstructured meshes. The notation used for describing these elements is summarized in Table 4.1. The letter ‘Q’ stands for ‘quadrilateral’. As before, n^E

Table 4.1: DGM and DEM Element Nomenclature

Element	$Pe \leq 10^3$	$Pe > 10^3$
DGM	$Q-n^E-n^\lambda$	$Q-n^E-n^\lambda$
DEM	$Q-n^E-n^{\lambda+}$	$Q-n^E-n^{\lambda+}$

denotes the number of enrichment functions (number of angles in the set Θ^c) and n^λ the number of Lagrange multiplier dofs per edge (number of angles in the set Θ^λ). Two cases are distinguished: $Pe \leq 10^3$ (small to moderate Péclet number regime),

and $Pe > 10^3$ (high Péclet number regime). In the latter case, the DGM and DEM elements are designed slightly differently to address some numerical issues and distinguished by the presence of a horizontal bar over their names ($\overline{\dots}$). The “+” superscript designates a true DEM element ($c^h = c^P + c^E$) and distinguishes it from a pure DGM element ($c^h = c^E$).

Since the approximation space \mathcal{V}^E is constructed independently from \mathcal{V}^P , the polynomial component of a DEM element can be set to that of any higher-order standard Galerkin element Q_n (see Section 7.1.1 of the Appendix), independently from the value of n^E . From a practical perspective, it is however unnecessary to do so because for most advection-diffusion problems, the benefit of including a higher-order polynomial approximation in a DEM element is already provided by the presence of the enrichment field in this element. For this reason and in order to maximize computational efficiency, all DEM elements described in this section share the same low-order polynomial component which is identical to that of the standard bilinear element Q_1 , that is,

$$Q\text{-}n^E\text{-}n^{\lambda+} \equiv [Q\text{-}n^E\text{-}n^\lambda] \cup [Q_1], \quad \overline{Q\text{-}n^E\text{-}n^{\lambda+}} \equiv [\overline{Q\text{-}n^E\text{-}n^\lambda}] \cup [Q_1]. \quad (4.27)$$

4.3.3 Element design for $Pe \leq 10^3$

Table 4.2 describes four DGM elements and four DEM elements designed according to the general procedure outlined in Section 4.3.1. For all these elements, the enrichment bases are defined by

$$\Theta^c = \{\theta_m\}_{m=1}^{n^E} \equiv \phi + \{\beta_m\}_{m=1}^{n^E}, \quad \beta_m = \frac{2(m-1)\pi}{n^E}. \quad (4.28)$$

where ϕ is the advection direction given in the problem (4.2).

Remark 4.3.2. *For all DEM elements in Table 4.2, n^E is chosen as an odd integer. This ensures that $\theta_i = \phi + \pi$, $n \in \mathbb{Z}$, is not included in Θ^c , and therefore the constant approximation is not included in this case in the enrichment field (see Remark 4.1.2). Note also that all values of n^λ are specified according to (2.50), all sets Θ^λ defining*

Table 4.2: Higher-order DGM and DEM elements

	Name	n^E	Θ^c	n^λ	Θ^λ
DGM	Q-4-1	4	$\phi + \left\{ \frac{m\pi}{2} : m = 0, \dots, 3 \right\}$	1	ϕ
	Q-8-2	8	$\phi + \left\{ \frac{m\pi}{4} : m = 0, \dots, 7 \right\}$	2	$\alpha^{ij} + \left\{ 0, \frac{\pi}{2} \right\}$
	Q-12-3	12	$\phi + \left\{ \frac{m\pi}{6} : m = 0, \dots, 11 \right\}$	3	$\alpha^{ij} + \left\{ \frac{\pi}{4}, \frac{\pi}{2}, \frac{3\pi}{4} \right\}$
	Q-16-4	16	$\phi + \left\{ \frac{m\pi}{8} : m = 0, \dots, 15 \right\}$	4	$\alpha^{ij} + \left\{ 0, \frac{\pi}{4}, \frac{\pi}{2}, \frac{3\pi}{4} \right\}$
DEM	Q-5-1 ⁺	5	$\phi + \left\{ \frac{2m\pi}{5} : m = 0, \dots, 4 \right\}$	1	$\phi + \pi$
	Q-9-2 ⁺	9	$\phi + \left\{ \frac{2m\pi}{9} : m = 0, \dots, 8 \right\}$	2	$\alpha^{ij} + \left\{ 0, \frac{\pi}{2} \right\}$
	Q-13-3 ⁺	13	$\phi + \left\{ \frac{2m\pi}{13} : m = 0, \dots, 12 \right\}$	3	$\alpha^{ij} + \left\{ \frac{\pi}{4}, \frac{\pi}{2}, \frac{3\pi}{4} \right\}$
	Q-17-4 ⁺	17	$\phi + \left\{ \frac{2m\pi}{17} : m = 0, \dots, 16 \right\}$	4	$\alpha^{ij} + \left\{ 0, \frac{\pi}{4}, \frac{\pi}{2}, \frac{3\pi}{4} \right\}$

the Lagrange multiplier approximations have the form (4.23), and all sets $\{\beta_k^\lambda\}_{k=1}^{n^\lambda}$ are such that condition (4.25) is avoided by all pairs of angles in these sets.

Remark 4.3.3. Although the approximation spaces of the true DEM elements contain one more enrichment function than their pure DGM counterparts, including these additional enrichment functions does not increase the cost of the true DEM elements. This is because the computational complexity of these elements (Table 2.2) is not determined by the number of enrichment functions n^E but rather the number of Lagrange multiplier approximation dofs, as the enrichment dofs are eliminated locally at the element level by static condensation (Section 2.4.3).

Example 4.3.4. As an example, the DGM element Q-8-2 described in Table 4.2 is graphically depicted in Figure 4.5.

4.3.4 Element design for $Pe > 10^3$

A difficulty arises in the implementation of the elements described in Section 4.3.3 when the Péclet number is very large (in practice, $Pe > 10^3$). Such a Péclet number can be encountered in high Reynolds number flows. In this case, it is found that even with the use of a reference point $\mathbf{x}_{r,i}^e$ inside each element Ω^e (see Section 4.4.3), the local and global matrices arising from the DGM or DEM discretizations become

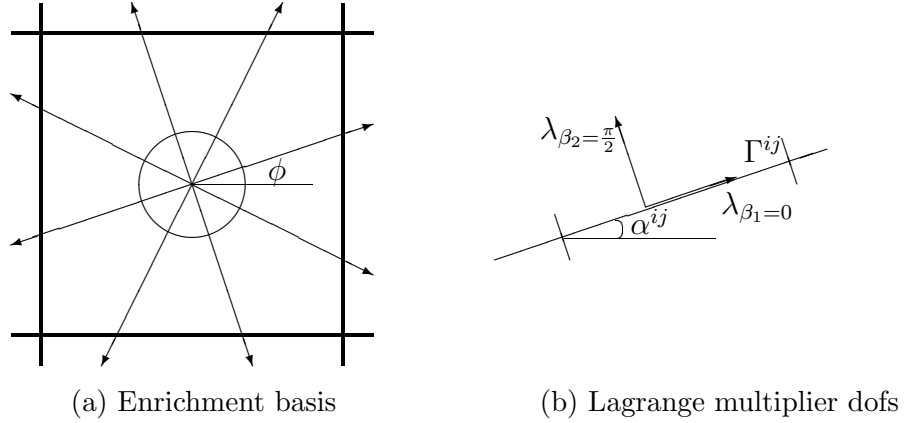


Figure 4.5: Illustration of the sets Θ^c and Θ^λ that define the Q -8-2 element

ill-conditioned. To address this issue, *advection-limited* variants of the DGM and DEM elements described so far are designed to operate in the high Péclet number regime, defined here as $Pe > 10^3$. In these variant elements, the advection coefficients appearing in the arguments of the exponential functions of the enrichment basis are limited to an experimentally-determined “safe” value of 10^3 so that the enrichment functions of these elements are made up of the functions

$$\bar{c}^E(\mathbf{x}; \theta_i)|_{\Omega^e} = \sum_{i=1}^{n^E} \exp \left\{ \frac{1}{2} \left(\frac{\mathbf{a}_\phi}{\kappa} + \bar{\mathbf{a}}_{\theta_i} \right) \cdot (\mathbf{x} - \mathbf{x}_{r,i}^e) \right\}, \quad (4.29)$$

with

$$\bar{\mathbf{a}}_{\theta_i}^T \equiv \min \left\{ 10^3, \frac{|\mathbf{a}|}{\kappa} \right\} \begin{pmatrix} \cos \theta_i & \sin \theta_i \end{pmatrix}, \quad (4.30)$$

where the bar notation is used to designate advection limitation. The resulting DGM and DEM elements are denoted by $\overline{Q-n^E-n^\lambda}$ (DGM) and $\overline{Q-n^E-n^{\lambda+}}$ (DEM).

Remark 4.3.5. For $Pe > 10^3$, functions of the form (4.29) are not free-space solutions of the homogeneous advection-diffusion equation for the original Péclet number.

Instead, they are free-space solutions of the homogeneous advection-diffusion equations for different and lower Péclet numbers. Nevertheless, these functions are more pertinent to the problem of interest than mere polynomials.

4.4 Implementation and computational properties

4.4.1 Computational complexity

The computational complexity of the DGM and DEM elements developed in Section 4.3.2 can be inferred from Table 2.2 for the case of a uniform mesh with $n^{el} = n \times n$ quadrilateral elements, assuming that static condensation of the enrichment dofs is implemented at the element-level (see Section 2.4.2). For more discussion of the computational complexity and implementation of DEM, the reader is referred to Section 2.4.3. The reader can observe that the elements in the following pairs of DGM and Galerkin elements have comparable computational complexity: $(Q-4-1, Q_1)$, $(Q-8-2, Q_2)$, $(Q-12-3, Q_3)$ and $(Q-16-4, Q_4)$. The true DEM elements are slightly more expensive: each constructed DEM element $Q-n^E-n^{\lambda+}$ has the same computational complexity as the standard Galerkin element $Q_{n^{\lambda+1}}$. In Section 4.5, it is shown numerically that any two elements of the following triplets exhibit comparable convergence rates: $(Q-4-1, Q-5-1^+, Q_1)$, $(Q-8-2, Q-9-2^+, Q_2)$, $(Q-12-3, Q-13-3^+, Q_3)$ and $(Q-16-4, Q-17-4^+, Q_4)$. For this reason, all pairs of elements within these triples are referred to here as **comparables** and the performance of a proposed DGM or DEM element is assessed (Section 4.5) by comparing it to that of its Galerkin comparable.

4.4.2 Analytical evaluation of element-level arrays

As $\kappa \rightarrow 0$ ($Pe \rightarrow \infty$), the numerical integration by a Gaussian quadrature of the integrals (2.22)–(2.25) becomes highly inaccurate because of the large magnitudes of the arguments of the exponential enrichment functions (4.1). However, these integrals can be evaluated analytically with ease on any mesh with straight-edged elements aligned with the coordinate axes. For example, on a uniform mesh of square elements $\Omega^e \equiv (x_j, x_{j+1}) \times (y_j, y_{j+1})$, the entries of the \mathbf{k}^{EE} matrices, for $1 \leq l, m \leq n^E$, take

the form

$$\begin{aligned} k_{lm}^{\text{EE}} &\equiv \int_{\Omega^e} [(\mathbf{a} \cdot \nabla c_l^E) c_m^E + \kappa \nabla c_l^E \cdot \nabla c_m^E] d\Omega^e \\ &= \left(\frac{|\mathbf{a}|}{2\kappa} (\cos \phi + \cos \theta_l) + \frac{|\mathbf{a}|}{2\kappa} (\sin \phi + \sin \theta_l) + \frac{1}{4\kappa} [(\mathbf{a}_\phi + \mathbf{a}_{\theta_l}) \cdot (\mathbf{a}_\phi + \mathbf{a}_{\theta_m})] \right) I_{lm}, \end{aligned} \quad (4.31)$$

where

$$\begin{aligned} I_{lm} &\equiv \left[\int_{x_j}^{x_{j+1}} e^{\frac{|\mathbf{a}^e|}{2\kappa} (2 \cos \phi + \cos \theta_l + \cos \theta_m)(x - x_{r,l}^e - x_{r,m}^e)} dx \right] \\ &\quad \times \left[\int_{y_j}^{y_{j+1}} e^{\frac{|\mathbf{a}^e|}{2\kappa} (2 \sin \phi + \sin \theta_l + \sin \theta)(y - y_{r,l}^e - y_{r,m}^e)} dy \right]. \end{aligned} \quad (4.32)$$

The integral (4.32) can be evaluated analytically.

Another convenient property of the functions (4.1), one that was mentioned earlier in Section 2.4.1, is that they satisfy $\mathcal{L}c^E = 0$. As a result, integration by parts of (2.22) gives

$$a(v^E, c^E) = \int_{\bar{\Omega}} (\kappa \nabla v^E \cdot \nabla c^E + \mathbf{a} \cdot \nabla c^E v^E) d\Omega = \kappa \int_{\bar{\Gamma}} \nabla c^E \cdot \mathbf{n} v^E d\Gamma. \quad (4.33)$$

Thus, for pure DGM elements and homogeneous problems, no volume integral needs be computed at all, which further simplifies the implementation of a DGM element.

4.4.3 Selection of reference points

As mentioned earlier, the enrichment functions (4.1) are scaled by the effect of an arbitrary **reference point** $\mathbf{x}_{r,i}^e$ within each element Ω^e to avoid evaluating a very large floating point number on a finite precision arithmetic processor. Numerical experiments demonstrate that overflow is inevitable if the same reference point is used for each of the enrichment functions. A procedure for setting the reference points that produces good performance for the DGM and DEM elements proposed herein is summarized in Algorithm 3.

In Algorithm 3, \mathbf{a}_ϕ and \mathbf{a}_{θ_i} are defined in (4.4), $\mathbf{a}_\phi(j)$ ($\mathbf{a}_\theta(j)$), $j = 1, 2$, is the j^{th} component of \mathbf{a}_ϕ (\mathbf{a}_θ), and $\{(x_k^e, y_k^e)\}_{k=1}^4$ are the coordinates of the nodes of element Ω^e . An analogous algorithm is used to determine the Lagrange multiplier reference points $s_{r,k}^{ij}$ which are set either to 0 or to l^{ij} depending on the sign of the argument

of the exponential in (4.17) (Figure 4.4).

Algorithm 3 Selection of exponential enrichment function reference point

```

for  $j = 1$  to  $n^{el}$  do
  for  $i = 1$  to  $n^E$  do
    if  $\mathbf{a}_\phi(1) + \mathbf{a}_{\theta_i}(1) \geq 0$  then
       $x_{r,i}^e = \max\{x_k^e\}_{k=1}^4$ 
    else
       $x_{r,i}^e = \min\{x_k^e\}_{k=1}^4$ 
    end if
    if  $\mathbf{a}_\phi(2) + \mathbf{a}_{\theta_i}(2) \geq 0$  then
       $y_{r,i}^e = \max\{y_k^e\}_{k=1}^4$ 
    else
       $y_{r,i}^e = \min\{y_k^e\}_{k=1}^4$ 
    end if
  end for
end for

```

4.5 Numerical results

In this section, the DGM and DEM advection-diffusion elements described in Section 4.3.2 are tested on four benchmark problems:

- (i) A homogeneous boundary layer problem on the unit square whose exact solution is spanned by the DGM basis (4.1) [Section 4.5.1].
- (ii) A homogeneous boundary layer problem on the unit square whose exact solution is *not* spanned by the DGM basis (4.1) [Section 4.5.2].
- (iii) A two-scale inhomogeneous BVP on the unit square [Section 4.5.3].
- (iv) A “double ramp” problem on an L -shaped domain [Section 4.5.4].

For all four problems, the diffusivity $\kappa = 1$, so that, since the length of the domain is equal to one, the global Péclet number on Ω is simply $Pe = |\mathbf{a}|$. In each case, the performance of the DGM and/or DEM elements of Section 4.3.2 is contrasted with

that of standard Galerkin elements. For the first benchmark problem (Section 4.5.1), it is also compared to that of several stabilized finite elements (Section 7.1.2 of the Appendix) developed in [16], as these elements were also tested by their developers on this problem. It is emphasized that all elements denoted by Q_n , $n = 1, 2, 3, 4$, are *non-stabilized* isoparametric Galerkin elements (Section 7.1.1 of the Appendix). All reported errors are relative errors measured in the $L^2(\Omega)$ **broken norm**. For a DGM element with n^E enrichment functions, the absolute counterpart of this **error** \mathcal{E} is computed as follows

$$\begin{aligned} \mathcal{E}^2 &= \sum_{e=1}^{n^{el}} \left\| \sum_{i=1}^{n^E} d_i c^E(\mathbf{x}; \theta_i)|_{\Omega^e} - c_{\text{ref}}(\mathbf{x})|_{\Omega^e} \right\|_{L^2(\Omega^e)}^2 \\ &= \sum_{e=1}^{n^{el}} \left\{ \int_{\Omega^e} \left(\sum_{i=1}^{n^E} d_i c^E(\mathbf{x}; \theta_i) - c_{\text{ref}}(\mathbf{x}) \right)^2 d\Omega \right\}, \end{aligned} \quad (4.34)$$

where $c_{\text{ref}}(\mathbf{x})$ is a reference (or the exact) solution, $c^E(\mathbf{x}; \theta_i)$ are the enrichment functions given by (4.1), and d_i are the computed enrichment dofs. The errors were measured either with respect to the exact solution (when available, as in the case of problems (i) – (iii)), or a reference solution computed using a sufficiently refined mesh (problem (iv)). For uniform meshes, all comparisons were performed between elements of similar computational complexity *a priori*, either for a specified level of accuracy or for a fixed total number of degrees of freedom. It turns out that all compared elements have also a similar convergence rate *a posteriori*. All unstructured meshes were generated by perturbing the nodes of an $n \times n$ uniform mesh (see e.g., Figure 4.3). On the structured meshes, all integrals (2.22)–(2.25) and therefore all matrices and right hand sides (2.56) were computed exactly (Section 4.4.2).

4.5.1 Homogeneous boundary layer problem with a flow aligned with the advection direction

Let $\Omega = (0, 1) \times (0, 1)$. Consider the BVP (2.1) with $f = 0$ and Dirichlet boundary conditions on Γ designed so that the exact solution of this problem (Figure 4.6 (c)) is

$$c_{ex}(\mathbf{x}; \phi) = \frac{e^{\mathbf{a}_\phi \cdot (\mathbf{x} - \mathbf{1})} - 1}{e^{-\mathbf{a}_\phi \cdot \mathbf{1}} - 1}, \quad (4.35)$$

where $\mathbf{1}^T \equiv (1, 1)$ and \mathbf{a}_ϕ is defined in (4.4). For a specified advection direction ϕ and Péclet number Pe , the solution of this BVP exhibits a boundary layer in the direction ϕ whose gradient is a function of Pe . The higher is Pe , the steeper is the solution.

Among all elements developed in Section 4.3.2, only the pure DGM elements Q -4-1, Q -8-2, Q -12-3 and Q -16-4 are considered for the solution of this benchmark problem, because it is a homogeneous one, per the rule of thumb described in Section 2.3. The performance results obtained for these DGM elements are compared to those of several standard Galerkin and stabilized finite elements when the size of the problem is kept fixed at approximately 400 dofs. Before commenting on these results, it is noted that:

- For this BVP, $c_{ex} \in \mathcal{V}^E$ for all DGM elements considered herein and all advection directions ϕ . However, each of these DGM elements should be expected to recover the exact solution (4.35) (to machine precision), only if $\nabla c_{ex} \cdot \mathbf{n} \in \mathcal{W}^h$ of this element.
- For a uniform discretization, α^{ij} (Figure 4.4) takes the values of $0, \frac{\pi}{2}, \pi$, or $\frac{3\pi}{2}$ for all edges $\Gamma^{ij} \in \Gamma_{\text{int}}$ of the mesh. From Table 4.2, it follows that in this case, for each considered DGM element, $\nabla c_{ex} \cdot \mathbf{n} \in \mathcal{W}^h$ for the advection directions given in Table 4.3.
- It follows that for $\phi = 0$, all four DGM elements considered herein should capture the solution of the BVP defined above to machine precision. For $\phi = \frac{\pi}{6}$, only the Q -4-1 element should do so. For $\phi = \frac{\pi}{4}$, all four DGM elements

considered herein except Q -8-2 should capture the exact solution to machine precision.

Table 4.3: Advection directions $\phi/\pi \in \{0, 1/6, 1/4\}$ for which $\nabla_{c_{ex}} \cdot \mathbf{n} \in \mathcal{W}^h$ for uniform discretizations of Ω for the homogeneous boundary layer problem of Section 4.5.1

		$\nabla_{c_{ex}} \cdot \mathbf{n} \in \mathcal{W}^h?$		
		0	$1/6$	$1/4$
DGM element	ϕ/π			
Q -4-1		✓	✓	✓
Q -8-2		✓		
Q -12-3		✓		✓
Q -16-4		✓		✓

Table 4.4 reports for $Pe = 10^2$ and $Pe = 10^3$ and three different advection directions the relative errors associated with the solutions computed on uniform meshes using the standard Galerkin element Q_1 , three different stabilized versions of this bilinear element developed in [16] under the labels STR¹, EST² and FFH³, and the lower-order DGM element Q -4-1, which has a comparable complexity. In all cases, the number of dofs is kept fixed at about 400. The reader can observe that, consistently with the remarks formulated above, the DGM element Q -4-1 reproduces the exact solution to almost machine precision for all three advection directions $\phi = 0$, $\phi = \frac{\pi}{6}$, and $\phi = \frac{\pi}{4}$. As such, it outperforms in these cases — by a large margin — the standard Galerkin element Q_1 and all of its considered stabilized counterparts.

Similarly, Table 4.5 reports the relative errors associated with the numerical solutions provided by the elements Q_1 , the STR, EST, FFH elements, and the advection-limited DGM element \overline{Q} -4-1, for the case of the very large Péclet number of 10^6 . The solutions provided by the considered stabilized finite elements are shown to be on average about four orders of magnitude more accurate for $\phi = 0$ and three orders

¹A stabilized finite element with a STReamline stabilization parameter [16].

²A stabilized finite element with an ESTimated streamline stabilization parameter [16].

³A stabilized finite element with the Franca-Frey-Hughes parameter [16, 20].

of magnitude more accurate for $\phi \neq 0$ than that generated by the standard element Q_1 . Since by construction, the basis functions of advection-limited DGM elements are not free-space solutions of the homogeneous advection-diffusion equation for the original Péclet number, the DGM element $\overline{Q-4-1}$ cannot capture the exact solution to almost machine precision. However, at least for this benchmark problem, this element is found to deliver a numerical solution that is about one order of magnitude more accurate than that delivered by any of the considered stabilized finite elements.

Table 4.4: Homogeneous boundary layer problem of Section 4.5.1 with $Pe \leq 10^3$: relative errors in the $L^2(\Omega)$ broken norm for uniform discretizations with approximately 400 dofs (non-stabilized and stabilized Galerkin Q_1 elements vs. DGM $Q-4-1$ element)

Pe	ϕ/π	Q_1	STR	EST	FFH	$\overline{Q-4-1}$
10^2	0	8.97×10^{-2}	7.62×10^{-2}	7.62×10^{-2}	8.59×10^{-2}	3.06×10^{-15}
	1/6	1.31×10^{-2}	1.14×10^{-2}	1.15×10^{-2}	1.25×10^{-2}	1.18×10^{-16}
	1/4	1.31×10^{-2}	1.14×10^{-2}	1.15×10^{-2}	1.26×10^{-2}	2.66×10^{-15}
10^3	0	5.77×10^{-1}	1.28×10^{-1}	1.28×10^{-1}	1.29×10^{-2}	3.43×10^{-14}
	1/6	2.53×10^{-2}	1.67×10^{-2}	1.67×10^{-2}	1.75×10^{-2}	1.24×10^{-15}
	1/4	2.62×10^{-2}	1.67×10^{-2}	1.67×10^{-2}	1.77×10^{-2}	3.19×10^{-14}

Table 4.5: Homogeneous boundary layer problem of Section 4.5.1 with $Pe = 10^6$: relative errors in the $L^2(\Omega)$ broken norm for uniform discretizations with approximately 400 dofs (non-stabilized and stabilized Galerkin Q_1 elements vs. advection-limited DGM $\overline{Q-4-1}$ element)

Pe	ϕ/π	Q_1	STR	EST	FFH	$\overline{Q-4-1}$
10^6	0	8.44×10^2	1.29×10^{-1}	1.29×10^{-1}	1.29×10^{-1}	2.24×10^{-2}
	1/6	9.75	1.67×10^{-2}	1.67×10^{-2}	1.75×10^{-2}	1.11×10^{-3}
	1/4	9.97	1.67×10^{-2}	1.67×10^{-2}	1.67×10^{-2}	1.29×10^{-3}

Table 4.6 reports for $Pe = 10^2$ and $Pe = 10^3$ and the same three different advection directions as before the relative errors associated with the solutions computed on uniform meshes using the standard Galerkin elements Q_2 , Q_3 and Q_4 , and the

higher-order DGM elements Q -8-2, Q -12-3 and Q -16-4. In all cases, the number of dofs is kept fixed at 400. For $\phi = 0$, the DGM element Q -8-2 performs as expected and captures the exact solution of the BVP considered herein to almost machine precision. In the other two cases, this element whose computational complexity is similar to that of the standard Galerkin element Q_2 produces numerical solutions that are one order of magnitude more accurate than those delivered by the Q_2 element when $Pe = 10^2$, and one to four orders of magnitude more accurate when $Pe = 10^3$. Similarly, the DGM element Q -12-3 captures as expected the exact solution to almost machine precision for $\phi = 0$ and $\phi = \frac{\pi}{4}$. For $\phi = \frac{\pi}{6}$, this element whose computational complexity is comparable to that of element Q_3 produces a numerical solution that is two orders of magnitude more accurate than that delivered by the element Q_3 when $Pe = 10^2$, and almost four orders of magnitude more accurate when $Pe = 10^3$. Similar conclusions can be drawn from the comparison of the performance of the DGM element Q -16-4 with the standard Galerkin element Q_4 for the solution of this BVP problem on structured meshes using 400 dofs.

On unstructured meshes, a DGM element whose enrichment field happens to include the exact solution of the problem of interest cannot be expected to capture that exact solution to machine precision at low mesh resolution because even in this case, $\nabla c_{ex} \cdot \mathbf{n} \notin \mathcal{W}^h$ in general. However, the performance results reported in Table 4.7 show that in this case, the DGM methodology outperforms the standard Galerkin methodology by a large margin. More specifically, for the solution on unstructured meshes using a fixed number of 400 dofs of the BVP considered herein with $Pe = 10^2$ and $Pe = 10^3$, the DGM element Q -8-2 is found to deliver numerical results that are one to three orders of magnitude more accurate than those delivered by the element Q_2 . The relative errors associated with the solutions produced by the Q -12-3 element are shown to be two to five orders of magnitude smaller than those associated with the numerical solutions computed with the element Q_3 , and those associated with the solutions computed using the element Q -16-4 are two to almost six orders of magnitude smaller than the relative errors associated with the numerical solutions computed with the element Q_4 . The results summarized in Tables 4.6 and 4.7 suggest also that DEM can be used with an h as well as a p mesh refinement computational

Table 4.6: Homogeneous boundary layer problem of Section 4.5.1 with $Pe \leq 10^3$: relative errors in the $L^2(\Omega)$ broken norm for uniform discretizations with approximately 400 dofs (non-stabilized Galerkin vs. DGM elements)

Pe	ϕ/π	Q_2	Q_{8-2}	Q_3	Q_{12-3}
10^2	0	5.77×10^{-2}	4.77×10^{-15}	4.06×10^{-2}	8.03×10^{-14}
	1/6	6.52×10^{-3}	2.40×10^{-4}	3.95×10^{-3}	6.61×10^{-5}
	1/4	6.51×10^{-3}	2.67×10^{-4}	3.83×10^{-3}	1.22×10^{-14}
10^3	0	4.33×10^{-1}	2.22×10^{-10}	3.68×10^{-1}	5.78×10^{-13}
	1/6	1.49×10^{-2}	8.38×10^{-4}	1.21×10^{-2}	5.50×10^{-6}
	1/4	1.53×10^{-2}	5.62×10^{-6}	1.24×10^{-2}	4.36×10^{-14}
		Pe	ϕ/π	Q_4	Q_{16-4}
10^2	0			2.39×10^{-2}	9.22×10^{-13}
	1/6			2.02×10^{-3}	1.03×10^{-5}
	1/4			1.87×10^{-3}	4.56×10^{-13}
10^3	0			2.44×10^{-1}	9.75×10^{-10}
	1/6			9.47×10^{-3}	3.31×10^{-6}
	1/4			9.81×10^{-3}	1.27×10^{-12}

strategy: not only is a more accurate solution obtained by reducing the mesh size h , but also by increasing the number of enrichment functions n^E . For the case of the very high Péclet number of 10^6 , Table 4.8 shows that all of the standard Galerkin elements Q_2 , Q_3 and Q_4 fail to deliver acceptable solutions, particularly for $\phi = 0$. On the other hand, the proposed higher-order advection-limited DGM elements deliver solutions with relative errors ranging between 10^{-4} and 10^{-2} .

Finally, Figure 4.6 compares graphically the solutions computed with the Q_{12-3} and Q_3 elements when the advection direction is set to $\phi = 0$ and the Péclet number to $Pe = 10^3$. The reader can observe that the DGM solution does not exhibit the spurious oscillations that pollute the Galerkin solution.

Table 4.7: Homogeneous boundary layer problem of Section 4.5.1 with $Pe \leq 10^3$: relative errors in the $L^2(\Omega)$ broken norm for unstructured discretizations with approximately 400 dofs (non-stabilized Galerkin vs. DGM elements)

Pe	ϕ/π	Q_2	Q_{8-2}	Q_3	Q_{12-3}
10^2	0	5.66×10^{-2}	9.11×10^{-5}	3.90×10^{-2}	1.35×10^{-5}
	1/6	6.45×10^{-3}	2.30×10^{-4}	3.90×10^{-3}	6.32×10^{-5}
	1/4	6.44×10^{-3}	1.78×10^{-4}	3.79×10^{-3}	2.47×10^{-6}
10^3	0	4.32×10^{-1}	1.69×10^{-4}	3.64×10^{-1}	2.58×10^{-6}
	1/6	1.49×10^{-2}	3.71×10^{-4}	1.21×10^{-2}	5.51×10^{-5}
	1/4	1.49×10^{-2}	9.62×10^{-5}	1.23×10^{-2}	3.21×10^{-6}
Pe	ϕ/π	Q_4	Q_{16-4}		
10^2	0	2.36×10^{-2}	2.23×10^{-6}		
	1/6	2.05×10^{-3}	1.04×10^{-5}		
	1/4	1.89×10^{-3}	2.42×10^{-8}		
10^3	0	2.43×10^{-1}	7.84×10^{-7}		
	1/6	9.48×10^{-3}	3.24×10^{-6}		
	1/4	9.83×10^{-3}	3.22×10^{-7}		

Table 4.8: Homogeneous boundary layer problem of Section 4.5.1 with $Pe = 10^6$: relative errors in the $L^2(\Omega)$ broken norm for unstructured discretizations with approximately 400 dofs (non-stabilized Galerkin vs. advection-limited DGM elements)

Pe	ϕ/π	Q_2	$\overline{Q_{8-2}}$	Q_3	$\overline{Q_{12-3}}$
10^6	0	7.07×10^2	2.23×10^{-2}	6.64×10^2	2.23×10^{-2}
	1/6	3.20	8.47×10^{-4}	5.15	7.58×10^{-4}
	1/4	5.23	7.07×10^{-4}	7.47	7.06×10^{-4}
Pe	ϕ/π	Q_4	$\overline{Q_{16-4}}$		
10^6	0	5.14×10^2	2.22×10^{-2}		
	1/6	3.45	7.57×10^{-4}		
	1/4	6.89	7.05×10^{-4}		

4.5.2 Homogeneous boundary layer problem with a flow not aligned with the advection direction

Here, attention is focused on the solution of a homogeneous boundary layer problem whose solution exhibits a boundary layer in a flow direction that is *not* aligned with

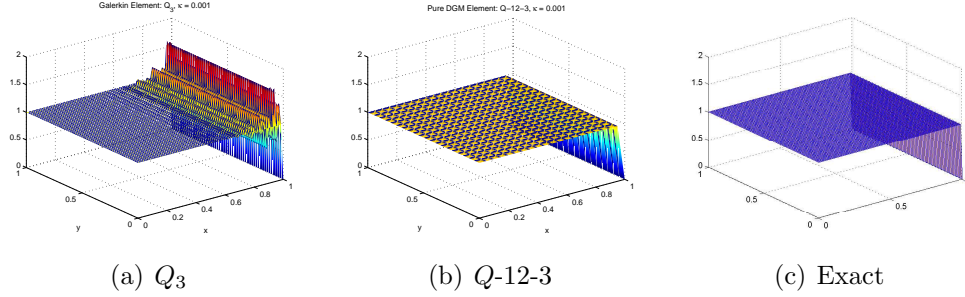


Figure 4.6: Plots of approximated and exact solutions of the homogeneous boundary layer problem of Section 4.5.1 with $\phi = 0$, 1,600 dofs and $Pe = 10^3$

the advection direction. To this effect, the BVP (2.1) is considered with Dirichlet boundary conditions designed so that the exact solution is

$$c_{ex}(\mathbf{x}; \phi, \psi) = \frac{e^{\frac{1}{2}(\mathbf{a}_\phi + \mathbf{a}_\psi) \cdot (\mathbf{x} - \mathbf{1})} - 1}{e^{-\frac{1}{2}(\mathbf{a}_\phi + \mathbf{a}_\psi) \cdot \mathbf{1}} - 1}, \quad (4.36)$$

where $\mathbf{1}^T \equiv (1, 1)$, $\phi \in [0, 2\pi)$ is the advection-direction and $\psi \in [0, 2\pi)$ is an arbitrary flow direction. The function (4.36) is plotted in Figure 4.7 (c) for $Pe = 10^3$, $\phi = \frac{\pi}{7}$ and $\psi = 0$. In general, solutions of the form given in (4.36) are *not* in the span of the enrichment space \mathcal{V}^E described in (4.1), except for certain values of ϕ and ψ . Here, the advection direction is fixed to $\phi = \pi/7$ and the direction ψ is varied by angles of $\pi/4$ so that the exact solution (4.36) is not contained in the space of approximation of any of the DGM elements considered herein. The domain is discretized by unstructured meshes. In all cases, the number of dofs is kept fixed at 1,600.

Table 4.9 reports for $Pe = 10^2$ and $Pe = 10^3$ the relative errors associated with the solutions computed on unstructured meshes using the standard Galerkin elements Q_1 , Q_2 , Q_3 and Q_4 , and the DGM elements $Q-4-1$, $Q-8-2$, $Q-12-3$ and $Q-16-4$. In all cases, the DGM elements are reported to outperform their standard Galerkin counterparts (from the computational complexity viewpoint) by a very large margin.

The performance results reported in Table 4.10 for $Pe = 10^6$ show that the advection-limited DGM elements outperform their standard Galerkin counterparts by even a larger margin of three orders of magnitude in accuracy. The convergence of the elements tested is depicted graphically in Figure 4.8. The Q_3 and Q -12-3 solutions are plotted in Figure 4.7 (a) and (b), respectively. The reader can observe that the DGM solution is oscillation free, in contrast with the Galerkin solution.

Table 4.9: Homogeneous boundary layer problem of Section 4.5.2 with $\phi = \pi/7$ and $Pe \leq 10^3$: relative errors in the $L^2(\Omega)$ broken norm for unstructured discretizations with approximately 1,600 dofs (non-stabilized Galerkin vs. DGM elements)

Pe	ψ/π	Q_1	Q -4-1	Q_2	Q -8-2
10^2	0	8.18×10^{-3}	1.18×10^{-3}	2.32×10^{-3}	5.79×10^{-5}
	1/4	5.42×10^{-3}	1.31×10^{-3}	1.40×10^{-3}	8.10×10^{-5}
	1/2	4.92×10^{-3}	3.07×10^{-3}	1.18×10^{-3}	4.18×10^{-5}
10^3	0	3.29×10^{-2}	7.65×10^{-3}	5.92×10^{-3}	1.79×10^{-3}
	1/4	3.31×10^{-2}	8.62×10^{-4}	6.06×10^{-3}	2.54×10^{-4}
	1/2	3.25×10^{-2}	9.26×10^{-4}	5.97×10^{-3}	2.12×10^{-4}
Pe	ψ/π	Q_3	Q -12-3	Q_4	Q -16-4
10^2	0	9.55×10^{-4}	4.26×10^{-6}	3.79×10^{-4}	4.94×10^{-7}
	1/4	4.93×10^{-4}	9.53×10^{-7}	1.64×10^{-4}	1.30×10^{-8}
	1/2	3.77×10^{-4}	1.01×10^{-5}	1.19×10^{-4}	2.24×10^{-8}
10^3	0	4.34×10^{-3}	1.10×10^{-4}	3.23×10^{-3}	2.30×10^{-5}
	1/4	4.46×10^{-3}	1.23×10^{-5}	3.29×10^{-3}	8.82×10^{-7}
	1/2	4.36×10^{-3}	1.11×10^{-5}	3.18×10^{-3}	1.59×10^{-6}

Table 4.11 reports for the BVP considered in this section the convergence rates measured on unstructured meshes for the standard Galerkin and DGM elements at $Pe = 10^2$. The DGM elements Q -4-1, Q -8-2, Q -12-3 and Q -16-4 deliver roughly quadratic, cubic, quartic, and quintic convergence rates, respectively. Hence from this viewpoint too, these elements are “comparable” to the standard Galerkin elements Q_1 , Q_2 , Q_3 , and Q_4 , respectively. The performance results reported in Table 4.11 also show that to achieve a relative error of 0.1% for $Pe = 10^3$, the DGM elements Q -4-1, Q -8-2, Q -12-3 and Q -16-4 require 4.4, 4.5, 14.7, and 15.1 times fewer dofs than

Table 4.10: Homogeneous boundary layer problem of Section 4.5.2 with $\phi = \pi/7$ and $Pe = 10^6$: relative errors in the $L^2(\Omega)$ broken norm for unstructured discretizations with approximately 1,600 dofs (non-stabilized Galerkin vs. advection-limited DGM elements)

Pe	ψ/π	Q_1	$\overline{Q-4-1}$	Q_2	$\overline{Q-8-2}$
10^6	0	8.67×10^{-1}	7.65×10^{-2}	2.87×10^{-1}	2.07×10^{-3}
	1/4	8.67×10^{-1}	5.67×10^{-2}	2.87×10^{-1}	7.87×10^{-4}
	1/2	8.67×10^{-1}	6.05×10^{-2}	2.87×10^{-1}	9.01×10^{-4}
Pe	ψ/π	Q_3	$\overline{Q-12-3}$	Q_4	$\overline{Q-16-4}$
10^6	0	1.85×10^{-1}	8.56×10^{-4}	9.84×10^{-2}	6.88×10^{-4}
	1/4	1.85×10^{-1}	5.68×10^{-4}	9.84×10^{-2}	4.61×10^{-4}
	1/2	1.85×10^{-1}	6.77×10^{-4}	9.84×10^{-2}	5.50×10^{-4}

the standard Galerkin elements $Q_1, Q_2, Q_3,$ and $Q_4,$ respectively. This demonstrates further the computational superiority of the DGM methodology.

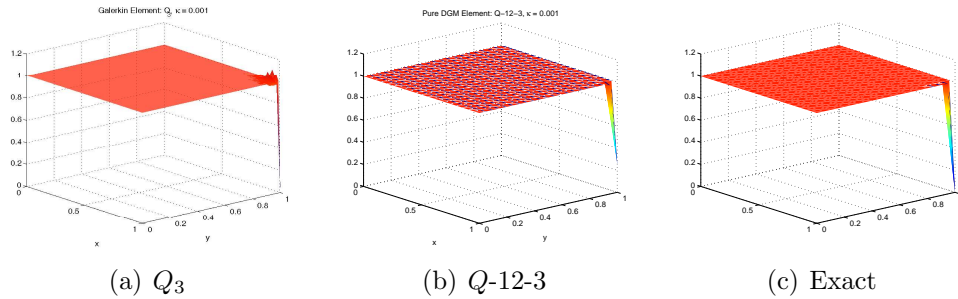


Figure 4.7: Plots of approximated and exact solutions of the homogeneous boundary layer problem of Section 4.5.2 with $\phi = \pi/7, \psi = 0, 1,600$ dofs and $Pe = 10^3$

4.5.3 Two-scale inhomogeneous problem

To highlight the role of the polynomial field c^P in DEM, a non-homogeneous variant of the boundary layer problem defined in Section 4.5.2 is considered here. More

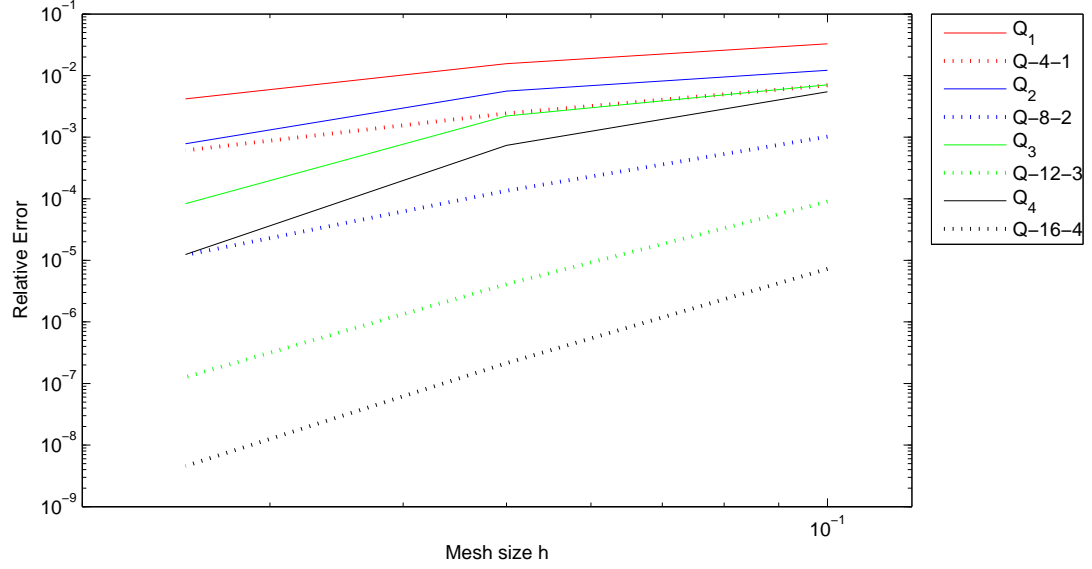


Figure 4.8: Convergence rates on unstructured meshes for the homogeneous boundary layer problem of Section 4.5.2 with $\phi = \pi/7$, $\psi = 0$ and $Pe = 10^2$

Table 4.11: Convergence rates on unstructured meshes for the homogeneous boundary layer problem of Section 4.5.2 with $\phi = \pi/7$, and $\psi = 0$

Element	Convergence rate ($Pe = 10^2$)	Required # dofs to achieve a relative error of 10^{-3} ($Pe = 10^3$)
Q_1	1.90	63,266
$Q-4-1$	1.99	14,322
Q_2	2.38	24,300
$Q-8-2$	3.27	5,400
Q_3	3.48	12,500
$Q-12-3$	3.88	850
Q_4	4.41	8,600
$Q-16-4$	5.19	570

specifically, the source term

$$f(\mathbf{x}; \phi) = \mathbf{a}_\phi \cdot \mathbf{1} + |\mathbf{a}|(y \cos \phi + x \sin \phi), \quad (4.37)$$

is added and the Dirichlet boundary conditions are designed so that the exact solution to problem (2.1) is

$$c_{ex}(\mathbf{x}; \phi) = \underbrace{\mathbf{x} \cdot \mathbf{1} + xy}_{\text{slowly varying}} + \underbrace{\left(\frac{e^{\mathbf{a}_\phi \cdot (\mathbf{x}-\mathbf{1})} - e^{-\mathbf{a}_\phi \cdot \mathbf{1}}}{e^{-\mathbf{a}_\phi \cdot \mathbf{1}} - 1} \right)}_{\text{rapidly varying}}. \quad (4.38)$$

This exact solution contains two scales: a rapidly-varying exponential *and* a slowly-varying polynomial. Because of this multi-scale behavior, a true DEM element whose approximation basis includes the enrichment as well as the polynomial fields ($c^h = c^P + c^E$) is used to solve this problem.

The performance results obtained for this problem and summarized in Tables 4.12–4.13 demonstrate once again the superior accuracy and computational efficiency of the DEM methodology, this time for the solution of inhomogeneous advection-diffusion problems.

Table 4.12: Inhomogeneous boundary layer problem of Section 4.5.3 with $Pe \leq 10^3$: relative errors in the $L^2(\Omega)$ broken norm for uniform discretizations with approximately 1,600 dofs (non-stabilized Galerkin vs. DEM elements)

Pe	ϕ/π	Q_1	Q_{5-1^+}	Q_2	Q_{9-2^+}
10^2	0	6.23×10^{-2}	4.34×10^{-5}	1.14×10^{-2}	2.52×10^{-5}
	1/4	6.23×10^{-2}	4.14×10^{-4}	9.23×10^{-4}	1.26×10^{-4}
	1/2	6.21×10^{-1}	4.34×10^{-5}	1.14×10^{-2}	2.40×10^{-5}
10^3	0	11.6×10^{-1}	2.07×10^{-4}	8.72×10^{-2}	1.39×10^{-4}
	1/4	6.76×10^{-2}	3.06×10^{-3}	4.38×10^{-3}	5.87×10^{-5}
	1/2	6.57×10^{-1}	2.07×10^{-4}	8.72×10^{-2}	1.07×10^{-4}
Pe	ϕ/π	Q_3	Q_{13-3^+}	Q_4	Q_{17-4^+}
10^2	0	6.02×10^{-3}	1.11×10^{-6}	2.36×10^{-3}	1.09×10^{-7}
	1/4	3.75×10^{-4}	1.51×10^{-5}	1.11×10^{-4}	4.50×10^{-8}
	1/2	6.02×10^{-3}	1.11×10^{-6}	2.36×10^{-3}	4.33×10^{-7}
10^3	0	6.92×10^{-2}	1.01×10^{-5}	5.22×10^{-2}	3.79×10^{-6}
	1/4	3.36×10^{-3}	1.90×10^{-5}	2.47×10^{-3}	2.00×10^{-6}
	1/2	6.92×10^{-2}	1.01×10^{-5}	5.22×10^{-2}	7.95×10^{-6}

Table 4.13: Inhomogeneous boundary layer problem of Section 4.5.3 with $Pe = 10^6$: relative errors in the $L^2(\Omega)$ broken norm for uniform discretizations with approximately 1,600 dofs (non-stabilized Galerkin vs. advection-limited DEM elements)

Pe	ϕ/π	Q_1	$\overline{Q-5-1^+}$	Q_2	$\overline{Q-9-2^+}$
10^6	0	1.26×10^2	2.16×10^{-2}	1.20	3.12×10^{-4}
	1/4	1.26×10^2	3.24×10^{-2}	1.52	4.62×10^{-5}
	1/2	1.26×10^2	2.87×10^{-2}	1.20	1.87×10^{-5}
Pe	ϕ/π	Q_3	$\overline{Q-13-3^+}$	Q_4	$\overline{Q-17-4^+}$
10^6	0	3.81×10^{-1}	8.12×10^{-5}	3.72×10^{-1}	5.12×10^{-4}
	1/4	1.49	1.05×10^{-5}	7.05×10^{-1}	1.36×10^{-6}
	1/2	3.81×10^{-1}	1.45×10^{-5}	3.72×10^{-1}	1.03×10^{-4}

Table 4.14 shows that for this two-scale problem, the DEM elements $Q-5-1^+$, $Q-9-2^+$, $Q-13-3^+$, and $Q-17-4^+$ exhibit convergence rates of approximately 2, 3, 4 and 5, respectively (Figure 4.9). Therefore, they are comparable from this viewpoint to the standard Galerkin Q_1 , Q_2 , Q_3 , and Q_4 elements except that they possess dramatically smaller error constants. For $Pe = 10^3$, the DEM element $Q-17-4^+$ delivers the same accuracy as $Q-13-3^+$ and $Q-9-2^+$ but using 2.5 and 13.8 times fewer dofs, respectively (Table 4.14). This illustrates the higher-order behavior of a DEM element with an increasing value of n^E . Also for $Pe = 10^3$, a relative error equal to 0.1% can be achieved by the DEM elements $Q-5-1^+$, $Q-9-2^+$, $Q-13-3^+$, and $Q-17-4^+$ using approximately 23.2, 4.75, 14, and 15.1 times fewer dofs than by the Galerkin Q_1 , Q_2 , Q_3 , and Q_4 elements, respectively. Perhaps more illustrative than the relative errors reported in Tables 4.12 and 4.13 are the plots of the computed solutions displayed in Figure 4.10. Whereas even the relatively high-order Q_3 solution is shown to exhibit spurious oscillations, the DEM $Q-13-3^+$ solution is shown to be virtually indistinguishable from the exact solution in the entire computational domain.

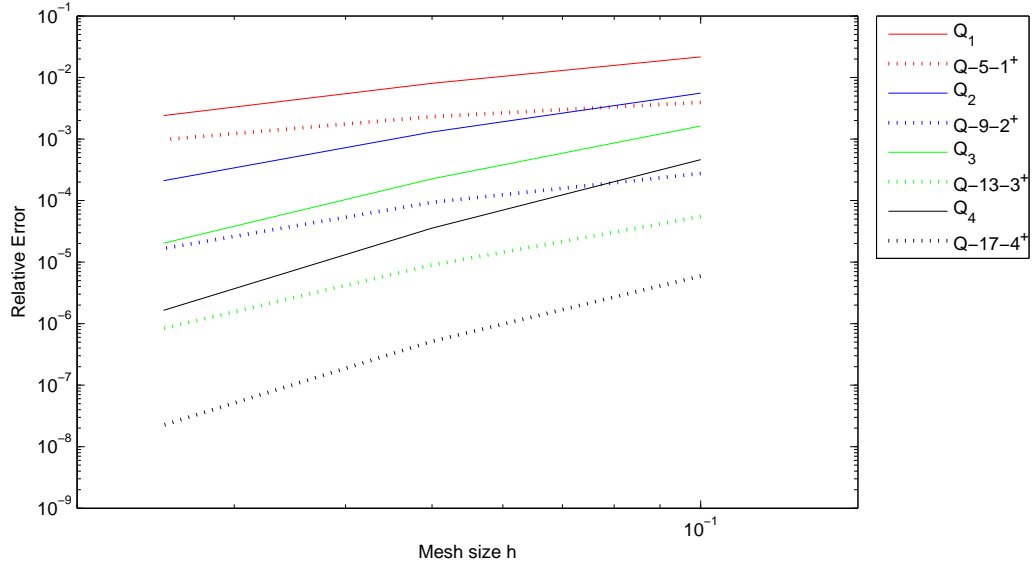


Figure 4.9: Convergence rates for the inhomogeneous boundary layer problem of Section 4.5.3 with $\phi = \pi/4$ and $Pe = 10^2$

Table 4.14: Convergence rates for the inhomogeneous boundary layer problem of Section 4.5.3 with $\phi = \pi/4$

Element	Convergence rate ($Pe = 10^2$)	Required # dofs to achieve a relative error of 10^{-3} ($Pe = 10^3$)
Q_1	1.74	203,005
$Q-5-1^+$	2.08	8,742
Q_2	2.79	14,700
$Q-9-2^+$	2.91	3,100
Q_3	3.66	8,000
$Q-13-3^+$	3.97	570
Q_4	4.65	3,400
$Q-17-4^+$	4.95	225

4.5.4 Double ramp problem on an L -shaped domain

The final benchmark problem is a variant of the double ramp problem used in [63] for testing stabilized finite elements with mesh refinement. The domain is an L -shaped

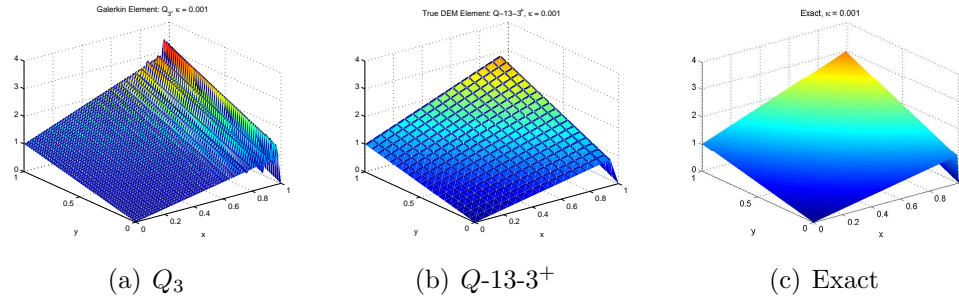


Figure 4.10: Plots of approximated and exact solutions of the inhomogeneous boundary layer problem of Section 4.5.3 with $\phi = 0$, 1,600 dofs and $Pe = 10^3$

region $\Omega = [(0, 1) \times (0, 1)] \setminus [(0, 0.5) \times (0.5, 1)]$ (Figure 4.11). The Péclet number is set to $Pe \equiv |\mathbf{a}| = 10^3$ and the source term of the BVP (2.1) is set to $f = Pe$. Homogeneous Dirichlet boundary conditions are prescribed on all six sides of Ω . The advection direction is set to $\phi = 0$ and therefore the flow moves from left to right. The solution of this problem is not available analytically; however, it is known to exhibit a strong outflow boundary layer along the line $x = 1$, two crosswind boundary layers along $y = 0$ and $y = 1$, and a crosswind internal layer along $y = 0.5$ (Figure 4.12). The nature of this solution is therefore different from that of the BVPs considered in the three previous sections. Indeed, this problem is one of the most stringent benchmark problems for advection-diffusion.

A reference solution for this problem that is free from any spurious oscillation is computed on a uniform mesh with 43,200 elements. The performance results of computations on unstructured meshes are reported in Table 4.15. They reveal that for this problem, the lower-order DGM elements provide only a moderate improvement over the Galerkin elements. The DEM elements provide a dramatic improvement of orders of magnitude in both accuracy and computational efficiency.

Figures 4.13–4.16 show four cross-sections of the nodal values of the numerical solutions computed using the DGM and DEM elements and their standard Galerkin counterparts. The Galerkin solutions exhibit noticeable oscillations in the $y = \text{const}$ plane near the outflow boundary. These are even present in the higher-order Q_4

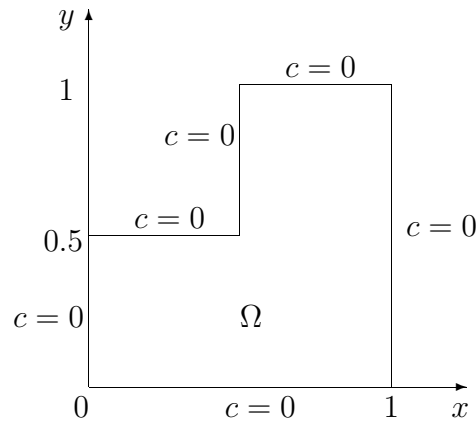


Figure 4.11: L -shaped domain for the double ramp problem of Section 4.5.4

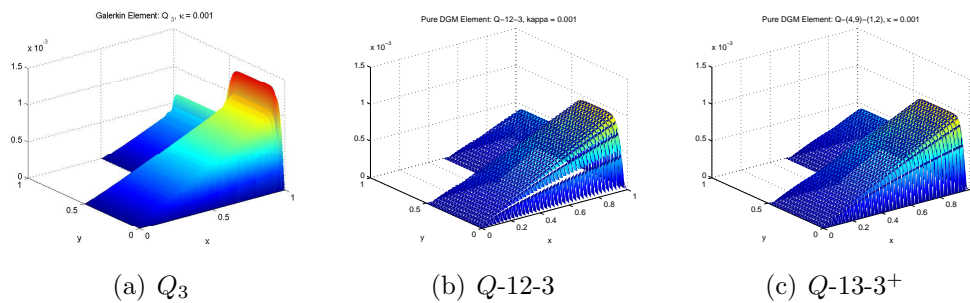


Figure 4.12: Plots of approximated solutions of the double ramp problem of Section 4.5.4 with $Pe = 10^3$ and 1,200 elements

solution. On the other hand, no oscillation is seen in the computed DGM and DEM solutions. The DGM elements appear to experience a small numerical difficulty but only along the location of the crosswind internal layer (line $y = 0.5$) (Figure 4.14 (b)). The polynomial component of the DEM elements appear to resolve this issue completely (Figure 4.14 (c)).

The computed Q_3 , $Q-12-3$ and $Q-13-3^+$ solutions are plotted on the entire domain in Figure 4.12. Again, oscillations are evident in the Galerkin solutions. On the other hand, the DGM and DEM solutions are free from any spurious oscillation. Figure

Table 4.15: Double ramp problem of Section 4.5.4: relative errors in the $L^2(\Omega)$ broken norm ($Pe = 10^3$, uniform discretizations, non-stabilized Galerkin vs. DGM and DEM elements)

Number of elements	Q_2	Q_{-8-2}	Q_{-9-2^+}
300	2.72×10^{-1}	1.19×10^{-1}	4.11×10^{-2}
1,200	1.23×10^{-1}	6.07×10^{-2}	8.47×10^{-3}
4,800	5.26×10^{-2}	2.81×10^{-2}	1.65×10^{-3}
10,800	2.92×10^{-2}	1.54×10^{-2}	7.43×10^{-4}
Number of elements	Q_3	Q_{-12-3}	Q_{-13-3^+}
300	1.49×10^{-1}	1.11×10^{-1}	2.80×10^{-2}
1,200	6.57×10^{-2}	5.00×10^{-2}	4.71×10^{-3}
4,800	2.36×10^{-2}	1.02×10^{-2}	8.24×10^{-4}
10,800	1.08×10^{-2}	4.54×10^{-3}	9.75×10^{-5}
Number of elements	Q_4	Q_{-16-4}	Q_{-17-4^+}
300	9.58×10^{-2}	8.32×10^{-2}	2.16×10^{-2}
1,200	3.78×10^{-2}	1.33×10^{-2}	2.94×10^{-3}
4,800	1.03×10^{-2}	9.17×10^{-3}	1.26×10^{-4}
10,800	3.70×10^{-3}	4.92×10^{-4}	2.12×10^{-5}

4.12 (b) suggests that the error in the DGM solutions can be partially attributed to small but noticeable discontinuities in these solutions in certain regions of the domain. The DGM solutions are nonetheless far more physically correct than the Galerkin solutions.

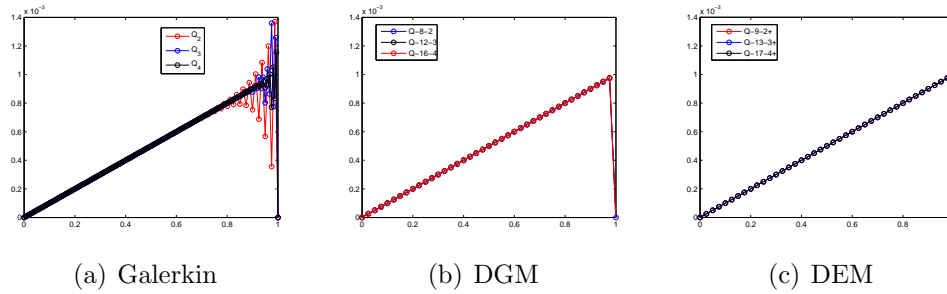


Figure 4.13: Nodal values of approximated solutions of the double ramp problem of Section 4.5.4 along the line $y = 0.25$ with 1,200 elements

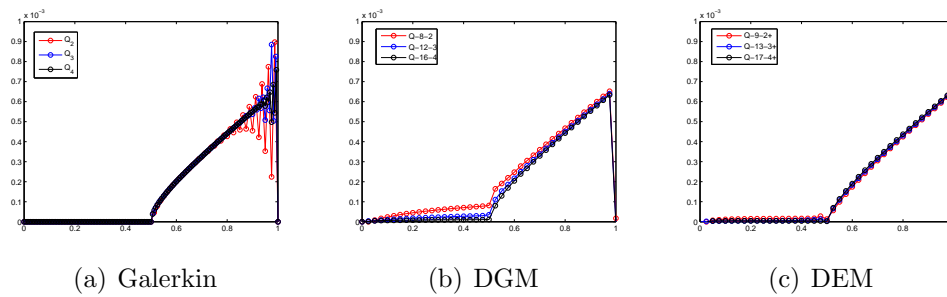


Figure 4.14: Nodal values of approximated solutions of the double ramp problem of Section 4.5.4 along the line $y = 0.5$ with 1,200 elements

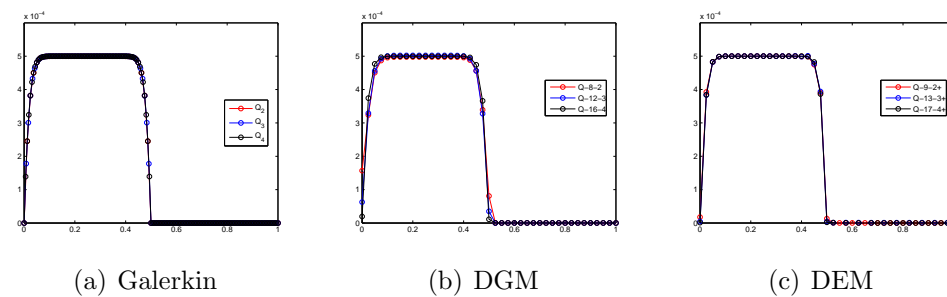


Figure 4.15: Nodal values of approximated solutions of the double ramp problem of Section 4.5.4 along the line $x = 0.5$ using 1,200 elements

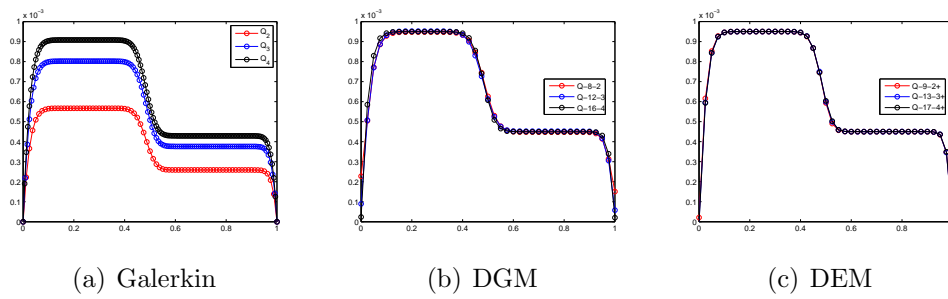


Figure 4.16: Plots of approximated solutions of the double ramp problem of Section 4.5.4 along the line $x = 0.95$ using 1,200 elements

Chapter 5

DEM for the 2D variable-coefficient advection-diffusion equation

In Chapter 4, DEM was developed and demonstrated for *constant*-coefficient advection-diffusion problems. In this chapter, attention is turned to the 2D *variable*-coefficient advection-diffusion equation – that is, (1.2) with an advection field $\mathbf{a}(\mathbf{x})$ that is allowed to vary spatially, unlike in Chapter 4. The diffusivity κ is assumed to be spatially constant, but there is no loss of generality in the formulation of the method by making this assumption (Remark 5.1.1).

5.1 The enrichment space \mathcal{V}^E

Suppose that $\mathbf{a} = \mathbf{a}(\mathbf{x})$ in Ω — that is, the advection direction varies in the spatial domain. The extension of the DEM methodology developed in Chapter 4 to variable coefficient transport problems is motivated by the observation that, even when $\mathbf{a} = \mathbf{a}(\mathbf{x})$, $\mathbf{a} \equiv \mathbf{a}^e \approx \text{constant}$ within each element $\Omega^e \subset \tilde{\Omega}$ when the mesh is refined. In other words, the variable-coefficient PDE (1.2) over Ω can be approximated by the

following set of local constant-coefficient PDEs over the elements Ω^e comprising Ω

$$\{\mathbf{a}(\mathbf{x}) \cdot \nabla c - \kappa \Delta c = f(\mathbf{x}) \text{ in } \Omega\} \approx \cup_{e=1}^{n^{el}} \{\mathbf{a}^e \cdot \nabla c - \kappa \Delta c = f(\mathbf{x}) \text{ in } \Omega^e\}. \quad (5.1)$$

Here, \mathbf{a}^e is a spatially constant value of the advection field associated with element Ω^e , e.g., if $\mathbf{a}(\mathbf{x})$ is available analytically

$$\mathbf{a}^e \equiv \mathbf{a}(\bar{\mathbf{x}}^e), \quad \bar{\mathbf{x}}^e = \text{center point of } \Omega^e, \quad (5.2)$$

(Figure 5.1). To this effect, in the variable-coefficient case, the enrichment field of DEM is chosen as

$$\mathcal{V}^E = \cup_{e=1}^{n^{el}} \{\mathcal{V}_e^E\}, \quad (5.3)$$

where

$$\mathcal{V}_e^E \subset \{c_e^E \in L^2(\mathbb{R}^2) : \mathcal{L}c_e^E = \mathbf{a}^e \cdot \nabla c_e^E - \kappa \Delta c_e^E = 0\}, \quad (5.4)$$

for elements $\Omega^e \subset \tilde{\Omega}$. By analogy with (4.1), the (exponential) free-space solutions of the local, constant-coefficient equations (5.4) are

$$c_e^E(\mathbf{x}; \theta_i^e) = \exp \left\{ \frac{1}{2\kappa} \left(\mathbf{a}_\phi^e + \mathbf{a}_{\theta_i^e}^e \right) (\mathbf{x} - \mathbf{x}_{r,i}^e) \right\} \in \mathcal{V}_e^E, \quad (5.5)$$

where ϕ^e is the advection direction local to element Ω^e defined by

$$a_1^e = |\mathbf{a}^e| \cos \phi^e, \quad a_2^e = |\mathbf{a}^e| \sin \phi^e, \quad (5.6)$$

and

$$\mathbf{a}_\phi^e \equiv |\mathbf{a}^e| \begin{pmatrix} \cos \phi^e \\ \sin \phi^e \end{pmatrix}^T, \quad \mathbf{a}_{\theta_i^e}^e \equiv |\mathbf{a}^e| \begin{pmatrix} \cos \theta_i^e \\ \sin \theta_i^e \end{pmatrix}^T. \quad (5.7)$$

Here, θ_i^e is the angle parameter defining the i^{th} enrichment function inside element Ω^e and $(x_{r,i}^e, y_{r,i}^e)$ is, as before, an arbitrary reference point for the i^{th} enrichment function inside element Ω^e . The set

$$\Theta_e^c \equiv \left\{ \text{set of angles } \{\theta_i^e \in [0, 2\pi)\}_{i=1}^{n^E} \text{ defining } \mathcal{V}_e^E \right\} \quad (5.8)$$

specifying the enrichment space inside element Ω^e is defined by analogy with (4.5). In this case however, the enrichment functions defining \mathcal{V}^E (4.1) will differ in general from one element Ω^e of the domain to another.

Remark 5.1.1. *Although the discussion above has assumed that the diffusivity κ is spatially constant, so that only $\mathbf{a}(\mathbf{x})$, the advection velocity, is allowed to vary, the approach outlined herein is not limited to the constant diffusivity case. When $\kappa = \kappa(\mathbf{x})$, the enrichment functions for the advection-diffusion equation would be defined by analogy to (5.5) but with $\kappa(\mathbf{x})$ frozen locally inside each element.*

It is worthwhile to investigate the relation between the local variable-coefficient enrichment functions comprising (5.4) and the governing variable-coefficient PDE being solved. Assume that $\mathbf{a}(\mathbf{x}) \in C^1(\Omega^e)$ so that the following Taylor expansion around the element's center point $\bar{\mathbf{x}}^e$ can be justified:

$$\mathbf{a}(\mathbf{x}) = \mathbf{a}(\bar{\mathbf{x}}^e) + \nabla \mathbf{a}|_{\mathbf{x}=\bar{\mathbf{x}}^e} \cdot (\mathbf{x} - \bar{\mathbf{x}}^e) + \mathcal{O}(\mathbf{x} - \bar{\mathbf{x}}^e)^2 \quad \text{in } \Omega^e. \quad (5.9)$$

The operator governing the PDE (1.2) inside the element Ω^e now takes the form

$$\mathcal{L}c = \mathcal{L}_e c + f(c) = 0 \quad \text{in } \Omega^e, \quad (5.10)$$

where

$$\mathcal{L}_e c \equiv \mathbf{a}(\bar{\mathbf{x}}^e) \cdot \nabla c - \kappa \Delta c, \quad (5.11)$$

and

$$f(c) \equiv [\nabla \mathbf{a}|_{\mathbf{x}=\bar{\mathbf{x}}^e} \cdot (\mathbf{x} - \bar{\mathbf{x}}^e) + \mathcal{O}(\mathbf{x} - \bar{\mathbf{x}}^e)^2] \cdot \nabla c. \quad (5.12)$$

Equation (5.10) is a perturbed constant-coefficient advection-diffusion equation. The linearization of $\mathbf{a}(\mathbf{x})$ (5.9) is essentially a first order approximation of the advection field. The free-space solutions to the constant-coefficient problems (5.11) can therefore be viewed as first order approximations of the free-space solutions of the variable-coefficient transport equation to be solved. The “residual” advection equation (5.12) acts as a source-like term. From the discussion of Section 2.3.1, more specifically, the rule of thumb regarding the inclusion of the polynomial field \mathcal{V}^P in

the approximation space of an enriched element, it follows that the true DEM discretization is more appropriate for the solution of variable-coefficient problems than its DGM counterpart, even when such problems are homogeneous. Nevertheless, it will be shown in Section 5.6 that for some variable-coefficient homogeneous problems, pure DGM elements with $\mathcal{V}^h \equiv \mathcal{V}^E = \cup_e \mathcal{V}_e^E$ defined by (5.4) can perform quite well.

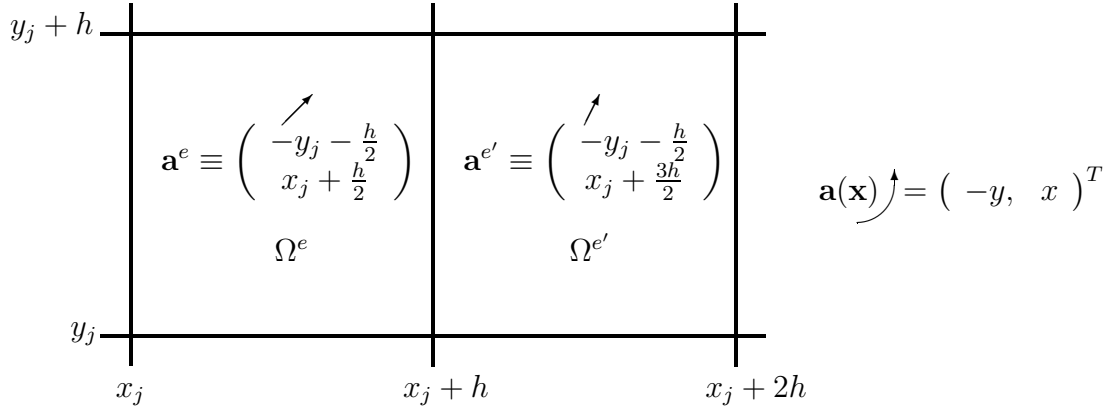


Figure 5.1: Locally frozen advection fields to enable the construction of enrichment functions as free-space solutions inside the two adjacent elements $\Omega^e = (x_j, x_j + h) \times (y_j, y_j + h)$ and $\Omega^{e'} = (x_j + h, x_j + 2h) \times (y_j, y_j + h)$ for an example advection field $\mathbf{a}(\mathbf{x}) = (-y, x)^T$

5.2 The Lagrange multiplier approximation space \mathcal{W}^h

It was shown in Section 2.3.3 that the variational formulation of the problem of interest implies that the space of approximations of the Lagrange multiplier field should be related to the normal derivatives of the enrichment functions at the element edges. The expression for the Lagrange multiplier λ in (2.52) was deduced from (2.51) for the *continuous* formulation. A problem arises when one attempts to use (2.52) to compute appropriate *discrete* Lagrange multiplier approximations λ^h in the

variable-coefficient context, however. As will be illustrated shortly, this is because the enrichment field for a generic variable-coefficient problem is element dependent.

5.2.1 Exponential Lagrange multiplier approximations

Suppose that the discrete Lagrange multiplier approximation λ^h is defined on $\Gamma^{e,e'}$ analogously to (2.52) — that is, as

$$\lambda^h|_{\Gamma^{e,e'}} = \text{span} \left\{ \nabla c_e^E(\mathbf{x}; \theta_i^e)|_{\Gamma^{e,e'}} \cdot \mathbf{n}^{e,e'} \right\}, \quad (5.13)$$

where $\text{span} \{c_e^E(\mathbf{x}; \theta_i^e)\}$ is the enrichment field (5.5) inside element Ω^e and $\mathbf{n}^{e,e'}$ denotes the outward unit normal to $\Gamma^{e,e'}$. Implicit in the expression (5.13) is the assumption that $\nabla c_e^E \cdot \mathbf{n}^{e,e'}$ is defined on $\Gamma^{e,e'}$. However, for a non-constant $\mathbf{a}(\mathbf{x})$ and the enrichment space given by (5.3) and (5.4), the normal derivative $\nabla c_e^E \cdot \mathbf{n}^{e,e'}$ is typically undefined.

For concreteness, consider a discretization of the domain Ω by a (structured or unstructured) mesh of quadrilateral elements Ω^e (Figure 2.1). Let $\Gamma^{e,e'}$ be a straight edge separating two adjacent elements Ω^e and $\Omega^{e'}$, but viewed as an edge belonging to Ω^e (Figure 4.4 with $h = l^{ij}$, $e = e_i$ and $e' = e_j$). It is straightforward to parameterize this edge with respect to an arc-length coordinate $0 \leq s \leq h$, where h is the length of this edge (see Section 4.2.1). Denoting by $\alpha^{e,e'} \in [0, \frac{\pi}{2}]$ the angle $\Gamma^{e,e'}$ makes with the x -axis, the normal derivatives of the enrichment functions in elements Ω^e and $\Omega^{e'}$ are given by

$$\nabla c_e^E(\mathbf{x}; \theta_i^e)|_{\Gamma^{e,e'}} \cdot \mathbf{n}^{e,e'} = C_1 \exp \left\{ \frac{1}{2\kappa} \left[\left(\mathbf{a}_\phi^e + \mathbf{a}_{\theta_i^e}^e \right) \cdot \mathbf{t}^{e,e'} \right] (s - s_{r,i}^{e,e'}) \right\}, \quad (5.14)$$

and

$$\nabla c_{e'}^E(\mathbf{x}; \theta_i^{e'})|_{\Gamma^{e,e'}} \cdot \mathbf{n}^{e',e} = C_2 \exp \left\{ \frac{1}{2\kappa} \left[\left(\mathbf{a}_\phi^{e'} + \mathbf{a}_{\theta_i^{e'}}^{e'} \right) \cdot \mathbf{t}^{e,e'} \right] (s - s_{r,i}^{e,e'}) \right\}, \quad (5.15)$$

respectively, where $C_1 \equiv \frac{1}{2\kappa} \left(\mathbf{a}_\phi^e + \mathbf{a}_{\theta_i^e}^e \right) \cdot \mathbf{n}^{e,e'}$ and $C_2 \equiv \frac{1}{2\kappa} \left(\mathbf{a}_\phi^{e'} + \mathbf{a}_{\theta_i^{e'}}^{e'} \right) \cdot \mathbf{n}^{e',e}$ are two constants, $\mathbf{t}^{e,e'}$ is the unit tangent vector to $\Gamma^{e,e'}$ and $0 \leq s_{r,i}^{e,e'} \leq h$ is an arbitrary reference point introduced for the stable evaluation of exponentials on $\Gamma^{e,e'}$. The

argument of the exponential in (5.14) is denoted from this point forward by

$$\Lambda^e(\theta_i^e) \equiv \Lambda_i^e \equiv \frac{1}{2\kappa} \left[\left(\mathbf{a}_\phi^e + \mathbf{a}_{\theta_i^e}^e \right) \cdot \mathbf{t}^{e,e'} \right] = \frac{|\mathbf{a}^e|}{2\kappa} \left[\cos(\phi^e - \alpha^{e,e'}) + \cos(\theta_i^e - \alpha^{e,e'}) \right]. \quad (5.16)$$

From the comparison of (5.14) and (5.15), it follows that if $\mathbf{a}^e \neq \mathbf{a}^{e'}$,

$$\nabla c_e^E(\mathbf{x}; \theta_i^e)|_{\Gamma^{e,e'}} \cdot \mathbf{n}^{e,e'} \neq -\nabla c_{e'}^E(\mathbf{x}; \theta_i^{e'})|_{\Gamma^{e',e}} \cdot \mathbf{n}^{e',e} \quad (5.17)$$

even for $\theta_i^e = \theta_i^{e'}$. This implies that, in this case, a normal derivative of an enrichment function along the edge $\Gamma^{e,e'}$ (5.13) is not well defined.

One approach for remedying the problem exhibited above is to extend the enrichment space $\mathcal{V} = \cup_e \mathcal{V}_e^E$ (5.3) to the element *edges*. This extension is denoted here by $\mathcal{V}_{e,e'}^E$ and constructed only for the sake of enabling the approximation of the Lagrange multiplier field using an approach similar to that of (5.13). For this purpose, let $\mathbf{a}^{e,e'}$ denote a constant advection velocity associated with the *edge* $\Gamma^{e,e'}$, for example,

$$\mathbf{a}^{e,e'} \equiv \mathbf{a}(\bar{\mathbf{x}}^{e,e'}), \quad \text{where } \bar{\mathbf{x}}^{e,e'} = \text{midpoint of } \Gamma^{e,e'}. \quad (5.18)$$

Then, for a specified angle $\theta_i^{e,e'} \in [0, 2\pi)$,

$$c_{e,e'}^E(\mathbf{x}; \theta_i^{e,e'}) \equiv \exp \left\{ \frac{1}{2\kappa} \left(\mathbf{a}_\phi^{e,e'} + \mathbf{a}_{\theta_i^{e,e'}}^{e,e'} \right) \left(\mathbf{x} - \mathbf{x}_{r,i}^{e,e'} \right) \right\} \Big|_{\Gamma^{e,e'}} \in \mathcal{V}_{e,e'}^E, \quad (5.19)$$

is an *i*th auxiliary enrichment function defined on the edge $\Gamma^{e,e'}$. Replacing $c_e^E(\mathbf{x}; \theta_i)|_{\Gamma^{e,e'}}$ by $c_{e,e'}^E(\mathbf{x}; \theta_i^{e,e'})$ (5.19) in (5.13) leads to the discrete Lagrange multiplier approximation

$$\lambda^h|_{\Gamma^{e,e'}} = \text{span} \left\{ \nabla c_{e,e'}^E(\mathbf{x}; \theta_i^{e,e'}) \cdot \mathbf{n}^{e,e'} \right\} = \text{span} \left\{ e^{\Lambda_i^{e,e'}(s-s_{r,i}^{e,e'})}, 0 \leq s \leq h \right\}, \quad (5.20)$$

where

$$\begin{aligned} \Lambda^{e,e'}(\theta_i^{e,e'}) \equiv \Lambda_i^{e,e'} &\equiv \frac{1}{2\kappa} \left[\left(\mathbf{a}_\phi^{e,e'} + \mathbf{a}_{\theta_i^{e,e'}}^{e,e'} \right) \cdot \mathbf{t}^{e,e'} \right] \\ &= \frac{|\mathbf{a}^{e,e'}|}{2\kappa} \left[\cos(\phi^{e,e'} - \alpha^{e,e'}) + \cos(\theta_i^{e,e'} - \alpha^{e,e'}) \right]. \end{aligned} \quad (5.21)$$

From (5.21) and (5.20), it follows that $\lambda^h|_{\Gamma^{e,e'}} = -\lambda^h|_{\Gamma^{e',e}}$ which implies that $\lambda^h|_{\Gamma^{e,e'}}$ is well defined on $\Gamma^{e,e'}$.

The approximation (5.20) can be justified by a Taylor analysis. Expanding (5.14) and the generic function defining the span in (5.20) in a Taylor series leads to

$$\nabla c_e^E(\mathbf{x}; \theta_i^e)|_{\Gamma^{e,e'}} \cdot \mathbf{n}^{e,e'} = C_1 \left[1 + \Lambda_i^e(s - s_{r,i}^{e,e'}) + \frac{1}{2}[\Lambda_i^e]^2(s - s_{r,i}^{e,e'})^2 + \mathcal{O}(s - s_{r,i}^{e,e'})^3 \right], \quad (5.22)$$

so that

$$\lambda^h(s)|_{\Gamma^{e,e'}} = 1 + \Lambda_i^{e,e'}(s - s_{r,i}^{e,e'}) + \frac{1}{2}[\Lambda_i^{e,e'}]^2(s - s_{r,i}^{e,e'})^2 + \mathcal{O}(s - s_{r,i}^{e,e'})^3, \quad (5.23)$$

respectively. Since $|s - s_{r,i}^{e,e'}| \leq h$, it follows that

$$\begin{aligned} \left| \nabla c_e^E(\mathbf{x}; \theta_i^e)|_{\Gamma^{e,e'}} \cdot \mathbf{n}^{e,e'} - C_1 \lambda^h(s)|_{\Gamma^{e,e'}} \right| &= C_1 \left| (\Lambda_i^e - \Lambda_i^{e,e'})(s - s_{r,i}^{e,e'}) \right. \\ &\quad \left. + \frac{1}{2}([\Lambda_i^e]^2 - [\Lambda_i^{e,e'}]^2)(s - s_{r,i}^{e,e'})^2 + \mathcal{O}(s - s_{r,i}^{e,e'})^3 \right| \\ &\leq C_1 \left| (\Lambda_i^e - \Lambda_i^{e,e'})h \right| + \mathcal{O}(h^2), \end{aligned} \quad (5.24)$$

which $\rightarrow 0$ when $h \rightarrow 0$. A similar result can be established for the difference

$$\left| \nabla c_{e'}^E(\mathbf{x}; \theta_i^{e'})|_{\Gamma^{e',e}} \cdot \mathbf{n}^{e',e} - C_2 \lambda^h(s)|_{\Gamma^{e',e}} \right|. \quad (5.25)$$

The implication of this analysis is that, as the mesh is refined, the normal derivatives of the enrichment functions c_e^E and $c_{e'}^E$ inside the adjacent elements Ω^e and $\Omega^{e'}$ approach the normal derivative of the auxiliary enrichment function $c_{e,e'}^E$ (5.19) which is equally defined on the edges $\Gamma^{e,e'}$ and $\Gamma^{e',e}$. This in turn justifies the choice (5.20) for approximating the Lagrange multipliers in the case of a variable advection coefficient.

5.2.2 Lagrange multiplier selection

As in the case of the constant-coefficient advection-diffusion equation (Chapter 4), the set Θ_e^c (5.8) typically leads to too many Lagrange multiplier dofs (5.13) in the sense that condition (2.49) fails. For this reason, the space of Lagrange multiplier

approximations is constructed as $\mathcal{W}^h = \cup_e \cup_{e' < e} \mathcal{W}_{e,e'}^h$ where

$$\mathcal{W}_{e,e'}^h \equiv \text{span} \left\{ \nabla c_{e,e'}^E(\mathbf{x}; \theta_i^{\lambda^{e,e'}}) |_{\Gamma^{e,e'}} \cdot \mathbf{n}^{e,e'} : \theta_i^{\lambda^{e,e'}} \in \Theta_{e,e'}^\lambda, n^\lambda \equiv \text{card}\{\Theta_{e,e'}^\lambda\} = \left\lfloor \frac{n^E}{4} \right\rfloor \right\}, \quad (5.26)$$

and n^λ is the number of Lagrange multiplier dofs per edge.

Recall that, in Section 4.2.2, in the context of a constant-coefficient advection-diffusion problem, a set of angles, denoted there by Θ^λ and used for constructing Lagrange multiplier approximations was chosen independently from the set of angles Θ^c used for selecting enrichment functions for the approximation of the primal solution. In the present chapter, this approach is modified slightly to take into account an important effect of a varying advection coefficient. Underlying this modification is the assumption that, to span as well as possible the space of all exponentials of the form $\{e^{\mathcal{A}} : \mathcal{A}_{min} \leq \mathcal{A} \leq \mathcal{A}_{max}\}$, \mathcal{A} should be uniformly distributed between \mathcal{A}_{min} and \mathcal{A}_{max} . Hence, if

$$\Lambda_{min}^{e,e'} \equiv \min_{\theta_i^{\lambda^{e,e'}} \in [0, 2\pi)} \Lambda^{e,e'}(\theta_i^{\lambda^{e,e'}}) \quad \text{and} \quad \Lambda_{max}^{e,e'} \equiv \max_{\theta_i^{\lambda^{e,e'}} \in [0, 2\pi)} \Lambda^{e,e'}(\theta_i^{\lambda^{e,e'}}), \quad (5.27)$$

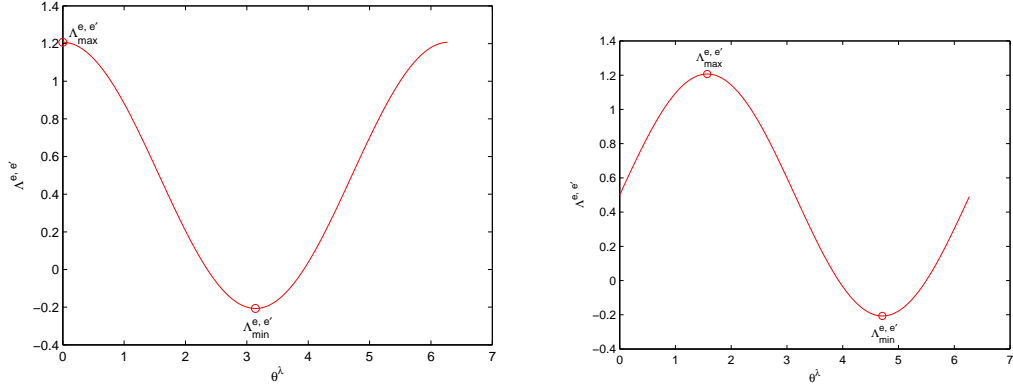
where $\Lambda^{e,e'}(\theta_i^{\lambda^{e,e'}})$ is defined as in (5.21), the angles $\theta_i^{\lambda^{e,e'}}$ are implicitly chosen here so that the corresponding values of $\Lambda^{e,e'}(\theta_i^{\lambda^{e,e'}})$ are uniformly sampled in the interval $[\Lambda_{min}^{e,e'}, \Lambda_{max}^{e,e'}]$.

The extrema of (5.21) can be computed analytically by taking the derivative of the function $\Lambda^{e,e'}(\theta)$ – which is plotted in Figure 5.2 for straight edges that are aligned with the x - and y -axes – with respect to θ , setting it to zero, and solving

$$\begin{aligned} \frac{d\Lambda^{e,e'}}{d\theta} &= \frac{|\mathbf{a}^{e,e'}|}{2\kappa} \sin(\alpha^{e,e'} - \theta^*) = 0 \\ \Rightarrow \theta^* &= \alpha^{e,e'} - n\pi, \quad n \in \mathbb{Z}. \end{aligned} \quad (5.28)$$

Substituting $\theta^* = \alpha^{e,e'} - n\pi$ into (5.21) gives

$$\Lambda_{min}^{e,e'} = \frac{1}{2\kappa} (\mathbf{a}_\phi^{e,e'} \cdot \mathbf{t}^{e,e'} - |\mathbf{a}^{e,e'}|), \quad \text{for} \quad \theta_{min}^{\lambda^{e,e'}} = \alpha^{e,e'} + \pi, \quad (5.29)$$



(a) On edges aligned with the x -axis ($\alpha = 0$) (b) On edges aligned with the y -axis
 $(\alpha = \frac{\pi}{2})$

Figure 5.2: $\Lambda^{e,e'}(\theta)$ for the case of a quadrilateral element — extrema are marked by circles ($a_1 = a_2 = \kappa = 1$)

and

$$\Lambda_{max}^{e,e'} = \frac{1}{2\kappa}(\mathbf{a}_\phi^{e,e'} \cdot \mathbf{t}^{e,e'} + |\mathbf{a}^{e,e'}|), \quad \text{for } \theta_{max}^{\lambda,e,e'} = \alpha^{e,e'}. \quad (5.30)$$

From (5.29) and (5.30), it follows that the size of the interval $[\Lambda_{min}^{e,e'}, \Lambda_{max}^{e,e'}]$ is

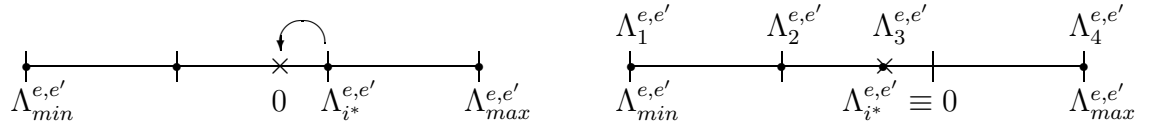
$$\Delta\Lambda^{e,e'} \equiv \Lambda_{max}^{e,e'} - \Lambda_{min}^{e,e'} = \frac{|\mathbf{a}^{e,e'}|}{\kappa}. \quad (5.31)$$

The general procedure for selecting the arguments $\Lambda_i^{e,e'} = \Lambda^{e,e'}(\theta_i^\lambda)$ defining the approximations of the Lagrange multiplier field is summarized in Algorithm 4 and illustrated in Figure 5.3. The interval $[\Lambda_{min}^{e,e'}, \Lambda_{max}^{e,e'}]$ is partitioned into $(n^\lambda - 1)$ subintervals of equal size, and the union of zero and the $(n^\lambda - 1)$ endpoints of the subintervals furthest away from zero⁵¹ are taken as the set of $\Lambda_i^{e,e'}$ that appears in the argument of the exponential in (5.20). The approach adopted here is to include the constant Lagrange multiplier approximation in $\mathcal{W}_{e,e'}^h$, generated by $\Lambda_i^{e,e'} = 0$. The constant Lagrange multiplier can be viewed as a coarse scale approximation,

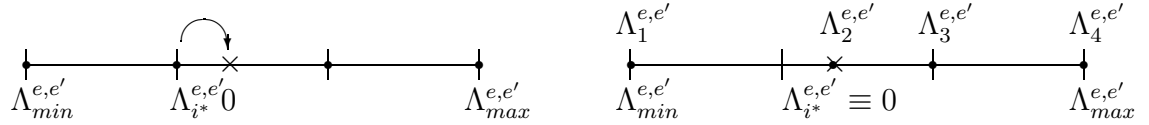
⁵¹It is straightforward to show that the function $\Lambda_i^{e,e'}$ (5.16) has necessarily a zero in the interval $(\Lambda_{min}^{e,e'}, \Lambda_{max}^{e,e'})$, or at one of its endpoints.

included in the definition of $\mathcal{W}_{e,e'}^h$ in order to balance the fine scales represented by the remaining $(n^\lambda - 1)$ exponential Lagrange multiplier approximations.

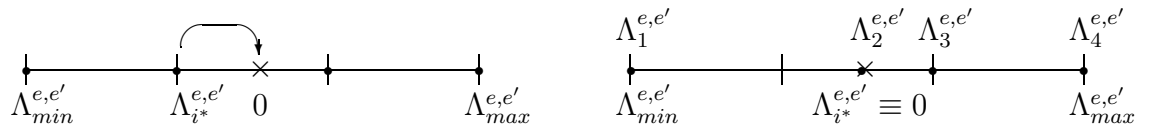
Remark 5.2.1. When $\mathbf{a}^{e,e'} \equiv \mathbf{0}$ on an edge $\Gamma^{e,e'}$ — which is the case, for example, when the advection velocity satisfies a no-slip boundary condition — and $n^\lambda > 1$, all of the Lagrange multiplier approximations (5.20) evaluate to constants. To avoid such a redundancy, polynomial Lagrange multiplier approximations are adopted instead of exponential ones on edges where $|\mathbf{a}^{e,e'}| \approx 0$.



(a) Case 1: $|\Lambda_{i^*}^{e,e'}| > \frac{1}{2}L^{e,e'}$ ($i^* = 3$)



(b) Case 2: $|\Lambda_{i^*}^{e,e'}| < \frac{1}{2}L^{e,e'}$ ($i^* = 2$)



(c) Case 3: $|\Lambda_{i^*}^{e,e'}| = \frac{1}{2}L^{e,e'}$ ($i^* = 2$)

Figure 5.3: Illustration of the Lagrange multiplier selection procedure (Algorithm 4) for $n^\lambda = 4$

Algorithm 4 Construction of the Lagrange multiplier approximation field

Given n^E exponential enrichment functions (5.5), set $n^\lambda = \left\lfloor \frac{n^E}{4} \right\rfloor$ per (2.50).

Select a tolerance $\delta > 0$, $\delta \ll 1$.

for all edges $\Gamma^{e,e'}$ in the mesh **do**

if $|\mathbf{a}^{e,e'}| < \delta$ **then**

Employ polynomial Lagrange multipliers on $\Gamma^{e,e'}$.

else

Compute $\Lambda_{min}^{e,e'}$ and $\Lambda_{max}^{e,e'}$ using (5.29) and (5.30) respectively.

Set

$$L^{e,e'} \equiv \frac{\Delta \Lambda^{e,e'}}{(n^\lambda - 1)} = \frac{|\mathbf{a}^{e,e'}|}{\kappa(n^\lambda - 1)}. \quad (5.32)$$

for $i = 1$ to n^λ **do**

Set

$$\Lambda_i^{e,e'} = \Lambda_{min}^{e,e'} + (i - 1)L^{e,e'}. \quad (5.33)$$

end for

Find the index

$$i^* = \min \left\{ \operatorname{argmin}_{1 \leq i \leq n^\lambda} |\Lambda_i^{e,e'}| \right\}. \quad (5.34)$$

Set $\Lambda_{i^*}^{e,e'} = 0$.

Return the set $\{\Lambda_i^{e,e'}\}_{i=1}^{n^\lambda}$ and define the Lagrange multipliers as in (5.20).

end if

end for

5.3 Augmentation of \mathcal{V}^E

Numerical tests (Section 5.6) suggest that the performance of DEM when applied to some variable-coefficient transport problems can be improved by adding to the space of exponential enrichment functions (5.5) some of the other free-space solutions to (1.2) derived in Chapter 3.

5.3.1 Augmentation of \mathcal{V}^E by polynomial free-space solutions to the 2D advection-diffusion equation

In Chapter 3, a family of polynomial free-space solutions to the advection-diffusion equation with constant coefficients (1.2) was derived (Section 3.1.2). Up to this

point, these polynomial free-space solutions were not included in the design of the enrichment space \mathcal{V}^E . It was found numerically (Section 4.5) that DEM performed quite well without these polynomial enrichment functions, and indeed our objective was to capture *exponential* boundary layers.

In an attempt to make \mathcal{V}_e^E as rich as possible given the information available, the following definition of \mathcal{V}_e^E (5.4) is proposed

$$\mathcal{V}_e^E \equiv \mathcal{V}_e^{\text{exp}} \oplus \mathcal{V}_e^{\text{pol}}, \quad (5.35)$$

where

$$\mathcal{V}_e^{\text{exp}} \equiv \left\{ c_e^E \in L^2(\tilde{\Omega}) : c|_{\Omega^e}^E(x, y) = \sum_{i=1}^{n^{\text{exp}}} c_i c_{e,i}^{\text{exp}}(\mathbf{x}; \theta_i^e), c_i \in \mathbb{R} \right\}, \quad (5.36)$$

$$c_{e,i}^{\text{exp}}(\mathbf{x}; \theta_i^e) = e^{\left(\frac{a_1^e + |\mathbf{a}^e| \cos \theta_i^e}{2\kappa}\right)(x - x_{r,i}^e)} e^{\left(\frac{a_2^e + |\mathbf{a}^e| \sin \theta_i^e}{2\kappa}\right)(y - y_{r,i}^e)}, \quad 0 \leq \theta_i^e < 2\pi, \quad (5.37)$$

and

$$\mathcal{V}_e^{\text{pol}} \equiv \left\{ c_e^E \in L^2(\tilde{\Omega}) : c|_{\Omega^e}^E(x, y) = \sum_{i=0}^{n^{\text{pol}}-1} c_i c_{e,i}^{\text{pol}}(\mathbf{x}), c_i \in \mathbb{R} \right\}. \quad (5.38)$$

From Section 3.1.2,

$$c_{e,0}^{\text{pol}}(\mathbf{x}) = 1, \quad (5.39)$$

$$c_{e,1}^{\text{pol}}(\mathbf{x}) = |\tilde{a}_2^e x - \tilde{a}_1^e y|, \quad (5.40)$$

$$c_{e,2}^{\text{pol}}(\mathbf{x}) = (\tilde{a}_2^e x - \tilde{a}_1^e y)^2 + 2(\tilde{\mathbf{a}}^e \cdot \mathbf{x}), \quad (5.41)$$

$$c_{e,3}^{\text{pol}}(\mathbf{x}) = (\tilde{a}_2^e x - \tilde{a}_1^e y)^3 + 6(\tilde{a}_2^e x - \tilde{a}_1^e y)(\tilde{\mathbf{a}}^e \cdot \mathbf{x}), \quad (5.42)$$

in (5.38), and so on, where it is recalled that $\tilde{\mathbf{a}}^e \equiv \mathbf{a}^e/\kappa$. Note that $\mathcal{V}_e^{\text{exp}}$ (5.36) is exactly the exponential enrichment space spanned by the functions (5.5).

Remark 5.3.1. *For constant-coefficient problems (Chapter 4), the enrichment space \mathcal{V}^E can be defined by the direct sum (5.35) as well, if desired.*

Remark 5.3.2. *To avoid possible linear dependence of the functions $c_{e,n}^{\text{pol}}(\mathbf{x})$ (5.38) with the standard Galerkin polynomial shape functions comprising \mathcal{V}^P , the rule of*

thumb of excluding \mathcal{V}^P from \mathcal{V}^h when designing elements for which \mathcal{V}_e^E is given by (5.35) will be adopted. That is, elements for which \mathcal{V}_e^E is given by (5.35) will be, by construction, pure DGM elements (second line of (2.38)) – Section 5.4.

5.3.2 Augmentation of \mathcal{V}^E by a “higher order” enrichment function

The enrichment functions comprising the space (5.35) can be viewed as first order enrichment functions for a variable-coefficient advection-diffusion BVP, in the sense that these functions solve (1.2) with $\mathbf{a}(\mathbf{x})$ linearized to first order:

$$\mathbf{a}(\mathbf{x}) \approx \mathbf{a}(\bar{\mathbf{x}}^e) \quad \text{in } \Omega^e. \quad (5.43)$$

Defining the enrichment spaces in this way may limit the performance of DEM when the method is used to solve variable-coefficient problems. To address this possible limitation, suppose $\mathbf{a}(\mathbf{x})$ is linearized to second order instead of to first order (5.43), that is:

$$\mathbf{a}(\mathbf{x}) \approx \mathbf{a}(\bar{\mathbf{x}}^e) + \nabla \mathbf{a}|_{\mathbf{x}=\bar{\mathbf{x}}^e} \cdot (\mathbf{x} - \bar{\mathbf{x}}^e) \quad \text{in } \Omega^e, \quad (5.44)$$

where $\nabla \mathbf{a}|_{\mathbf{x}=\bar{\mathbf{x}}^e}$ denotes the advection gradient tensor evaluated at the element midpoint $\bar{\mathbf{x}}^e$:

$$\nabla \mathbf{a}|_{\mathbf{x}=\bar{\mathbf{x}}^e} = \begin{pmatrix} \frac{\partial a_1}{\partial x}(\bar{\mathbf{x}}^e) & \frac{\partial a_1}{\partial y}(\bar{\mathbf{x}}^e) \\ \frac{\partial a_2}{\partial x}(\bar{\mathbf{x}}^e) & \frac{\partial a_2}{\partial y}(\bar{\mathbf{x}}^e) \end{pmatrix}. \quad (5.45)$$

With the approximation (5.44), (1.2) is of the form

$$[\mathbf{A}^e \mathbf{x} + \mathbf{b}^e] \cdot \nabla c - \Delta c = 0, \quad (5.46)$$

where

$$\mathbf{A}^e \equiv \frac{\nabla \mathbf{a}|_{\mathbf{x}=\bar{\mathbf{x}}^e}}{\kappa}, \quad \mathbf{b}^e \equiv \left(\frac{\mathbf{a}^e}{\kappa} - \frac{\nabla \mathbf{a}|_{\mathbf{x}=\bar{\mathbf{x}}^e}}{\kappa} \bar{\mathbf{x}}^e \right). \quad (5.47)$$

The free-space solutions to the variable-coefficient advection-diffusion equation (5.46) were derived in Section 3.2. Hence, the approximation space \mathcal{V}_e^E described

earlier can be augmented as follows:

$$\mathcal{V}_e^E \equiv \mathcal{V}_e^{\text{exp}} \oplus \mathcal{V}_e^{\text{pol}} \oplus \mathcal{V}_e^{\text{erf}}, \quad (5.48)$$

where

$$\mathcal{V}_e^{\text{erf}} \equiv \text{span} \left\{ \text{erf} \left(\frac{\sqrt{-2\sigma_-^e}}{2} \left(\mathbf{v}_-^e \cdot \mathbf{x} + \frac{\mathbf{v}_-^e \cdot \mathbf{b}^e}{\sigma_-^e} \right) \right) \right\}, \quad (5.49)$$

with

$$(\sigma_-^e, \mathbf{v}_-^e) \equiv \{(\sigma, \mathbf{v}) : \mathbf{A}^e \mathbf{v} = \sigma \mathbf{v}, \sigma \in \mathbb{R}, \sigma < 0\}. \quad (5.50)$$

That is, σ_-^e in (5.49) is the negative real eigenvalue, if there is such an eigenvalue, of \mathbf{A}^e (5.47) and \mathbf{v}_-^e is its corresponding eigenvector². The enrichment comprising $\mathcal{V}_e^{\text{erf}}$ (5.49) can be viewed as a “higher order” enrichment. It is “higher order” in the sense that a linear combination of this function and a constant, namely

$$\begin{aligned} c^E(\mathbf{x}) &= \int_0^{\mathbf{v}_i \cdot \mathbf{x}} \exp \left\{ \frac{\sigma_i}{2} w^2 + [\mathbf{v}_i \cdot \mathbf{b}] w \right\} dw \\ &= \frac{\sqrt{2\pi}}{2\sqrt{-\sigma_i}} \exp \left\{ \frac{-(\mathbf{v}_i \cdot \mathbf{b})^2}{2\sigma_i} \right\} \left[\text{erf} \left(\frac{\sqrt{-2\sigma_i}}{2} \left[(\mathbf{v}_i \cdot \mathbf{x}) + \frac{\mathbf{v}_i \cdot \mathbf{b}}{\sigma_i} \right] \right) + \text{erf} \left(\frac{\sqrt{2}(\mathbf{v}_i \cdot \mathbf{b})}{2\sqrt{-\sigma_i}} \right) \right], \end{aligned} \quad (5.51)$$

as shown in Section 3.2, solves

$$[\mathbf{a}^e + \nabla \mathbf{a}|_{\mathbf{x}=\bar{\mathbf{x}}^e}(\mathbf{x} - \bar{\mathbf{x}}^e)] \cdot \nabla c - \kappa \Delta c = 0. \quad (5.52)$$

Remark 5.3.1. *The following are some connections between the character of the functions (5.49) and the physics of the flow field $\mathbf{a}(\mathbf{x})$:*

- *In the case when $\mathbf{a}(\mathbf{x})$ represents the velocity field, $\nabla \mathbf{a}$ is the velocity gradient tensor.*
- *In the case of an incompressible flow ($\nabla \cdot \mathbf{a} = 0$), $\text{tr}(\mathbf{A}) = 0$, so that the eigenvalues (5.50) simplify to:*

$$\sigma_{\pm} = \pm \sqrt{\Delta}, \quad (5.53)$$

²It can be shown that if $\mathbf{a}(\mathbf{x})$ is incompressible and has real eigenvalues, one of these eigenvalues is necessarily negative; Remark 5.3.1.

which are either purely real or purely imaginary, where Δ was defined earlier in (3.52).

- In an irrotational (2D) flow, $\nabla \mathbf{a}$ is symmetric. A consequence of this fact is that all its eigenvalues are real.
- In a fluid mechanics context, when $\mathcal{I}(\nabla \mathbf{a}) \neq 0$, we are in a region known as the **vortex core** of the flow [64].

Remark 5.3.2. The higher order function (5.49) is employed only inside elements for which $\nabla \mathbf{a}|_{\mathbf{x}=\bar{\mathbf{x}}^e}$ has a negative, real eigenvalue. When $\sigma > 0$ or $\mathcal{I}(\sigma) \neq 0$ (where $\mathcal{I}(z)$ denotes the imaginary part of a complex number $z \in \mathbb{C}$), the functions specified by (5.49) are not good representations of the solutions to the sorts of boundary value problems considered here, as suggested by the LLS qualifying test described in Section 2.5.

5.4 DGM and DEM element design

5.4.1 Nomenclature and computational complexity

In this section, several low and higher-order quadrilateral DGM and DEM elements are proposed for the solution to variable-coefficient transport problems. The notation used for describing these elements is summarized in Table 5.1. As before, ‘ Q ’

Table 5.1: DGM and DEM Element Nomenclature

Element Type	\mathcal{V}^E	Notation
DGM ($\mathcal{V}^h = \mathcal{V}^E$)	\mathcal{V}^{exp}	$Q-n^{\text{exp}}-n^\lambda$
	$\mathcal{V}^{\text{pol}} \oplus \mathcal{V}^{\text{exp}}$	$Q-(n^{\text{pol}}, n^{\text{exp}})-n^\lambda$
	$\mathcal{V}^{\text{pol}} \oplus \mathcal{V}^{\text{exp}} \oplus \mathcal{V}^{\text{erf}}$	$Q-(n^{\text{pol}}, n^{\text{exp}})^*-n^\lambda$
DEM ($\mathcal{V}^h = \mathcal{V}^P \oplus \mathcal{V}^E$)	\mathcal{V}^{exp}	$Q-n^{\text{exp}}-n^{\lambda+}$
	$\mathcal{V}^{\text{exp}} \oplus \mathcal{V}^{\text{erf}}$	$Q-n^{\text{exp}*}-n^{\lambda+}$

stands for quadrilateral. The integers n^{exp} and n^{pol} denote the number of exponential enrichment functions (cardinality of the set Θ_e^c) and the number of polynomial enrichment functions ($\text{deg}(\mathcal{V}^{\text{pol}}) + 1$), respectively. The integer n^λ is the number of Lagrange multiplier dofs per edge (cardinality of the set $\{\Lambda_i^{e,e'}\}$). The + superscript designates a true DEM element ($\mathcal{V}^h = \mathcal{V}^P \oplus \mathcal{V}^E$) and distinguishes it from a pure DGM element ($\mathcal{V}^h = \mathcal{V}^E$). The polynomial approximation \mathcal{V}^P of all four considered DEM elements is chosen to be that of the standard bilinear element Q_1 . The * superscript indicates that the enrichment space of the element has been augmented by the “higher order” error function enrichment (5.49). For the $Q-(n^{\text{pol}}, n^{\text{exp}})^*-n^\lambda$ elements, $n^E = n^{\text{exp}} + n^{\text{pol}} + 1$. Otherwise, for the $Q-(n^{\text{pol}}, n^{\text{exp}})-n^\lambda$ and $Q-(n^{\text{pol}}, n^{\text{exp}})-n^{\lambda+}$ elements, $n^E = n^{\text{exp}} + n^{\text{pol}}$; for the $Q-n^{\text{exp}}-n^\lambda$ and $Q-n^{\text{exp}}-n^{\lambda+}$ elements, $n^E = n^{\text{exp}}$.

In this section, proposed first are four DGM elements $Q-4-1$, $Q-8-2$, $Q-12-3$ and $Q-16-4$ and four DEM elements $Q-5-1^+$, $Q-9-2^+$, $Q-13-3^+$ and $Q-17-4^+$ for which $\mathcal{V}^E = \mathcal{V}^{\text{exp}}$. For all of these elements, Θ_e^c is chosen as

$$\Theta_e^c = \{\theta_m^e\}_{m=1}^{n^E} \equiv \phi^e + \{\beta_m\}_{m=1}^{n^E} \quad \text{with} \quad \beta_m = \frac{2(m-1)\pi}{n^E} \in [0, 2\pi), \quad (5.54)$$

where $n^E = n^{\text{exp}}$. (5.54) leads to the specifications of Table 5.2.

Proposed also are four additional DGM elements $Q-(4, 0)-1$, $Q-(4, 5)-2$, $Q-(4, 9)-3$ and $Q-(4, 13)-4$ for which $\mathcal{V}^E = \mathcal{V}^{\text{pol}} \oplus \mathcal{V}^{\text{exp}}$. The specifications of these elements are summarized in Table 5.2 as well. For each of these elements $n^{\text{pol}} = 4$, so that \mathcal{V}^{pol} consists of polynomial free-space solutions to the constant-coefficient advection-diffusion equation up to degree three (5.39)–(5.42). For the first element, denoted by $Q-(4, 0)-1$, $n^{\text{exp}} = 0$, so that $\mathcal{V}^E = \mathcal{V}^{\text{pol}}$.

The computational complexities and stencil widths of the DGM and DEM elements just described can be inferred from Table 2.2 for the case of a uniform mesh with $n^{el} = n \times n$ quadrilateral elements, assuming that static condensation of the enrichment dofs is implemented at the element-level (see Section 2.4.2). Some of the elements’ key computational properties are summarized below.

- The stencil of a DGM discretization is in general smaller than that of its Galerkin comparable.

Table 5.2: Enrichment spaces of the proposed DGM and DEM elements for variable-coefficient transport problems

	Element	n^E	Θ_e^c	$\deg\{\mathcal{V}^{\text{pol}}\}$
DGM element	Q -4-1	4	$\phi^e + \left\{ \frac{\pi}{2}(m-1) : m = 1, \dots, 4 \right\}$	—
	Q -(4, 0)-1	4	—	3
	Q -(4, 0)*-1	5	—	3
	Q -8-2	8	$\phi^e + \left\{ \frac{\pi}{4}(m-1) : m = 1, \dots, 8 \right\}$	—
	Q -(4, 5)-2	9	$\phi^e + \left\{ \frac{2\pi}{5}(m-1) : m = 1, \dots, 5 \right\}$	3
	Q -(4, 5)*-2	10	$\phi^e + \left\{ \frac{2\pi}{5}(m-1) : m = 1, \dots, 5 \right\}$	3
	Q -12-3	12	$\phi^e + \left\{ \frac{\pi}{6}(m-1) : m = 1, \dots, 12 \right\}$	—
	Q -(4, 9)-3	13	$\phi^e + \left\{ \frac{2\pi}{9}(m-1) : m = 1, \dots, 9 \right\}$	3
	Q -(4, 9)*-3	14	$\phi^e + \left\{ \frac{2\pi}{9}(m-1) : m = 1, \dots, 9 \right\}$	3
	Q -16-4	16	$\phi^e + \left\{ \frac{\pi}{8}(m-1) : m = 1, \dots, 16 \right\}$	—
	Q -(4, 13)-4	17	$\phi^e + \left\{ \frac{2\pi}{13}(m-1) : m = 1, \dots, 13 \right\}$	3
	Q -(4, 13)*-4	18	$\phi^e + \left\{ \frac{2\pi}{13}(m-1) : m = 1, \dots, 13 \right\}$	3
DEM element	Q -5-1 ⁺	5	$\phi^e + \left\{ \frac{2\pi}{5}(m-1) : m = 1, \dots, 5 \right\}$	—
	Q -9-2 ⁺	9	$\phi^e + \left\{ \frac{2\pi}{9}(m-1) : m = 1, \dots, 9 \right\}$	—
	Q -13-3 ⁺	13	$\phi^e + \left\{ \frac{2\pi}{13}(m-1) : m = 1, \dots, 13 \right\}$	—
	Q -17-4 ⁺	17	$\phi^e + \left\{ \frac{2\pi}{17}(m-1) : m = 1, \dots, 17 \right\}$	—

- Any two elements of the following quadruples of DGM and Galerkin elements have comparable computational complexity: (Q -4-1, Q -(4, 0)-1, Q -(4, 0)*-1, Q_1), (Q -8-2, Q -(4, 5)-2, Q -(4, 5)*-2, Q_2), (Q -12-3, Q -(4, 9)-3, Q -(4, 9)*-3, Q_3) and (Q -16-4, Q -(4, 13)-4, Q -(4, 13)*-4, Q_4).

- Each constructed DEM element $Q-n^E-n^{\lambda+}$ and $Q-n^{E*}-n^{\lambda+}$ has the same computational complexity as the standard Galerkin element $Q_{n^{\lambda+1}}$.

5.4.2 Lagrange multiplier selection

For all DGM and DEM elements summarized in Table 5.2, the Lagrange multiplier approximations are constructed via the Lagrange multiplier approximation procedure developed in Section 5.2. The sets of exponential arguments $\Lambda_i^{e,e'}$ associated with these elements are specified in Table 5.3.

Table 5.3: Lagrange multiplier approximation spaces of the DGM and DEM elements in Table 5.2 (identified here by the number of Lagrange multiplier dofs per edge, n^λ)

n^λ	$\{\Lambda_i^{e,e'}\} \subseteq$	$\Theta_{e,e'}^\lambda \subseteq$	$\lambda_h^{e,e'} \subseteq$
1	$\{0\}$	$\{\phi^{e,e'} + \pi\}$	$\{1\}$
2	$\{0, \Lambda_{min}^{e,e'}, \Lambda_{max}^{e,e'}\}$	$\{\phi^{e,e'} + \pi, \alpha^{e,e'} + \pi, \alpha^{e,e'}\}$	$\left\{1, \exp\left(\frac{1}{2\kappa} \mathbf{a}_\phi^{e,e'} \cdot \mathbf{t}^{e,e'} \mp \frac{1}{2\kappa} \mathbf{a}^{e,e'} \right)\right\}$
3	$\left\{0, \Lambda_{mp}^{e,e'}, \Lambda_{min}^{e,e'}, \Lambda_{max}^{e,e'}\right\}$	$\left\{\phi^{e,e'} + \pi, \alpha^{e,e'} + \frac{\pi}{2}, \alpha^{e,e'} + \pi, \alpha^{e,e'}\right\}$	$\left\{1, \exp\left(\frac{1}{2\kappa} \mathbf{a}_\phi^{e,e'} \cdot \mathbf{t}^{e,e'}\right), \exp\left(\frac{1}{2\kappa} \mathbf{a}_\phi^{e,e'} \cdot \mathbf{t}^{e,e'} \mp \frac{1}{2\kappa} \mathbf{a}^{e,e'} \right)\right\}$
4	$\left\{0, \Lambda_{min}^{e,e'}, \Lambda_{max}^{e,e'}, \Lambda_{mp}^{e,e'} \pm \frac{1}{6} \Delta \Lambda^{e,e'}\right\}$	$\left\{\phi^{e,e'} + \pi, \alpha^{e,e'} + \pi, \alpha^{e,e'}, \alpha^{e,e'} + \cos^{-1}\left(\mp \frac{1}{3}\right)\right\}$	$\left\{1, \exp\left(\frac{1}{2\kappa} \mathbf{a}_\phi^{e,e'} \cdot \mathbf{t}^{e,e'} \mp \frac{1}{2\kappa} \mathbf{a}^{e,e'} \right), \exp\left(\frac{1}{2\kappa} \mathbf{a}_\phi^{e,e'} \cdot \mathbf{t}^{e,e'} \mp \frac{1}{6\kappa} \mathbf{a}^{e,e'} \right)\right\}$

The following analysis suggests that the Lagrange multiplier selection procedure detailed in Section 5.2.2 is appropriate for the $Q-(n^{\text{pol}}, n^{\text{exp}})-n^\lambda$ elements in Table 5.2.

From Section 3.1.2, an n^{th} degree polynomial free-space solution $c_n^{\text{pol}}(\mathbf{x})$ to (1.2) has the form

$$c_n^{\text{pol}}(\mathbf{x}) = |\tilde{\mathbf{a}} \times \mathbf{x}|^n + f_n(x, y), \quad (5.55)$$

where $f_n(x, y)$ is an $n - 1$ degree polynomial. Now, on an edge Γ^{ij} (4.13),

$$|\tilde{\mathbf{a}} \times \mathbf{x}|^n|_{\Gamma^{ij}} = |(\tilde{\mathbf{a}} \times \mathbf{x}_0^{ij}) + (\tilde{\mathbf{a}} \times \mathbf{t}^{ij})s|^n. \quad (5.56)$$

Taking the normal derivative of the expression in (5.56) along an edge Γ^{ij} , it follows that the polynomial enrichment functions (5.55) give rise to Lagrange multiplier approximations of the form

$$\lambda^h(s)|_{\Gamma^{ij}} = \sum_{k=0}^{n^{\text{pol}}-2} \lambda_k s^k, \quad 0 \leq s \leq l^{ij}. \quad (5.57)$$

That is, if \mathcal{V}^{pol} consists of polynomials up to degree $n^{\text{pol}} - 1$, then the Lagrange multiplier approximations should be polynomials up to degree $n^{\text{pol}} - 2$. By the rule of thumb (2.50) (Remark 2.3.2), only $\lfloor n^{\text{pol}}/4 \rfloor$ Lagrange multiplier approximations per edge are to be retained. Now, observe that, for $k \gg 1$ and $h \rightarrow 0$, $s^k \rightarrow 0$. Hence, it is reasonable to approximate the Lagrange multiplier approximations (5.57) by

$$\lambda^h(s)|_{\Gamma^{ij}} = \sum_{k=0}^{n_{\text{pol}}^\lambda} \lambda_k s^k, \quad 0 \leq s \leq l^{ij}, \quad (5.58)$$

where

$$n_{\text{pol}}^\lambda = \left\lfloor \frac{n^{\text{pol}}}{4} \right\rfloor. \quad (5.59)$$

For the elements in Table 5.2, $n^{\text{pol}} = 4$ so that (5.59) evaluates to $n_{\text{pol}}^\lambda = 1$. For $n_{\text{pol}}^\lambda = 1$, (5.58) is simply the constant approximation. But the constant $\lambda^h = 1$ approximation is, by construction, already contained in the space \mathcal{W}_{ij}^h (Section 5.2). This suggests that the Lagrange multiplier selection algorithm developed in Section 5.2 need not be modified for the elements Q -(4,0)-1, Q -(4,5)-2, Q -(4,9)-3 and Q -(4,13)-4.

5.5 Implementation and computational properties

5.5.1 Analytical evaluation of element-level arrays

As in the constant-coefficient DEM, when $\kappa \rightarrow 0$ ($Pe \rightarrow \infty$), the numerical integration by a Gaussian quadrature of the integrals (2.22)–(2.25) becomes highly inaccurate because of the large magnitudes of the arguments of the exponential enrichment

functions (5.36). It was shown in Section 4.4.2 that these integrals can be computed analytically on a mesh with straight-edged elements whose edges are aligned with the coordinate axes if \mathbf{a} is spatially constant. In general, these integrals can still be evaluated analytically on any mesh with straight-edged elements aligned with the coordinate axes, provided that the advection field $\mathbf{a}(\mathbf{x})$ is a sufficiently simple function. For example, on a uniform mesh of square elements $\Omega^e \equiv (x_j, x_{j+1}) \times (y_j, y_{j+1})$, the entries of the \mathbf{k}^{EE} matrices (2.56), for $1 \leq l, m \leq n^E$, take the form

$$\begin{aligned} k_{lm}^{\text{EE}} &\equiv \int_{\Omega^e} [(\mathbf{a}(\mathbf{x}) \cdot \nabla c_l) c_m + \kappa \nabla c_l \cdot \nabla c_m] d\Omega^e \\ &= \frac{|\mathbf{a}^e|}{2\kappa} (\cos \phi^e + \cos \theta_l^e) I_{lm}^{a_1(\mathbf{x})} + \frac{|\mathbf{a}^e|}{2\kappa} (\sin \phi^e + \sin \theta_l^e) I_{lm}^{a_2(\mathbf{x})} \\ &\quad + \frac{1}{4\kappa} [(\mathbf{a}_\phi + \mathbf{a}_{\theta_l}) \cdot (\mathbf{a}_\phi + \mathbf{a}_{\theta_m})] I_{lm}^{\text{diff}}, \end{aligned} \quad (5.60)$$

where

$$I_{lm}^{a_i(\mathbf{x})} \equiv \int_{x_j}^{x_{j+1}} \int_{y_j}^{y_{j+1}} a_i(\mathbf{x}) e^{\frac{|\mathbf{a}^e|}{2\kappa} (2 \cos \phi^e + \cos \theta_l^e + \cos \theta_m^e)(x - x_{r,l}^e - x_{r,m}^e)} \times e^{\frac{|\mathbf{a}^e|}{2\kappa} (2 \sin \phi^e + \sin \theta_l^e + \sin \theta_m^e)(y - y_{r,l}^e - y_{r,m}^e)} dy dx, \quad (5.61)$$

for $i = 1, 2$, and

$$I_{lm}^{\text{diff}} \equiv \left[\int_{x_j}^{x_{j+1}} e^{\frac{|\mathbf{a}^e|}{2\kappa} (2 \cos \phi^e + \cos \theta_l^e + \cos \theta_m^e)(x - x_{r,l}^e - x_{r,m}^e)} dx \right] \times \left[\int_{y_j}^{y_{j+1}} e^{\frac{|\mathbf{a}^e|}{2\kappa} (2 \sin \phi^e + \sin \theta_l^e + \sin \theta_m^e)(y - y_{r,l}^e - y_{r,m}^e)} dy \right]. \quad (5.62)$$

The diffusion integral I_{lm}^{diff} (5.62) can be evaluated analytically as it is simply the product of two one-dimensional integrals of exponential functions. Analytic computation of the advection integrals $I_{lm}^{a_i(\mathbf{x})}$ (5.61) depends on the form of $\mathbf{a}(\mathbf{x})$. For a polynomial $a_i(\mathbf{x})$, e.g., $a_i(\mathbf{x}) = x^{m_i} y^{n_i}$ for some integers m_i and n_i , a recursive relation can be derived to compute (5.61) exactly with ease.

In practice, $\mathbf{a}(\mathbf{x})$ is likely to be available numerically — that is, at a discrete set of N points $\{\mathbf{x}_1^e, \dots, \mathbf{x}_N^e\} \in \overline{\Omega^e}$. In this case, $\mathbf{a}(\mathbf{x})$ can be reconstructed by interpolating its discrete values at these points using standard Lagrange polynomial interpolation within each element (Section 5.5.3), making possible the analytic computation of

(5.61).

5.5.2 Scaling of enrichment functions

To avoid evaluating a very large floating point number on a finite precision arithmetic machine, the exponential enrichment functions (5.36) are scaled by the effect of an arbitrary reference point $\mathbf{x}_{r,i}^e$ within each element Ω^e per the procedure outlined in Section 4.4.3 (Algorithm 3). The polynomial enrichment functions (5.38) are scaled as well to prevent numerical overflow and improve matrix conditioning. They are normalized as follows:

$$c_{e,n}^{\text{pol}}(\mathbf{x}) = \frac{c_{e,n}^{\text{pol}}(\mathbf{x})}{\max_{\mathbf{x} \in \Omega^e} |c_{e,n}^{\text{pol}}(\mathbf{x})|}, \quad (5.63)$$

within each element Ω^e .

5.5.3 Interpolation of advection field

In practical applications, the advection field $\mathbf{a}(\mathbf{x})$ may not be available in closed analytic form. Suppose the advection field $\mathbf{a}(\mathbf{x})$ is available at a discrete set of N points, $\mathbf{x}_1, \dots, \mathbf{x}_N$: $\{\mathbf{a}_i : i = 1, \dots, N\}$, where $\mathbf{a}_i \equiv \mathbf{a}(\mathbf{x}_i)$. In this case (Sections 5.6.3–5.6.4), the $\mathbf{a}(\mathbf{x})$ that appears in the bilinear form (2.22) will be interpolated from these discrete values using some appropriate set of interpolation functions. For example, if the interpolation functions are isoparametric shape functions based on Lagrange polynomials, $\mathbf{a}(\mathbf{x})$ is interpolated inside element Ω^e as

$$\mathbf{a}^e(\boldsymbol{\xi}) = \sum_{i=1}^{\# \text{ nodes of } \Omega^e} \mathbf{a}_i^e \phi_i^e(\boldsymbol{\xi}), \quad (5.64)$$

where $\boldsymbol{\xi} \in [-1, 1]^2$ is the usual parent coordinate system (Section 7.1.1), $\phi_i^e(\boldsymbol{\xi})$ are the interpolation functions and \mathbf{a}_i^e are the values of the advection field at the nodes of an element Ω^e .

5.6 Numerical results

The performances of the DGM and DEM elements described in the previous section are assessed on four different two-dimensional linear variable-coefficient transport problems. In each of these problems, the boundary conditions for (1.2) are prescribed so that boundary layers form as $\kappa \rightarrow 0$ ($Pe \rightarrow \infty$), making the solution of these problems by a standard FEM inefficient. The first two problems are:

- An inhomogeneous BVP with a rotating advection field posed on an L -shaped domain [Section 5.6.1].
- A homogeneous BVP with a linear advection field, referred to as the “thermal boundary value problem” [Section 5.6.2].

In these problems, $\mathbf{a}(\mathbf{x})$ is given in closed analytical form. It is shown that DEM can outperform the standard and stabilized Galerkin FEM by a large margin without augmenting the exponential enrichment space (5.36) with additional enrichment functions, as proposed in Section 5.3.

The last two problems considered in this section are:

- A homogeneous BVP modeling a lid-driven cavity flow [Section 5.6.3].
- A homogeneous BVP posed inside a differentially-heated square cavity [Section 5.6.4].

The advection field $\mathbf{a}(\mathbf{x})$ for these problems is obtained by solving an initial boundary value problem (IBVP) for the time-dependent, incompressible (or near-incompressible) 2D Navier-Stokes equations, and converging this solution to a steady state. Since $\mathbf{a}(\mathbf{x})$ is computed numerically, it is available at a discrete set of points in the domain, rather than in closed analytical form as in the case of the former two problems. The $\mathbf{a}(\mathbf{x})$ that appears in the bilinear form defining the stiffness matrices is interpolated inside each element from these discrete points using Lagrange polynomial interpolation functions, following the procedure outlined in Section 5.5.3. For the latter two test

cases, it is shown that the accuracy of the DEM solution can be improved by augmenting the exponential enrichment space $\mathcal{V}_e^{\text{exp}}$ by additional free-space solutions to variants of the governing equation, as described in Section 5.3.

In all problems, the given domain Ω is discretized by uniform meshes of square elements. For the problems of Sections 5.6.1 and 5.6.2, the performances of the considered DGM and DEM elements are contrasted with those of their standard Galerkin comparables. The performances of the DGM elements Q -4-1 and Q -(4,0)-1 and DEM elements Q -5-1⁺ are also compared to that of the streamline upwind stabilized bilinear finite element proposed in [16]. All reported solution errors are relative solution errors measured in the $L^2(\Omega)$ broken norm (4.34), where $c_{\text{ref}}(\mathbf{x})$ is a converged “reference” solution computed using a sufficiently refined mesh. The adoption here of a reference solution in lieu of an exact one is due to the fact that the exact solutions of the BVPs considered in the subsequent subsections are unavailable. It is verified that the reference solutions employed in the error analysis are free from any spurious oscillations.

5.6.1 Inhomogeneous problem with a rotating advection field and an L -shaped domain

Here, the following inhomogeneous BVP defined on an L -shaped domain $\Omega = [(0, 1) \times (0, 1)] \setminus [(0, 0.5) \times (0.5, 1)]$ (Figure 5.4) is considered

$$\begin{aligned} \begin{pmatrix} 1 - y, & x \end{pmatrix}^T \cdot \nabla c(\mathbf{x}) - \kappa \Delta c(\mathbf{x}) &= 1, & \text{in } \Omega = [(0, 1) \times (0, 1)] \setminus [(0, 0.5) \times (0.5, 1)], \\ c &= 0, & \text{on } \partial\Omega. \end{aligned} \tag{5.65}$$

The diffusivity constant is set to $\kappa = 10^{-3}$, so that the Péclet number for this problem is $Pe = 10^3$. This problem is a variable-coefficient variant of an advection-diffusion problem that was studied in [63] and Section 4.5.4. It is also similar to a benchmark problem that was used to evaluate the performances of the residual-free bubbles and Petrov-Galerkin stabilized methods in [14] and [23], respectively. The advection field represents a rigid body rotation about the point $(x, y) = (0, 1)$.

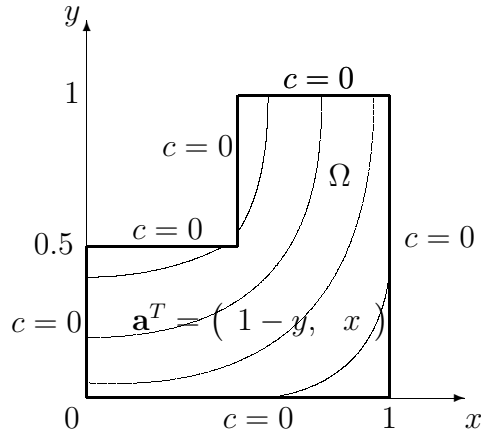


Figure 5.4: L -shaped domain and rotating velocity field, with curved lines indicating streamlines (Section 5.6.1)

The above problem is a stringent test for the advection-diffusion equation because its solution presents an outflow boundary layer as well as a second boundary layer which terminates in the vicinity of the reentrant corner (the point $(x, y) = (0.5, 0.5)$ in Figure 5.4). Because it is an inhomogeneous problem, the DEM elements Q -5-1⁺, Q -9-2⁺, Q -13-3⁺ and Q -17-4⁺ are more suitable for its discretization than their DGM counterparts. The performances of these elements obtained for this problem are reported in Table 5.4 for four different mesh resolutions. In each case, these performances are contrasted with those of the standard Galerkin elements Q_1 , Q_2 , Q_3 and Q_4 , and that of the stabilized version of the finite element Q_1 . The results are tabulated by groups of elements of comparable convergence rates. The reference solution employed in the error analysis is computed using the higher-order Galerkin element Q_6 and a uniform mesh with an element size $h = 1/120$.

The reader can observe that in general, each considered DEM element delivers for a given mesh an accuracy that is an order of magnitude better than that of its standard Galerkin comparable. The DEM element Q -5-1⁺ is also found to outperform the stabilized finite element Q_1 [16] by a large margin.

Table 5.5 reports the convergence rates numerically deduced from the performance results reported in Table 5.4. Each pair of elements $(Q_1, Q$ -5-1⁺), $(Q_2, Q$ -9-2⁺),

Table 5.4: Inhomogeneous problem of Section 5.6.1 defined on an L -shaped domain ($Pe = 10^3$): relative solution errors

Element	300 elements	1,200 elements	2,700 elements	10,800 elements
Q_1	4.91×10^{-1}	2.28×10^{-1}	1.46×10^{-1}	6.33×10^{-2}
Stabilized Q_1	2.26×10^{-1}	1.39×10^{-1}	1.02×10^{-1}	5.54×10^{-2}
Q -5-1 ⁺	1.29×10^{-1}	3.87×10^{-2}	2.16×10^{-2}	7.36×10^{-3}
Q_2	2.02×10^{-1}	9.13×10^{-2}	5.44×10^{-2}	1.90×10^{-2}
Q -9-2 ⁺	4.40×10^{-2}	1.24×10^{-2}	5.85×10^{-3}	1.13×10^{-3}
Q_3	1.12×10^{-1}	4.58×10^{-2}	2.46×10^{-2}	6.29×10^{-3}
Q -13-3 ⁺	3.10×10^{-2}	6.85×10^{-3}	2.10×10^{-3}	2.24×10^{-4}
Q_4	6.89×10^{-2}	2.45×10^{-2}	1.13×10^{-2}	1.92×10^{-3}
Q -17-4 ⁺	2.74×10^{-2}	2.42×10^{-3}	4.92×10^{-4}	1.24×10^{-4}

(Q_3 , Q -13-3⁺) and (Q_4 , Q -17-4⁺) is found to have a comparable convergence rate. However, Figure 5.5 shows that in each case, the DEM element has the smallest constant: for a given mesh size, it delivers a numerical solution that is typically one order of magnitude more accurate than those produced by its standard and stabilized Galerkin comparables. More specifically, the reader can observe that to achieve for this problem the relative error of 0.1%:

- The DEM element Q -5-1⁺ requires 6.4 times fewer dofs than the Galerkin element Q_1 .
- The DEM element Q -9-2⁺ requires 8.3 times fewer dofs than the Galerkin element Q_2 .
- The DEM element Q -13-3⁺ requires 5.7 times fewer dofs than the Galerkin element Q_3 .
- The DEM element Q -17-4⁺ requires 4.3 times fewer dofs than the Galerkin element Q_4 .

These results demonstrate the computational superiority of the DEM methodology.

The performance results reported in Table 5.5 also reveal that increasing the number of enrichment functions of a DEM element reduces the number of dofs needed for achieving a specified accuracy, thereby illustrating the higher-order behavior of a DEM element with an increasing value of n^E .

Table 5.5: Inhomogeneous problem of Section 5.6.1 defined on an L -shaped domain ($Pe = 10^3$): convergence rates

Element	Convergence rate*	Required # dofs to achieve the relative error of 10^{-2}
Q_1	1.44	139,649
Stabilized Q_1	1.16	198,020
Q -5-1 ⁺	1.55	21,834
Q_2	1.94	62,721
Q -9-2 ⁺	2.37	7,568
Q_3	2.67	33,707
Q -13-3 ⁺	3.23	5,935
Q_4	3.50	20,796
Q -17-4 ⁺	3.26	4,802

* The convergence rates reported in Table 5.5 for the standard Galerkin elements are slightly below the theoretical rates associated with the L^2 norm, because they are derived from numerical experiments and mesh resolutions for which these elements have not reached asymptotic convergence.

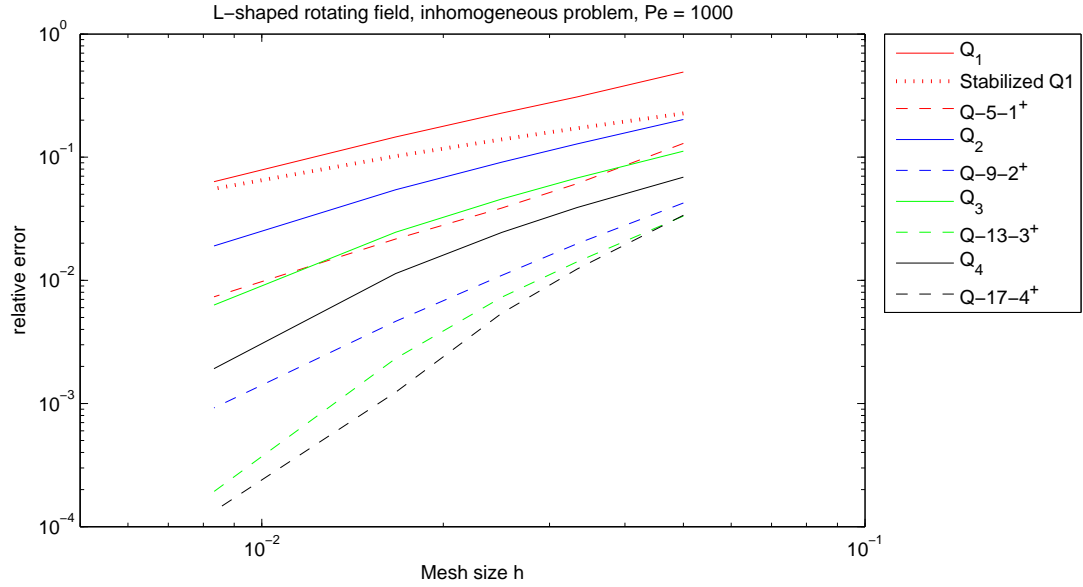


Figure 5.5: Inhomogeneous problem of Section 5.6.1 defined on an L -shaped domain ($Pe = 10^3$): decrease of the relative solution error with the mesh size

5.6.2 Thermal boundary layer problem

Next, the following variable-coefficient BVP, whose boundary conditions are illustrated in Figure 5.6, is considered

$$\begin{aligned}
 \left(y, 0 \right)^T \cdot \nabla c(\mathbf{x}) - \kappa \Delta c(\mathbf{x}) &= 0, & \text{in } \Omega = (0, 1)^2, \\
 c(0, y) &= 1, & 0 \leq y \leq 1, \\
 c(1, y) &= y, & 0 \leq y \leq 1, \\
 c(x, 0) &= 1 - \frac{x}{\epsilon}, & 0 \leq x \leq \epsilon, \\
 c(x, 0) &= 0, & \epsilon \leq x \leq 1, \\
 c(x, 1) &= 1, & 0 \leq x \leq 1.
 \end{aligned} \tag{5.66}$$

The parameter $0 < \epsilon \ll 1$ ensures that the above BVP is well-posed. It is set here to $\epsilon = 1/10$. The diffusivity constant is set to $\kappa = 10^{-3}$, which sets the Péclet number

to $Pe = 10^3$. Variants of this problem have been used to assess the performance of stabilized finite elements [20, 22, 23] and other finite elements with enriched approximation spaces [53, 65]. This problem is referred to here as a thermal boundary layer problem as it may be viewed as a model problem for the formation of a pair of thermal boundary layers along the lower and outflow boundaries of a fully developed shear flow between two parallel plates with the lower one fixed, and the upper one moving to the right. In this context, $c(\mathbf{x})$ represents the temperature at a point $\mathbf{x} \in \Omega \subset \mathbb{R}^2$. This BVP involves a relatively simple variable advection field. However, its solution features both an outflow boundary layer at $x = 1$, and a parabolic layer along $y = 0$. As such, it is a challenging problem for standard Galerkin elements (see Figures 5.7 and 5.8 (a),(c), (e)).

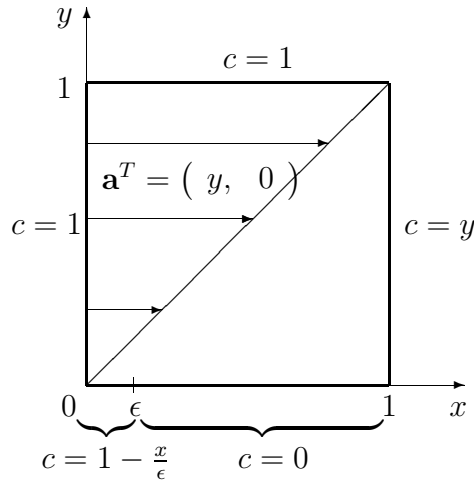


Figure 5.6: Thermal boundary layer problem of Section 5.6.2: domain and boundary conditions

Table 5.6 reports the relative solution errors associated with the discretization of the above problem by the variable-coefficient variants of the DGM and DEM elements introduced Section 4.3, and standard and stabilized Galerkin using four different uniform meshes. As for the problem of Section 5.6.1, the error analysis is performed with respect to a reference solution computed using the higher-order Galerkin element Q_6 and a uniform mesh with an element size $h = 1/120$. In the first column of this

table, n denotes the number of elements in one direction. Therefore, the total number of elements is $n^{el} = n^2$ and the size of an element is $h = \frac{1}{n}$. Figure 5.7 and Figure 5.8 display the front and rear views of the standard Galerkin and DGM solutions, respectively. The following observations are noteworthy:

- Although the first-order DGM element Q -4-1 is outperformed by the DEM element Q -5-1⁺ which has a slightly higher computational complexity, the Q -4-1 element outperforms both the standard and stabilized Galerkin elements Q_1 which have a comparable computational complexity.
- Despite the fact that the homogeneous problem considered here is a variable-coefficient BVP and therefore locally equivalent to an inhomogeneous constant-coefficient problem (see (5.10)–(5.12)), the DGM elements are found to become as effective as the DEM elements at solving it when more enrichment functions are added to \mathcal{V}_e^E .
- In general, the DGM and DEM elements are found to deliver for a given mesh a significantly better accuracy than their standard Galerkin comparables. When the number of enrichment functions is increased, the higher-order DGM and DEM elements are shown to produce numerical solutions that are an order of magnitude more accurate than those computed by their standard higher-order Galerkin comparables.
- Whereas the solutions computed using the DGM and DEM discretizations are continuous and smooth, those computed using the Galerkin discretizations — including the higher-order ones — are contaminated by spurious, non-physical oscillations near the outflow boundary ($x = 1$).

5.6.3 Lid-driven cavity flow problem

The lid-driven cavity flow problem is a well known validation problem for codes and numerical methods in the field of computational fluid mechanics. The problem is posed on a simple two-dimensional (2D) square domain $\Omega \equiv (0, 1)^2 \in \mathbb{R}^2$, representing

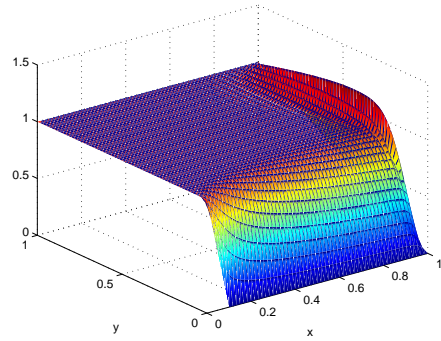
Table 5.6: Thermal boundary layer problem of Section 5.6.2 ($Pe = 10^3$): relative solution errors

Element	$n = 10$	$n = 15$	$n = 20$	$n = 30$
Q_1	$4.00e \times 10^{-1}$	1.16×10^{-1}	9.47×10^{-2}	5.74×10^{-2}
Stabilized Q_1	8.42×10^{-2}	6.55×10^{-2}	5.49×10^{-2}	4.20×10^{-2}
Q -4-1	6.48×10^{-2}	4.97×10^{-2}	3.79×10^{-2}	2.25×10^{-2}
Q -5-1 ⁺	1.22×10^{-2}	7.07×10^{-3}	4.25×10^{-3}	2.12×10^{-3}
Q_2	9.54×10^{-2}	5.10×10^{-2}	3.62×10^{-2}	2.20×10^{-2}
Q -8-2	2.10×10^{-2}	9.37×10^{-3}	4.43×10^{-3}	1.50×10^{-3}
Q -9-2 ⁺	4.62×10^{-3}	4.56×10^{-3}	9.71×10^{-4}	5.56×10^{-4}
Q_3	4.52×10^{-2}	2.72×10^{-2}	1.87×10^{-2}	1.04×10^{-2}
Q -12-3	5.55×10^{-3}	3.98×10^{-3}	8.38×10^{-4}	5.19×10^{-4}
Q -13-3 ⁺	2.98×10^{-3}	4.24×10^{-3}	7.94×10^{-4}	5.16×10^{-4}
Q_4	2.77×10^{-2}	1.61×10^{-2}	1.05×10^{-2}	5.29×10^{-3}
Q -16-4	3.73×10^{-3}	4.03×10^{-3}	7.56×10^{-4}	4.99×10^{-4}
Q -17-4 ⁺	2.79×10^{-3}	4.21×10^{-3}	7.22×10^{-4}	5.08×10^{-4}

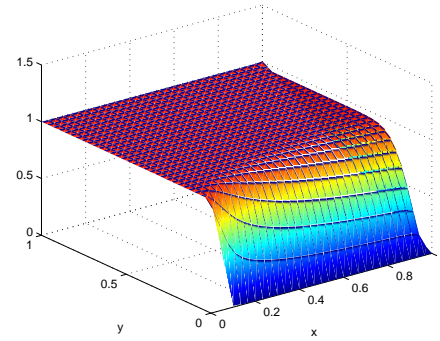
a cavity assumed to contain fluid. The velocity field solution $\mathbf{a}(\mathbf{x})$ to this problem is obtained by solving the time-dependent, incompressible 2D Navier-Stokes equations (1.1) on the domain $\Omega = (0, 1)^2$ with the boundary conditions illustrated in Figure 5.9 (a), and converging this solution to a steady state³. Three sides of the cavity (the bottom, left and right sides) are stationary. No-slip and no-penetration boundary conditions are applied along these walls. The top region is open, and has a purely tangential, constant velocity $a_1 = const > 0$. The movement of the fluid parallel to the upper boundary causes a rotating, recirculation region to form in the cavity (Figure 5.9 (b)).

Given the numerically-computed advection field shown in Figure 5.9 (a) and 5.10,

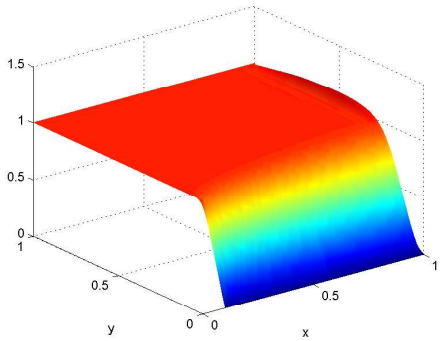
³This solution, computed on a 41×41 node uniform mesh of $\Omega = (0, 1)^2$, was downloaded from the dataset library [66].



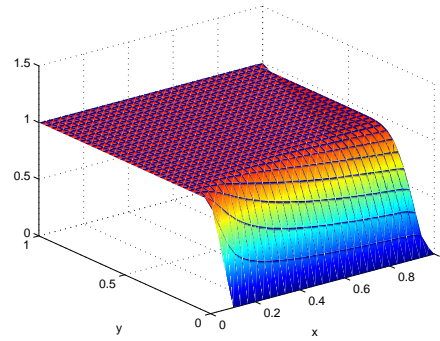
(a) Galerkin element Q_2



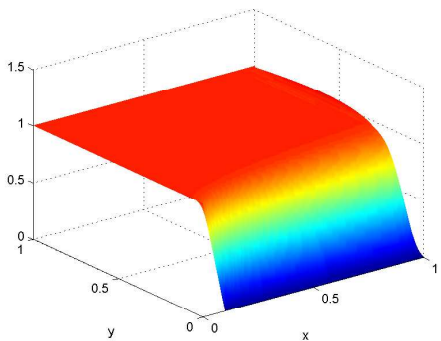
(b) DGM element $Q-8-2$



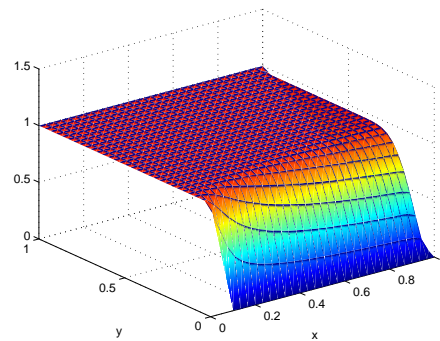
(c) Galerkin element Q_3



(d) DGM element $Q-12-3$

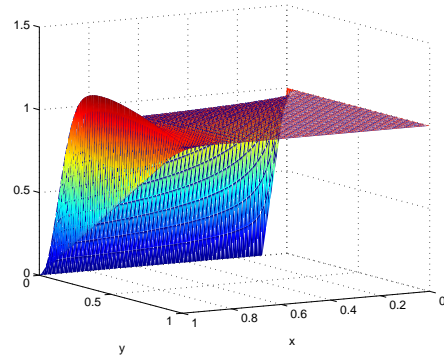


(e) Galerkin element Q_4

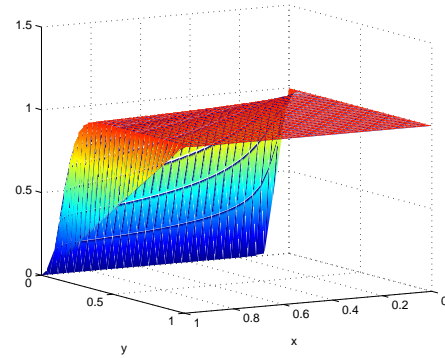


(f) DGM element $Q-16-4$

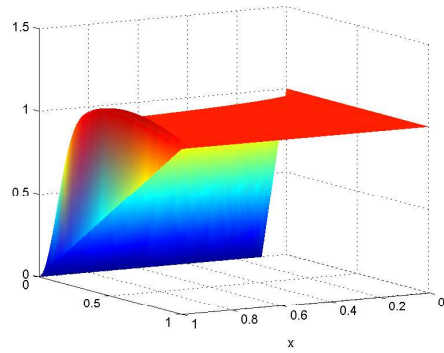
Figure 5.7: Thermal boundary layer problem of Section 5.6.2 $\left(Pe = 10^3, h = \frac{1}{30} \right)$: front views of the computed solutions



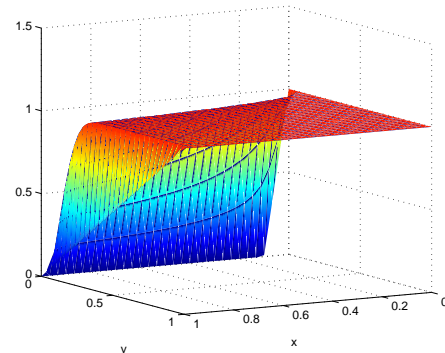
(a) Galerkin element Q_2



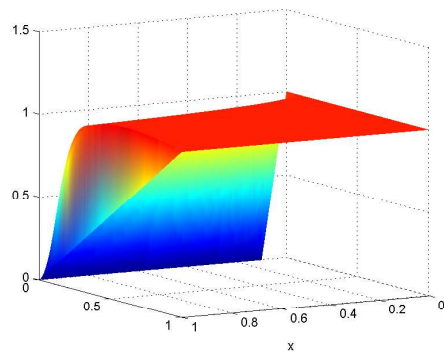
(b) DGM element $Q-8-2$



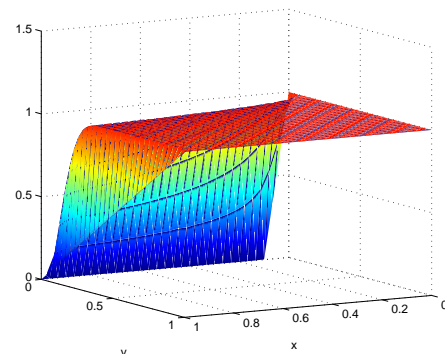
(c) Galerkin element Q_3



(d) DGM element $Q-12-3$



(e) Galerkin element Q_4



(f) DGM element $Q-16-4$

Figure 5.8: Thermal boundary layer problem of Section 5.6.2 $\left(Pe = 10^3, h = \frac{1}{30} \right)$: rear views of the computed solutions

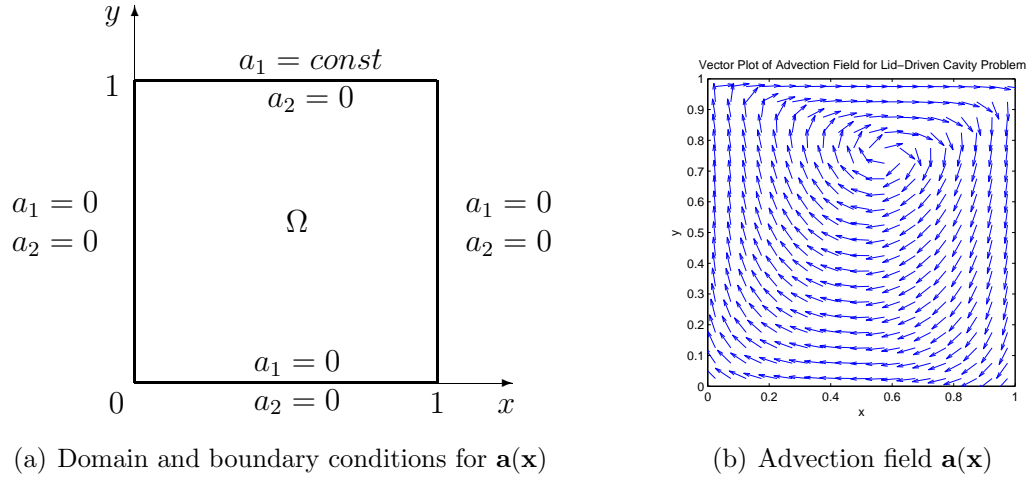


Figure 5.9: Domain, boundary conditions and $\mathbf{a}(\mathbf{x})$ for the lid-driven cavity flow problem of Section 5.6.3

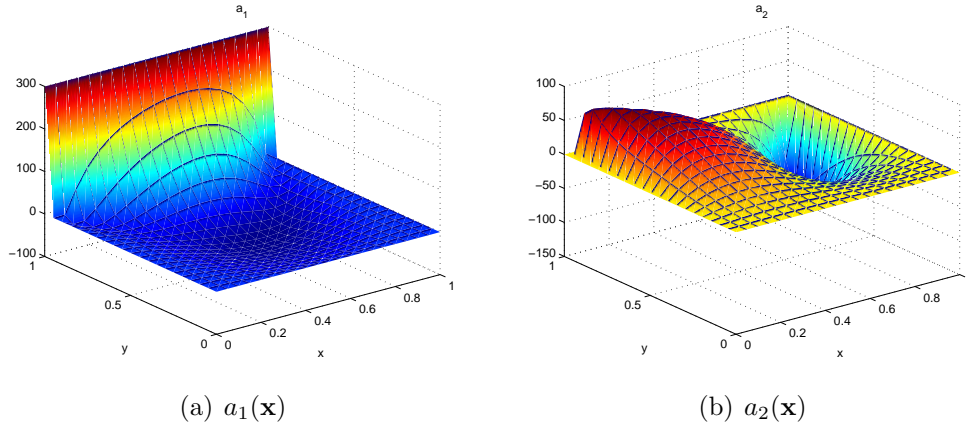


Figure 5.10: Components a_1 and a_2 of the advection field for the lid-driven cavity flow problem of Section 5.6.3

DEM and the standard Galerkin FEM are evaluated on the following advection-diffusion BVP for the concentration $c(\mathbf{x})$:

$$\begin{aligned}
 \mathbf{a}(\mathbf{x}) \cdot \nabla c(\mathbf{x}) - \kappa \Delta c(\mathbf{x}) &= 0, & \text{in } \Omega = (0, 1)^2, \\
 c(0, y) &= 0, & 0 \leq y \leq 1, \\
 c(1, y) &= 1, & 0 \leq y \leq 1, \\
 \frac{\partial c(\mathbf{x})}{\partial \mathbf{n}} \Big|_{y=0} &= \frac{\partial c(\mathbf{x})}{\partial \mathbf{n}} \Big|_{y=1} = 0, & 0 \leq x \leq 1.
 \end{aligned} \tag{5.67}$$

A convergence study is performed for $\kappa = 0.01$ ($Pe \approx 260$), on uniform meshes with mesh increment $h = \frac{1}{10}, \frac{1}{15}$ and $\frac{1}{20}$. The reference solution taken in place of the exact solution is a solution computed on a uniform 40×40 mesh using a Galerkin Q_6 element. The advection field $\mathbf{a}(\mathbf{x})$ is interpolated in all computations, including the computation of the reference solution, using bilinear Lagrange interpolation functions (Example 7.1.6 in the Appendix).

Table 5.7: Lid-driven cavity flow problem of Section 5.6.3 ($\kappa = 10^{-2}$, $Pe \approx 260$): relative solution errors

Element	$n = 10$	$n = 15$	$n = 20$
Q_1	2.68×10^{-1}	1.88×10^{-1}	3.27×10^{-2}
$Q-(4,0)-1$	4.67×10^{-1}	3.19×10^{-1}	7.85×10^{-2}
$Q-(4,0)^*-1$	2.18×10^{-1}	1.74×10^{-1}	2.22×10^{-2}
$Q-5-1^+$	2.53×10^{-1}	9.74×10^{-2}	1.67×10^{-2}
Q_2	3.68×10^{-1}	1.28×10^{-1}	1.12×10^{-2}
$Q-(4,5)-2$	2.48×10^{-1}	8.07×10^{-2}	1.43×10^{-3}
$Q-(4,5)^*-2$	2.01×10^{-1}	5.41×10^{-2}	9.46×10^{-4}
$Q-9-2^+$	2.24×10^{-1}	7.32×10^{-2}	3.64×10^{-3}
Q_3	2.34×10^{-1}	7.91×10^{-2}	3.30×10^{-3}
$Q-(4,9)-3$	2.01×10^{-1}	7.41×10^{-2}	6.31×10^{-4}
$Q-(4,9)^*-3$	1.87×10^{-1}	4.28×10^{-2}	4.44×10^{-4}
$Q-13-3^+$	2.18×10^{-1}	7.36×10^{-2}	7.81×10^{-4}
Q_4	2.36×10^{-1}	7.90×10^{-2}	1.08×10^{-3}
$Q-(4,13)-4$	2.00×10^{-1}	7.30×10^{-2}	4.84×10^{-4}
$Q-(4,13)^*-4$	1.76×10^{-1}	4.00×10^{-2}	4.04×10^{-4}
$Q-17-4^+$	2.21×10^{-1}	7.63×10^{-2}	4.65×10^{-4}

Table 5.7 reports the relative errors in the solution to this problem computed by the Galerkin Q_1 , Q_2 , Q_3 and Q_4 , the pure DGM $Q-(4,0)-1$, $Q-(4,5)-2$, $Q-(4,9)-3$, $Q-(4,13)-4$, $Q-(4,0)^*-1$, $Q-(4,5)^*-2$, $Q-(4,9)^*-3$, $Q-(4,13)^*-4$ elements, and the true DEM $Q-5-1^+$, $Q-9-2^+$, $Q-13-3^+$, $Q-17-4^+$ elements. The decrease in the relative solution errors with respect to the mesh size is plotted in Figure 5.12–5.14. Figure 5.11 compares the Q_2 solution with the DGM $Q-(4,5)-2$ solution when the diffusivity is set to $\kappa = 0.005$ and the mesh size is $h = \frac{1}{40}$. The following are conclusions drawn from these results:

- The pure DGM elements $Q-(4, 5)-2$, $Q-(4, 9)-3$ and $Q-(4, 13)-4$ deliver a solution that is in general at least as accurate as the solution delivered by their true DEM element counterparts, namely the $Q-9-2^+$, $Q-13-3^+$ and $Q-17-4^+$ respectively (Figures 5.12 and 5.14). The former three elements are recommended, as they have a smaller computational complexity.
- On the finest mesh considered, for which the mesh increment is $h = \frac{1}{20}$, the $Q-(4, 5)-2$ pure DGM element outperforms its Galerkin counterpart, the Q_2 element, by an order of magnitude. The $Q-(4, 9)-3$ pure DGM outperforms its Galerkin comparable of similar computational complexity, namely the Q_3 element, by almost an order of magnitude on this finest mesh (Figure 5.12).
- The similar performance of all elements evaluated on the coarsest mesh, for which the mesh increment is $h = \frac{1}{10}$, can be attributed to the under-interpolation of the advection field $\mathbf{a}(\mathbf{x})$ (relative to the $\mathbf{a}(\mathbf{x})$ used in computing the reference solution) on this coarse mesh. Accuracy at the finer mesh resolutions would improve if the $\mathbf{a}(\mathbf{x})$ used in all computation was defined on the same mesh as the reference solution.
- The reader can infer the effect of augmenting the enrichment field \mathcal{V}^E of each of the pure DGM elements with the “higher order” enrichment function (5.49) by comparing Figure 5.13 with Figure 5.12. As expected, all augmented elements $Q-(n^{\text{pol}}, n^{\text{exp}})^*-n^\lambda$ outperform their un-augmented analogs, denoted by $Q-(n^{\text{pol}}, n^{\text{exp}})-n^\lambda$.
- The $Q-(4, 0)-1$ DGM element is not performing well on this problem. Recall that this element’s approximation space consists of only polynomial free-space solutions to (1.2). Hence the local polynomial free-space solutions to (1.2) comprising the field $\mathcal{V}_e^{\text{pol}}$ do not seem to be sufficient for this problem – the exponential enrichment field $\mathcal{V}_e^{\text{exp}}$ are needed as well.
- All pairs of elements in the following quadruples of elements $(Q_1, Q-(4, 0)-1,$

$Q_-(4, 0)^*-1$, $Q_-(5-1^+)$, $(Q_2, Q_-(4, 5)-2, Q_-(4, 5)^*-2, Q_-(9-2^+)$, $(Q_3, Q_-(4, 9)-3, Q_-(4, 9)^*-3, Q_-(13-3^+)$ and $(Q_4, Q_-(4, 13)-4, Q_-(4, 13)^*-4, Q_-(17-4^+)$ have a comparable convergence rate *a posteriori*.

- The reader may observe that the Q_2 solution is contaminated by spurious oscillations near the point $(x, y) = (1, 1)$; in contrast, the DGM $Q_-(4, 5)-2$ solution is smooth and oscillation free everywhere in the computational domain (Figure 5.11).

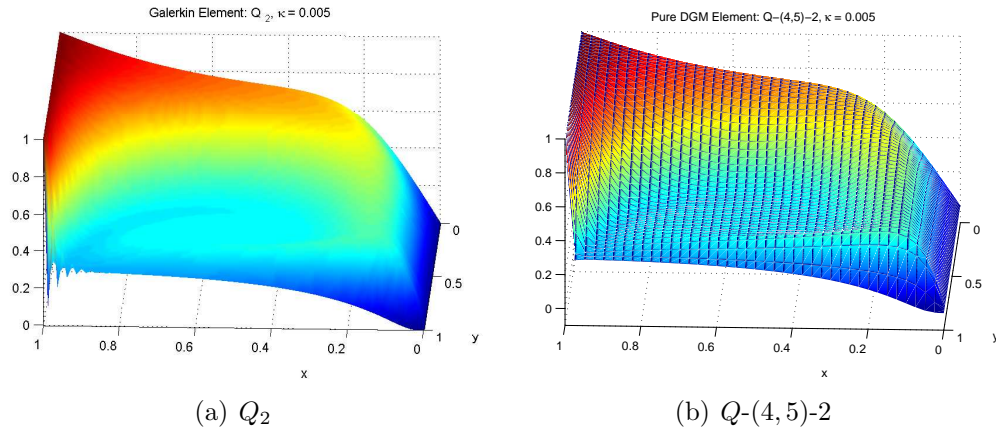


Figure 5.11: Solution plots $c(\mathbf{x})$ to the advection-diffusion equation for the lid-driven cavity flow problem of Section 5.6.3 ($\kappa = 0.005$ and 40×40 uniform mesh)

5.6.4 Differentially-heated cavity problem

The final benchmark problem is that of a differentially heated cavity, a variant of the problem in Section 3.2 of [67]. The problem is posed in a square domain $\Omega = (0, 1)^2$ representing a differentially heated cavity filled with air. In this context, the scalar solution to (1.2) $c(\mathbf{x})$ represents the temperature. The left and right walls are isothermal with boundary conditions $c = 302.5$ and $c = 313.5$ respectively, and the top and bottom walls are adiabatic ($\frac{\partial c}{\partial \mathbf{n}} = 0$). The boundary conditions on the advection (velocity) field are no-slip conditions: $\mathbf{a} = \mathbf{0}$ on $\partial\Omega$. The physical scenario being modeled is one in which the left wall is cooled and the right wall is heated

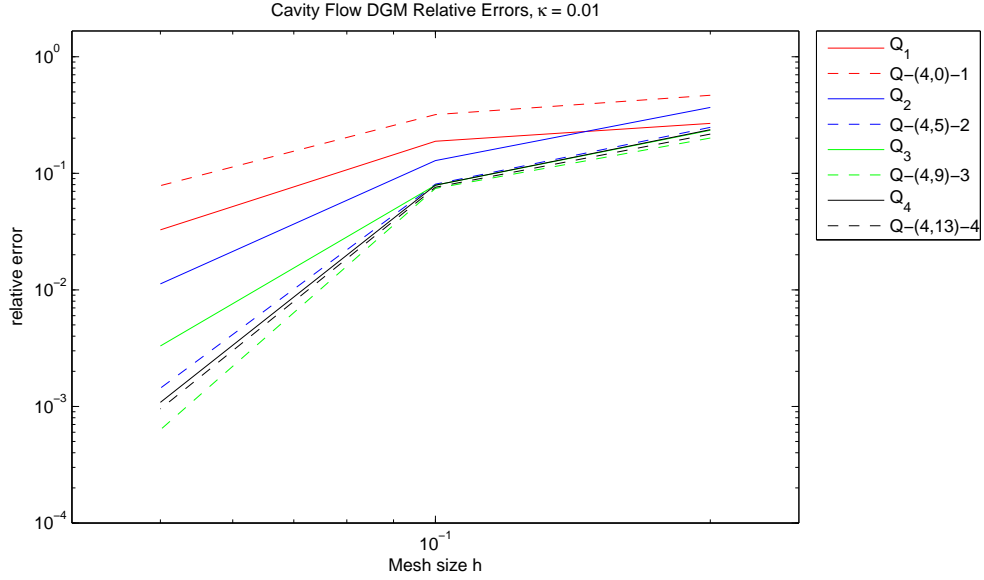


Figure 5.12: Lid-driven cavity flow problem of Section 5.6.3: decrease of the relative solution error with the mesh size ($\kappa = 0.01$, $Pe \approx 260$) for the pure DGM elements

(Figure 5.15 (a)). The result is an induced velocity field that flows counterclockwise within the domain (Figure 5.15 (b) and Figure 5.16). This velocity (advection) is obtained numerically by solving the unsteady compressible Navier-Stokes equations in the near-incompressible (low Mach number) regime, converging the solution to a steady state⁴.

Given the advection field $\mathbf{a}(\mathbf{x})$, DEM and the standard Galerkin FEM are evaluated on the following advection-diffusion BVP for the temperature $c(\mathbf{x})$

$$\begin{aligned}
 \mathbf{a}(\mathbf{x}) \cdot \nabla c(\mathbf{x}) - \kappa \Delta c(\mathbf{x}) &= 0, & \text{in } \Omega = (0, 1)^2, \\
 c(0, y) &= 302.5, & 0 \leq y \leq 1, \\
 c(1, y) &= 313.5, & 0 \leq y \leq 1, \\
 \frac{\partial c(\mathbf{x})}{\partial \mathbf{n}} \Big|_{y=0} &= \frac{\partial c(\mathbf{x})}{\partial \mathbf{n}} \Big|_{y=1} = 0, & 0 \leq x \leq 1.
 \end{aligned} \tag{5.68}$$

⁴This solution was computed numerically in AERO-F [68], a finite volume CFD code, using a 512×512 uniform mesh of the domain $\Omega = (0, 1)^2$.

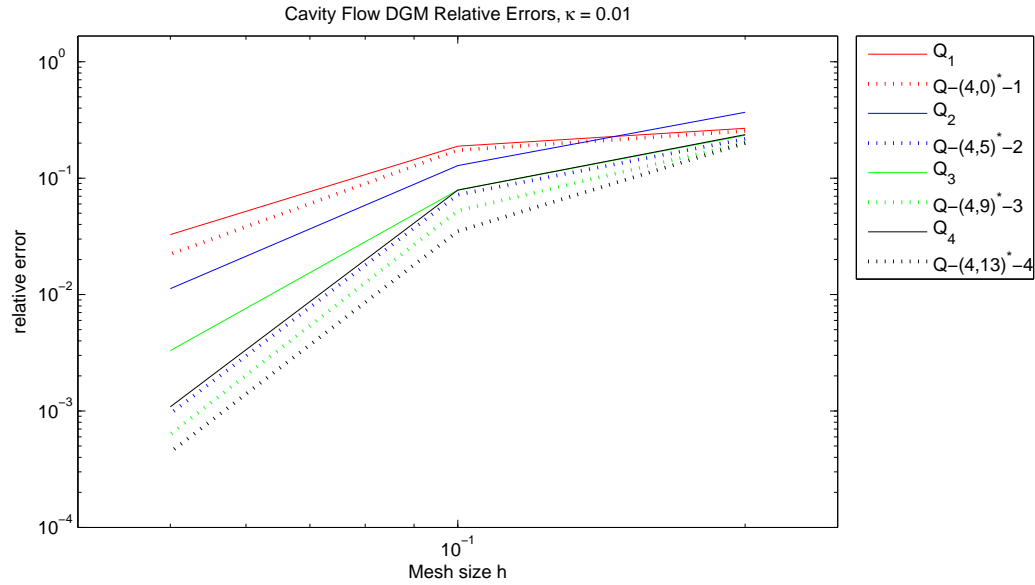


Figure 5.13: Lid-driven cavity flow problem of Section 5.6.3: decrease of the relative solution error with the mesh size ($\kappa = 0.01$, $Pe \approx 260$) for the pure DGM elements with higher order enrichment function

The value of κ was set to 2.22×10^{-5} , which corresponds to a global Péclet number of ≈ 1530 .

All computed solutions are compared to a reference solution, obtained by solving (5.68) numerically using a fine mesh and a high order polynomial interpolant. More specifically, this reference solution was obtained by solving (5.68) using a Galerkin Q_4 element and a 256×256 uniform mesh. A convergence study of various DGM, DEM and Galerkin elements was performed, relative to this reference solution, on meshes of 8×8 , 16×16 and 32×32 elements (Figure 5.18). The advection field $\mathbf{a}(\mathbf{x})$ was interpolated, in all computations, using biquadratic Lagrange interpolation functions.

The performance results for this problem are summarized in Figures 5.17–5.20. The following observations are noteworthy:

- The first order true DEM element $Q-5-1^+$ produces a more accurate solution than its Galerkin counterpart of comparable convergence order, the Q_1 element,

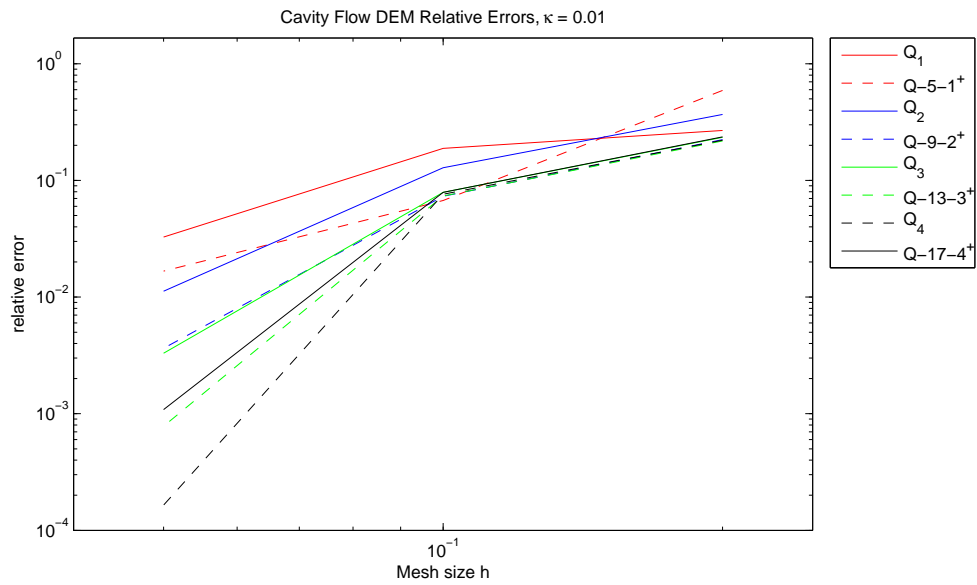


Figure 5.14: Lid-driven cavity flow problem of Section 5.6.3: decrease of the relative solution error with the mesh size ($\kappa = 0.01$, $Pe \approx 260$) for the true DEM elements

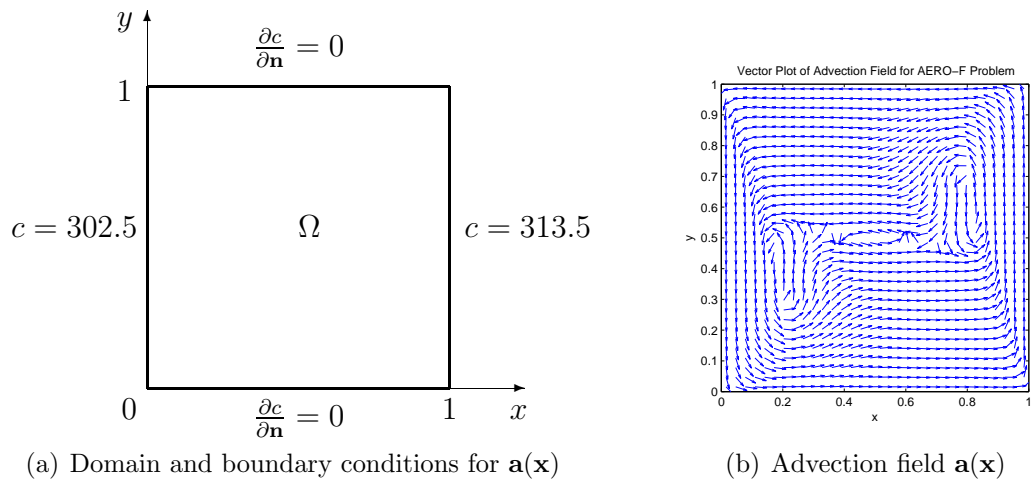


Figure 5.15: Domain, boundary conditions and $\mathbf{a}(\mathbf{x})$ for the differentially-heated cavity problem of Section 5.6.4

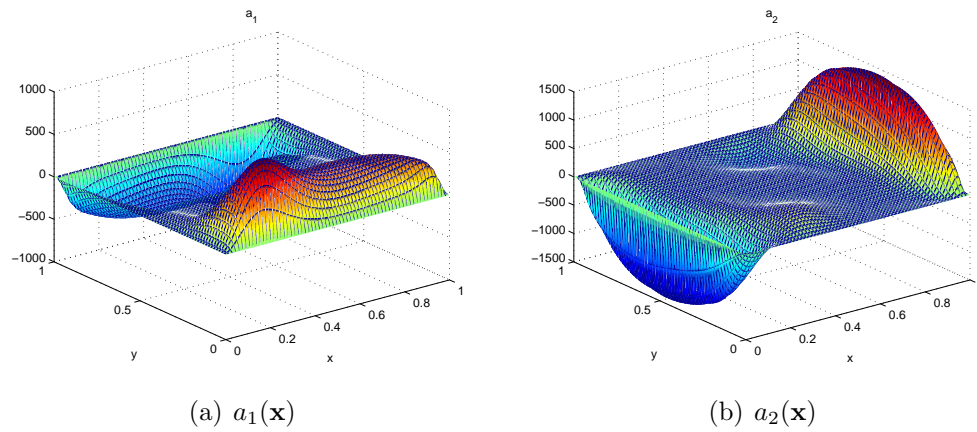


Figure 5.16: Components a_1 and a_2 of the advection field for the differentially-heated cavity problem of Section 5.6.4

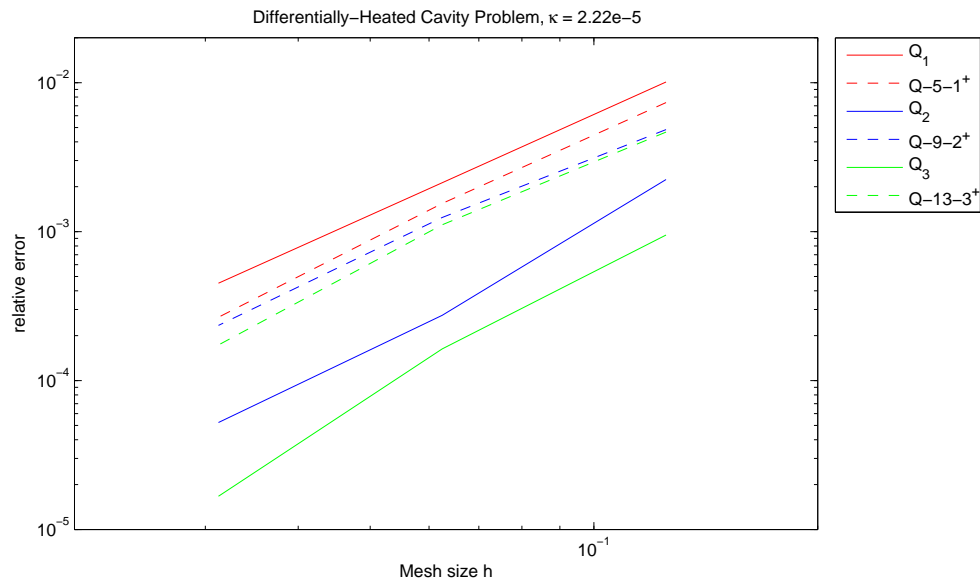


Figure 5.17: Differentially-heated cavity problem of Section 5.6.4: decrease of the relative solution error with the mesh size ($\kappa = 2.22 \times 10^{-5}$, $Pe \approx 1530$) for the true DEM elements

at a given mesh resolution (Figure 5.17).

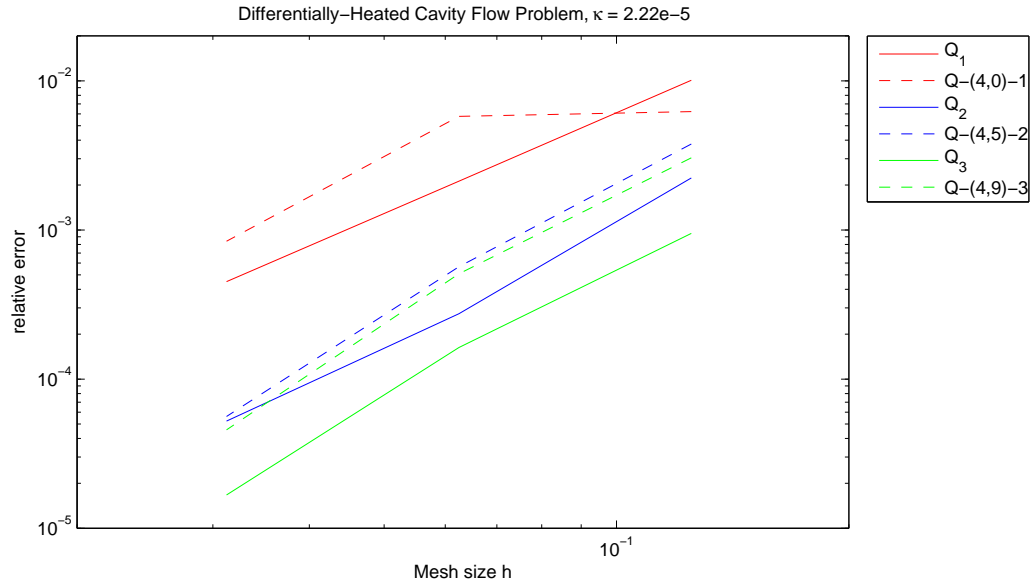


Figure 5.18: Differentially-heated cavity problem of Section 5.6.4: decrease of the relative solution error with the mesh size ($\kappa = 2.22 \times 10^{-5}$, $Pe \approx 1530$) for the pure DGM elements

- However, neither the second nor the third order true DEM elements, denoted Q_{9-2^+} and Q_{13-3^+} respectively, outperform their Galerkin comparables, namely the Q_2 and Q_3 elements (Figure 5.17).
- The situation is better for the pure DGM elements, $Q_{-(4,5)-2}$ and $Q_{-(4,13)-3}$, each of which deliver a more accurate solution than their true DEM counterparts, the Q_{9-2^+} and Q_{13-3^+} elements. The former two elements achieve a solution that is comparable in accuracy to the Q_2 solution as the mesh is refined (Figure 5.18).
- Figure 5.19 (a), (b) and (c) show contours of the solutions, computed with the Galerkin Q_2 , the true DEM Q_{9-2^+} and the pure DGM $Q_{-(4,5)-2}$ elements respectively, on a relatively coarse 16×16 mesh with $\kappa = 2.22 \times 10^{-5}$ ($Pe \approx 1530$). Oscillations near that $(x, y) = (0, 1)$ corner are apparent in the Q_2 solution (Figure 5.19 (a)). The Q_{9-2^+} solution (Figure 5.19 (b)) contains oscillations as well,

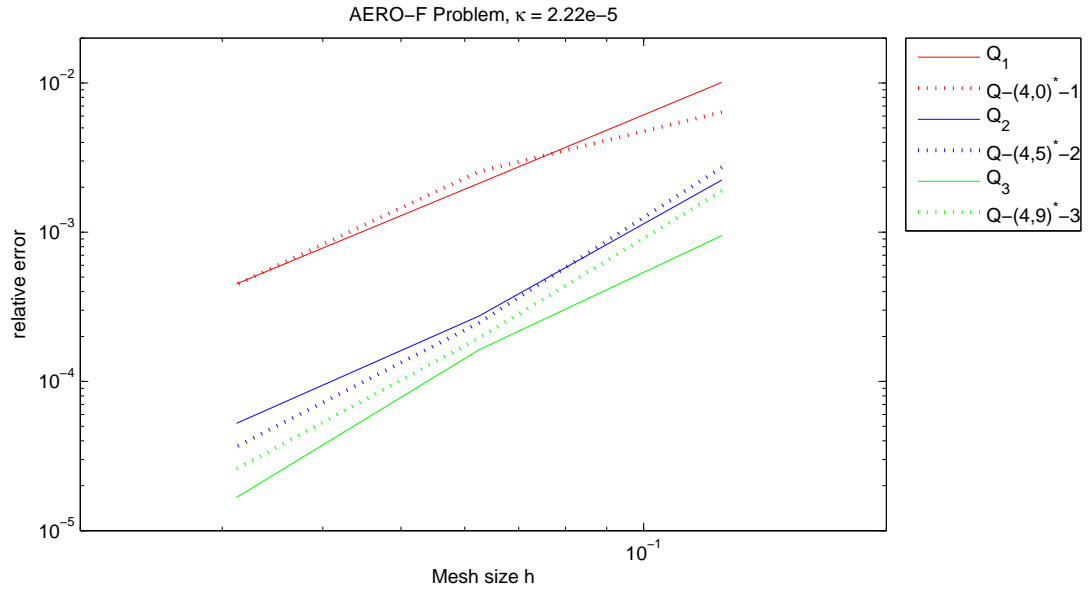


Figure 5.20: Differentially-heated cavity problem of Section 5.6.4: decrease of the relative solution error with the mesh size ($\kappa = 2.22 \times 10^{-5}$, $Pe \approx 1530$) for the pure DGM elements with higher order enrichment function

is not performing well, which suggests the polynomial enrichment field $\mathcal{V}_e^{\text{pol}}$ is not sufficient on its own to capture well the solution to this problem.

- The reader may observe by comparing Figure 5.20 with Figure 5.18 that, in contrast with the pure DGM elements $Q-(4, 5)-2$ and $Q-(4, 13)-3$, the augmented pure DGM elements $Q-(4, 5)^*-2$ and $Q-(4, 9)^*-3$ outperform the Q_2 element at all mesh resolutions h considered.
- None of the pure DGM or true DEM elements evaluated here outperform the Galerkin Q_3 element, however. This suggests that the definition of the enrichment field may put a limit on the accuracy a DGM or DEM element can deliver when the element is used to solve certain variable-coefficient problems.
- To this effect, it is conjectured that, for a DGM element to outperform the Q_3 element, its enrichment space would need to be augmented by a still higher order enrichment function, namely the free-space solution to (2.1) with $\mathbf{a}(\mathbf{x})$

linearized within each element to third order:

$$\mathbf{a}(\mathbf{x}) = \mathbf{a}(\bar{\mathbf{x}}^e) + \nabla \mathbf{a}|_{\mathbf{x}=\bar{\mathbf{x}}^e} \cdot (\mathbf{x} - \bar{\mathbf{x}}^e) + (\mathbf{x} - \bar{\mathbf{x}}^e)^T \nabla^2 \mathbf{a}|_{\mathbf{x}=\bar{\mathbf{x}}^e} \cdot (\mathbf{x} - \bar{\mathbf{x}}^e) \quad \text{in } \Omega^e. \quad (5.69)$$

Chapter 6

Conclusions and future work

This dissertation lays down the foundation required to apply the discontinuous enrichment method (DEM) to multi-scale problems in fluid mechanics. Attention is focused specifically on the advection-diffusion equation, a basic transport equation that arises in fluid mechanics applications. This equation is significant both in its relevance in describing physical phenomena of interest in science and engineering applications, as well as as a precursor for studying more complex fluid equations, such as the Navier-Stokes equations. The following is a summary of the primary contributions of this dissertation, followed by some suggestions for avenues of future research.

6.1 Summary of dissertation contributions

The primary contribution of this dissertation is the development of a discontinuous enrichment method that can be used with an h - and/or a p -mesh-refinement computational strategy for the efficient finite element solution of high Péclet constant-coefficient and variable-coefficient advection-diffusion equations (1.2) in two spatial dimensions (2D). In this method, the usual Galerkin polynomial approximation is locally enriched (or, in some cases replaced) by the free-space solution to the governing homogeneous PDE. To this effect, several families of enrichment functions are derived for the advection-diffusion equation. These families include:

- A set of exponential free-space solutions to the constant-coefficient advection-diffusion equation, each exhibiting a sharp gradient in some direction $\theta_i \in [0, 2\pi)$.
- A set of polynomial free-space solutions to the constant-coefficient advection-diffusion equation that may be derived up to any desired degree n .
- A “higher-order” enrichment function that solves the advection-diffusion equation with $\mathbf{a}(\mathbf{x})$ linearized to first order in the case when the advection field is spatially varying.

A corresponding dual space of Lagrange multiplier approximations that are related to the normal traces of the aforementioned enrichment functions, introduced to enforce a weak continuity of the approximation across the element interfaces, is constructed. The issue of potential redundancy in these approximations in the context of higher-order elements *and* variable-coefficient problems is illuminated and addressed. Several low as well as higher-order DGM and DEM elements are proposed for the solution of constant and variable-coefficient transport problems. The proposed elements are tested on a number of benchmark problems whose solutions are known to exhibit sharp gradients in the high Péclet regime, and therefore cannot be solved efficiently by the standard Galerkin FEM. These numerical experiments demonstrate the superiority of the proposed discretization method over the standard p -type Galerkin finite element method: the proposed higher-order DGM and DEM elements are found in general to achieve higher convergence rates as the p -type FEM, but with much smaller (in some cases, orders of magnitude smaller) error constants.

6.2 Future work

The work presented in this dissertation has illuminated some possible avenues for future research, which are described briefly here.

- The potential of DEM for multi-scale advection-diffusion problems in the high Péclet regime was illustrated numerically in this dissertation. The higher-order

behavior of DGM and DEM elements with increasing n^E was also illustrated numerically. A rigorous mathematical analysis of the stability (in the *inf-sup* sense) and convergence of the DGM and DEM elements proposed in this dissertation is lacking at the present time. Future work may attempt to address the following lingering theoretical questions.

- Can it be proven that the bilinear form $b(\mu_h, c^h)$ for the elements developed in this dissertation satisfies the *continuous* Babuška-Brezzi *inf-sup* condition?
- Can the convergence and order of these elements be established *a priori*?
- In all the numerical experiments presented in this dissertation, the same number of enrichment function n^E was employed in each element of the mesh. Future work may involve the development of a solution-adaptive DEM, that is, a version of DEM in which enrichment is added only in elements where it is needed.
- In the version of DEM presented in this dissertation, the enrichment functions were derived analytically. Future versions of DEM may employ enrichment fields that are computed numerically. Numerically generated enrichments have been explored in the context of other methods and other equations; *cf.* [69] for an example of numerical enrichment in a PUM framework.
- The methodology developed in this dissertation for the specific case of the constant and variable-coefficient advection-diffusion equation has a natural extension to more complex equations and problems in fluid mechanics, namely unsteady and non-linear problems. To this effect, future work may involve combining the methodology developed in this dissertation with the Chorin-Temam projection method (or some variant of this method) [11, 70, 71] to build a discontinuous enrichment method for the incompressible, unsteady Navier-Stokes equations.

Chapter 7

Appendix

7.1 Review of the classical Galerkin FEM and stabilized FEMs

This section provides a brief review of the classical Galerkin finite element method (Section 7.1.1) as well as some stabilized finite element methods (Section 7.1.2) in the context of the advection-diffusion BVP (2.1). This material is based on the established texts [6, 7, 8, 10, 54] and the journal article [16].

7.1.1 The classical Galerkin finite element method (FEM)

Functional settings and variational formulation

As outlined in Section 2.1, before defining the weak or variational counterpart of (S) (2.1), the spaces of test and trial functions, denoted by \mathcal{V} and \mathcal{S} respectively, must be characterized. In the standard Galerkin finite element method (FEM), per (2.8) and (2.9), since $m = 2$ for the problem of interest (2.1), these spaces are

$$\mathcal{S} = \{u : u \in H^1(\Omega), u = g \text{ on } \Gamma\}, \quad (7.1)$$

and

$$\mathcal{V} = \{w : w \in H^1(\Omega), w = 0 \text{ on } \Gamma\}. \quad (7.2)$$

Having defined the trial and test spaces, the weak form of (2.1) is obtained by taking the $L^2(\Omega)$ inner product of (2.1) with a test function $v \in \mathcal{V}$, and integrating the diffusion term by parts, that is:

$$\int_{\Omega} (\mathbf{a} \cdot \nabla c - \kappa \Delta c) v d\Omega = \underbrace{\int_{\Omega} (\mathbf{a} \cdot \nabla c + \kappa \nabla c \cdot \nabla v) d\Omega}_{=a(c,v)} - \kappa \underbrace{\int_{\Gamma} \nabla c \cdot \mathbf{n} v d\Gamma}_{=0 \text{ (since } v = 0 \text{ on } \Gamma)}. \quad (7.3)$$

It follows that the weak (or variational) form of the problem (S) (2.1), assuming a discretization by the standard Galerkin FEM, is

$$(W) : \begin{cases} \text{Given } f, g \text{ as in (2.1), find } c \in \mathcal{V} \text{ such that } \forall v \in \mathcal{S} \\ a(c, v) = (v, f), \end{cases} \quad (7.4)$$

where $a(\cdot, \cdot)$ is the following bilinear form on $\mathcal{V} \times \mathcal{S}$

$$a(c, v) \equiv \int_{\Omega} (\mathbf{a} \cdot \nabla cv + \kappa \nabla c \cdot \nabla v) d\Omega, \quad (7.5)$$

and (v, f) is the linear form

$$(v, f) \equiv \int_{\Omega} v f d\Omega. \quad (7.6)$$

The weak forms (W) (7.4) and (S) (2.1) are equivalent assuming all functions are smooth. A proof of this equivalence can be found in Section 1.4 of [6]. Note that the weak form (7.4) is non-unique (see Remark 2.2.1).

The existence and uniqueness of the solution to the variational problem (W) (7.4) is characterized by the celebrated Lax-Milgrim Theorem. The theorem relies on two fundamental concepts, namely **continuity** and **coercivity** of the bilinear form $a(\cdot, \cdot)$ (7.5). Denoting a generic Hilbert space with norm $\|\cdot\|_X$ by X , and assuming $a(\cdot, \cdot)$ is a bilinear form on $X \times X$, these concepts are defined as follows.

Definition 7.1.1. *The bilinear form $a(\cdot, \cdot)$ is **continuous** if and only if there exists a constant $M > 0$ such that $\forall u, v \in X$,*

$$|a(u, v)| \leq M \|u\|_X \|v\|_X. \quad (7.7)$$

For a continuous bilinear form, $\|a\|$ denotes the smallest constant M satisfying (7.7):

$$\|a\| = \sup_{u,v \in X} \frac{|a(u,v)|}{\|u\|_X \|v\|_X}. \quad (7.8)$$

Definition 7.1.2. The bilinear form $a(\cdot, \cdot)$ is **coercive** if there exists a constant $\alpha > 0$ such that $\forall v \in X$,

$$a(v, v) \geq \alpha \|v\|_X^2. \quad (7.9)$$

The largest α satisfying this relation is called the **coercivity constant**. A coercive bilinear form with a coercivity constant α is said to be **α -coercive**.

Given Definitions 7.1.1 and 7.1.2, one can state the **Lax-Milgrim theorem**.

Theorem (Lax-Milgrim) 7.1.3. Let X be a Hilbert space with norm $\|\cdot\|_X$ with dual space X' having norm $\|\cdot\|_{X'}$. Let $f \in X'$ and let $a(\cdot, \cdot)$ be a bilinear form on $X \times X$ that is continuous and coercive with a constant of coercivity α . Then there exists a unique $u \in X$ such that

$$a(u, v) = (f, v), \quad \forall v \in X, \quad (7.10)$$

and (7.10) is well-posed. Moreover, u satisfies

$$\|u\|_X \leq \frac{\|f\|_{X'}}{\alpha}. \quad (7.11)$$

It is straightforward to show [54] that the bilinear form (7.5) is continuous and coercive on $\mathcal{V} \times \mathcal{V}$:

$$|a(u, v)| \leq \max\{C_\Omega \|\mathbf{a}\|_\infty, \kappa\} |u|_1 |v|_1, \quad (7.12)$$

for some constant C_Ω , and

$$a(v, v) \geq \kappa |v|_1^2, \quad (7.13)$$

where $|\cdot|_1$ denotes the semi-norm defined in (2.11).

Galerkin formulation

The next step in solving (2.1) by the Galerkin FEM is to construct finite-dimensional approximations of the spaces \mathcal{V} and \mathcal{S} , denoted by \mathcal{V}^h and \mathcal{S}^h respectively. As the continuous versions of the functions $c^h \in \mathcal{S}^h$ by definition satisfy the essential boundary conditions on Γ , and $w^h \in \mathcal{V}^h$ vanishes on Γ , it is common to write $c^h \in \mathcal{S}^h$ as:

$$c^h = v^h + g^h \in \mathcal{S}^h, \quad (7.14)$$

where $v^h \in \mathcal{V}^h$ and g^h results in satisfaction, or at least approximate satisfaction, of the boundary condition $c = g$ on Γ . One can now state the Galerkin form of the problem (7.4):

$$(G) : \begin{cases} \text{Given } f, g \text{ as in (7.4), find } c^h = v^h + g^h \in \mathcal{S}^h \text{ such that } \forall w^h \in \mathcal{V}^h \\ a(v^h, w^h) = (w^h, f) - a(g^h, w^h). \end{cases} \quad (7.15)$$

At this point in the discussion, there is an additional theoretical result worth reviewing, known as **Céa's Lemma** [54]. For coercive problems, this result shows that the approximation error of a Galerkin method is controlled by the error associated with the approximation of \mathcal{S} by \mathcal{S}^h , and a stability constant that involves the continuity and coercivity constants.

Lemma (Céa) 7.1.4. *Let $a(\cdot, \cdot)$ be a continuous, α -coercive bilinear form on $X \times X$ where X is a Hilbert space with norm $\|\cdot\|_X$. If c is the solution of (7.4) and c^h is the solution of (7.15), then*

$$\|c - c_h\|_X \leq \frac{\|a\|}{\alpha} \inf_{c^h \in X_h} \|c - c^h\|_X. \quad (7.16)$$

Remark 7.1.5. *Lemma 7.1.4 illustrates the fundamental difficulty in solving the advection-diffusion equation (1.2) by a numerical method in the advection-dominated (high Péclet) regime. One can infer the continuity and coercivity constants for this equation from (7.12) and (7.13) respectively. It follows that, when $\|\mathbf{a}\|_\infty \gg \kappa$, the*

constant appearing in the estimate (7.16) is of the form

$$\frac{\|a\|}{\alpha} = \frac{C_\Omega \|\mathbf{a}\|_\infty}{\kappa} \gg 1. \quad (7.17)$$

It is because the magnitude of this constant is so large in the high Péclet regime that poor numerical results from the classical Galerkin FEM are observed. One way to improve the accuracy of this method is through the addition to the variational equation (7.4) a stabilization term (Section 7.1.2).

Discretization and matrix equation

Suppose the domain has been discretized into a finite set of elements domains Ω^e , as shown in Figure 2.1, for $1 \leq e \leq n^{el}$, each having n^{nodes} nodes. Let n^{np} denote the total number of nodes in the mesh, and let $\eta = \{1, 2, \dots, n^{np}\}$ denote the set of global node numbers. The value of the solution will be prescribed on some subset of these nodes, namely the nodes on Γ , where $c^h = g^h$ by the Dirichlet boundary condition. Letting $\eta_g \subset \eta$ denote the set of nodes at which the solution is prescribed (i.e., the nodes on the Dirichlet boundary Γ), the complement of η_g in η , namely $\eta - \eta_g$, is the set of nodes at which c^h is to be determined. In this notation, a typical member of \mathcal{V}^h is assumed to have the form

$$w^h(\mathbf{x}) = \sum_{A \in \eta - \eta_g} N_A(\mathbf{x}) c_A \in \mathcal{V}^h, \quad (7.18)$$

where $N_A(\mathbf{x})$ is the shape function associated with node number A and $c_A \in \mathbb{R}$. It is assumed that the shape functions $N_A(\mathbf{x})$ are linearly independent, i.e.,

$$w^h = 0 \quad \Leftrightarrow \quad c_A = 0 \quad \forall A \in \eta - \eta_g. \quad (7.19)$$

Similarly to (7.18), one can write

$$v^h(\mathbf{x}) = \sum_{A \in \eta - \eta_g} N_A(\mathbf{x}) d_A \in \mathcal{S}^h, \quad (7.20)$$

where $d_A \in \mathbb{R}$ is an unknown dof for $c(\mathbf{x})$ at node A , and

$$g^h(\mathbf{x}) = \sum_{A \in \eta_g} N_A(\mathbf{x})g_A, \quad g_A = g(\mathbf{x}_A). \quad (7.21)$$

Substituting (7.18), (7.20) and (7.21) into (7.15), since (7.15) must hold for all $c_A \in \mathbb{R}$, the following linear system is obtained:

$$\sum_{B \in \eta - \eta_g} a(N_A, N_B)d_B = (N_A, f) - \sum_{B \in \eta_g} a(N_A, N_B)g_B, \quad A \in \eta - \eta_g, \quad (7.22)$$

for $A \in \eta - \eta_g$. (7.22) can be written in matrix form as

$$\mathbf{Kd} = \mathbf{F}. \quad (7.23)$$

Isoparametric shape functions

It is desired that the shape functions $N_A(\mathbf{x})$ are defined such that, as the finite element mesh is refined, the approximated Galerkin solution converges to the exact solution. The basic convergence requirements desired of the shape functions (Smoothness, Continuity and Completeness) were itemized earlier in Section 2.1. As mentioned in Section 2.1, one class of common shape functions that satisfy these properties are the so-called *isoparametric* shape functions (Chapter 3 of [6]). An isoparametric transformation from a (potentially curved) element in (x, y) -space, to a straight-edged element in (ξ, η) -space (the *parent domain*) is defined by mappings of the form

$$x(\xi, \eta) = \sum_{a=1}^{n^{\text{nodes}}} N_a(\xi, \eta)x_a^e, \quad (7.24)$$

$$y(\xi, \eta) = \sum_{a=1}^{n^{\text{nodes}}} N_a(\xi, \eta)y_a^e, \quad (7.25)$$

where (x_a^e, y_a^e) are the coordinates of the nodes of the element in (x, y) -space (Figure 7.1). The finite element shape functions $N_a(\xi, \eta)$ are in practice defined in the *natural coordinates* (ξ, η) in the reference element $(-1, 1) \times (-1, 1)$, and the integrations

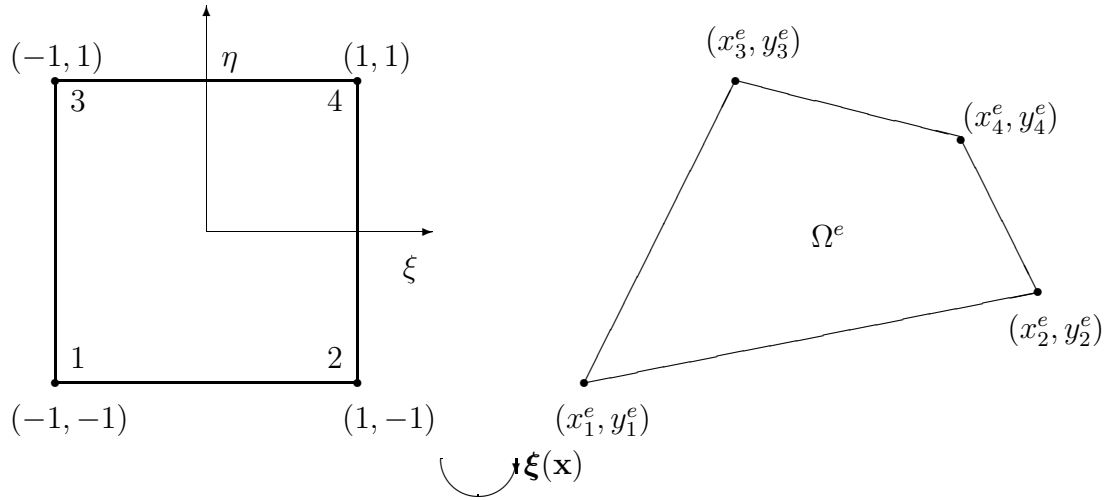


Figure 7.1: Bilinear quadrilateral element Q_1 domain and local node ordering in the parent domain (left) and in the physical domain (right)

appearing in the bilinear and linear forms are evaluated in these coordinates.

Attention is restricted in the present work to meshes of quadrilateral elements. An isoparametric quadrilateral finite element is denoted by Q_n . The integer n is a measure of the “order” of the element. Table 7.1 summarizes some properties of the Q_1, Q_2, Q_3 and Q_4 isoparametric quadrilateral finite elements. The second-to-last and last columns in this table give the standard error estimate of each of the elements, in the $H^0(\Omega) = L^2(\Omega)$ norm and the $H^1(\Omega)$ norms respectively (Chapter 4, [6]). Here, k is a constant independent of h and the solution c . The expected convergence rate is the exponent of h in these estimates.

Table 7.1: Summary of Galerkin quadrilateral isoparametric elements: notation and convergence properties

Notation	Name	n^{nodes}	$\ c - c^h\ _0$	$\ c - c^h\ _1$
Q_1	Bilinear Quadrilateral	4	$\leq kh^2 \ c\ _2$	$\leq kh \ c\ _2$
Q_2	Biquadratic Quadrilateral	9	$\leq kh^3 \ c\ _3$	$\leq kh^2 \ c\ _3$
Q_3	Bicubic Quadrilateral	16	$\leq kh^4 \ c\ _4$	$\leq kh^3 \ c\ _4$
Q_4	Biquartic Quadrilateral	25	$\leq kh^5 \ c\ _5$	$\leq kh^4 \ c\ _5$

Example 7.1.6. *As an example, the four shape functions that define the bilinear quadrilateral, or Q_1 , isoparametric element are given below, in the parent coordinate system*

$$N_1(\xi, \eta) = \frac{1}{4}(1 - \xi)(1 - \eta), \quad (7.26)$$

$$N_2(\xi, \eta) = \frac{1}{4}(1 + \xi)(1 - \eta), \quad (7.27)$$

$$N_3(\xi, \eta) = \frac{1}{4}(1 - \xi)(1 + \eta), \quad (7.28)$$

$$N_4(\xi, \eta) = \frac{1}{4}(1 + \xi)(1 + \eta). \quad (7.29)$$

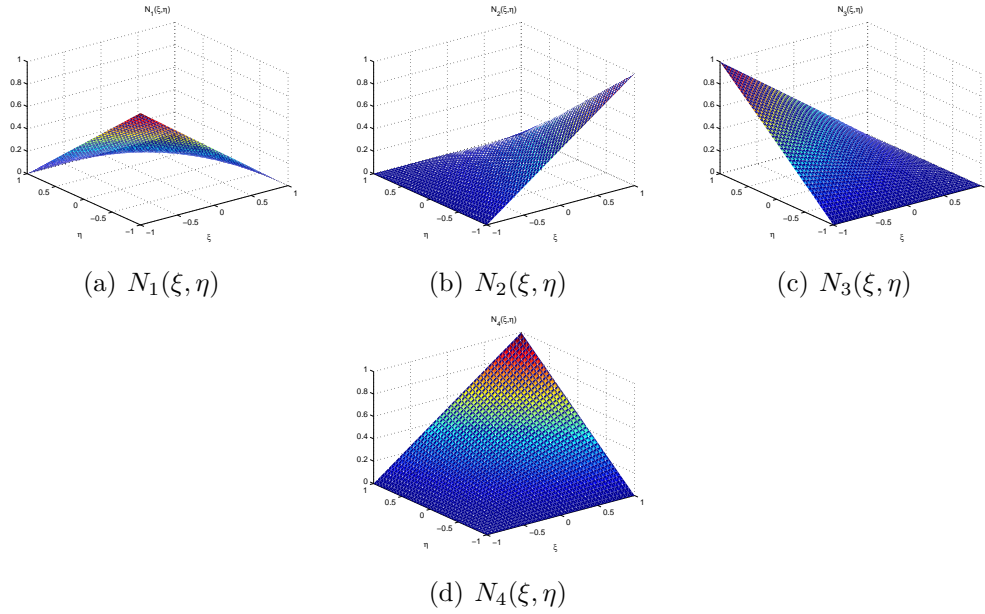
*These functions are plotted in Figure 7.2. Higher order shape functions can be constructed by taking products of one-dimensional Lagrange polynomials in the ξ and η directions. A **Lagrange polynomial** of degree d , which, by construction, satisfies $l_a(\xi_a) = 1$ if $b \neq a$ and $l_a(\xi_b) = 0$ otherwise, is defined by:*

$$l_a^d(\xi) = \frac{\prod_{b=1, b \neq a}^{d-1} (\xi - \xi_b)}{\prod_{b=1, b \neq a}^{d-1} (\xi_a - \xi_b)}. \quad (7.30)$$

7.1.2 Stabilized finite element methods

As discussed in the Introduction and Remark 7.1.5, the standard Galerkin FEM with low order piecewise polynomials performs poorly if the mesh size $h > \kappa$ [10]. More specifically, the standard Galerkin FEM produces central difference-type approximations in advection-dominated regimes. This phenomenon can be attributed to the loss of coercivity of the bilinear form $a(\cdot, \cdot)$ (7.5) when the Péclet number is high (Remark 7.1.5).

A common way to handle the difficulties encountered with the standard Galerkin method in this regime is by modifying the variational formulation (W) (7.4) by adding to it some numerical or artificial viscosity terms in a way that retains the weighted residual structure. This modification gives rise to the class of **stabilized finite**

Figure 7.2: Shape functions of the bilinear quadrilateral Q_1 element

element methods. Stabilized finite element methods have been studied since the 1980s. Some popular variants are:

- The *Streamline Upwind/Petrov-Galerkin (SUPG) method*, introduced by Hughes and Brooks [15, 72].
- The *Galerkin/Least-Squares (GLS) method* of Hughes, Franca and Hulbert [19].
- The *Unusual Stabilized Finite Element Method (USFEM)* of Franca *et al.* [1, 20].

Let \mathcal{V}^h be the discrete analog of (7.2) and let $v^h \in \mathcal{V}^h$. Now, rather than taking the $L^2(\Omega)$ inner product of (1.2) with $v^h \in \mathcal{V}^h$ as done in (7.3), take instead the inner product of (1.2) with $v^h + \tau^h \bar{\mathcal{L}}v^h$, where $\tau^h \in \mathbb{R}$ is some stability parameter, and $\bar{\mathcal{L}}$ is a differential operator (to be defined shortly) related to the operator governing the

problem (1.2)

$$\begin{aligned} \int_{\Omega} (\mathbf{a} \cdot \nabla c^h - \kappa \Delta c^h)(v^h + \tau^h \bar{\mathcal{L}}v^h) d\Omega &= \int_{\Omega} (\mathbf{a} \cdot \nabla c^h v^h + \kappa \nabla c^h \cdot \nabla v^h) d\Omega \\ &\quad - \underbrace{\kappa \int_{\Gamma} \nabla c^h \cdot \mathbf{n} v^h d\Gamma}_{=0 \text{ (since } v^h = 0 \text{ on } \Gamma)} + \tau^h \int_{\Omega} \mathcal{L}c^h \bar{\mathcal{L}}v^h d\Omega. \end{aligned} \quad (7.31)$$

(7.31) is of the form

$$a(c^h, v^h) + \tau^h(\mathcal{L}c^h, \bar{\mathcal{L}}v^h), \quad (7.32)$$

so that the Galerkin equation for the new stabilized finite element method is

$$a(c^h, v^h) + \tau^h(\mathcal{L}c^h, \bar{\mathcal{L}}v^h) = (f, v^h) + \tau^h(f, \bar{\mathcal{L}}v^h). \quad (7.33)$$

The class of methods defined by (7.33) are known as **residual methods**, due to the presence of the weighted residual term $(\mathcal{L}c^h - f, \bar{\mathcal{L}}v^h)$ in (7.33). Remark that if c^h in (7.33) is replaced with c , namely the exact solution to (1.2), the expression (7.33) reduces exactly to the Galerkin equation of the standard FEM (7.15), since $\mathcal{L}c - f = 0$.

Different stabilized methods are obtained by changing the definition of the differential operator $\bar{\mathcal{L}}$. In particular, for the SUPG, GLS and USFEM, this operator is defined respectively by [16]:

$$\bar{\mathcal{L}} \equiv \begin{cases} \mathbf{a} \cdot \nabla, & \text{SUPG [19],} \\ \mathcal{L}, & \text{GLS [15],} \\ \kappa \Delta + \mathbf{a} \cdot \nabla, & \text{USFEM [20].} \end{cases} \quad (7.34)$$

Remark 7.1.7. *The definitions of $\bar{\mathcal{L}}$ (7.34) differ in the treatment of the diffusive term $\kappa \Delta v^h$. Note that in the case of bilinear finite element shape functions, $\Delta v^h = 0$, so that all three methods (7.34) are identical.*

Remark 7.1.8. *For (7.33) to be defined, the definition of the spaces \mathcal{V}^h and \mathcal{S}^h need to be modified such that the term $(\Delta c^h, \bar{\mathcal{L}}v^h)$, which contains second order derivatives, is defined.*

Various approaches for selecting the value of the stability parameter τ^h have been proposed. For example, τ^h is typically chosen to be [19]

$$\tau^h = \begin{cases} \mathcal{O}\left(\frac{h}{|\mathbf{a}|}\right), & \text{if } Pe_h \gg 1, \\ \mathcal{O}\left(\frac{h^2}{\kappa}\right), & \text{if } Pe_h \ll 1, \end{cases} \quad (7.35)$$

where h is a characteristic length associated with a typical element Ω^e , and Pe_h denotes the local element Péclet number, defined by

$$Pe_h \equiv \frac{|\mathbf{a}|h}{2\kappa}. \quad (7.36)$$

7.2 Free-space solutions to the constant-coefficient advection-diffusion equation in 3D

The angle-parameterized exponential enrichment functions (3.10) have three-dimensional (3D) analogs. In 3D, the advection-direction is specified by *two* angle parameters, denoted by $\theta^a \in [0, 2\pi)$, the **azimuth angle**, and $\varphi^a \in [0, \pi)$, the **inclination angle**, (similar to the two angle parameters that come up in the spherical coordinate system; Figure 7.3). Then, the advection coefficient vector is

$$\mathbf{a}^T = \left(a_1, a_2, a_3 \right) = |\mathbf{a}| \left(\sin \varphi^a \cos \theta^a, \sin \varphi^a \sin \theta^a, \cos \varphi^a \right). \quad (7.37)$$

The angles θ^a and φ^a are given, that is, they are inferred from the PDE being solved, like the 2D advection direction, referred to earlier as ϕ (Figure 4.2). By analogy to the 2D case, the enrichment basis for the 3D advection-diffusion equation is given by:

$$c^E(\mathbf{x}; \theta_i, \varphi_i) = e^{\left[\frac{a_1}{2\kappa} + \frac{|\mathbf{a}|}{2\kappa} \sin \varphi_i \cos \theta_i\right](x-x_{r,i})} e^{\left[\frac{a_2}{2\kappa} + \frac{|\mathbf{a}|}{2\kappa} \sin \varphi_i \sin \theta_i\right](y-y_{r,i})} e^{\left[\frac{a_3}{2\kappa} + \frac{|\mathbf{a}|}{2\kappa} \cos \varphi_i\right](z-z_{r,i})}. \quad (7.38)$$

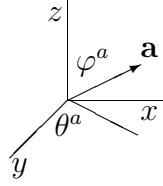


Figure 7.3: Azimuth and inclination angles specifying a 3D advection direction field $\mathbf{a} \in \mathbb{R}^3$

The angles $\theta_i \in [0, 2\pi)$ and $\varphi_i \in [0, \pi)$ are selected to generate a particular enrichment function, much like the angle θ_i in 2D:

$$\Theta^c \times \Phi^c \equiv \left\{ \{(\theta_i, \varphi_i)\}_{i=1}^{n^E} \in [0, 2\pi) \times [0, \pi) = \text{set of angles specifying } \mathcal{V}^E \text{ in 3D} \right\}. \quad (7.39)$$

One may verify that $\mathcal{L}c^E = \mathbf{a} \cdot \nabla c^E - \kappa \Delta c^E = 0$ for c^E given by (7.38) with $\mathbf{a} \in \mathbb{R}^3$ and for all angles θ_i and φ_i .

7.3 Free-space solutions to the 2D advection-diffusion equation with $\mathbf{a}(\mathbf{x}) = \mathbf{A}\mathbf{x} + \mathbf{b}$ and orthogonally diagonalizable \mathbf{A}

In this section, some additional free-space solutions to the 2D advection-diffusion equation in which $\mathbf{a}(\mathbf{x})$ is a linear function, that is

$$[\mathbf{A}\mathbf{x} + \mathbf{b}] \cdot \nabla c - \Delta c = 0, \quad (7.40)$$

are derived for the specific case when \mathbf{A} is orthogonally diagonalizable. In this case, the spectral decomposition of \mathbf{A} is

$$\mathbf{A}^T = \mathbf{S}\mathbf{D}\mathbf{S}^T, \quad \mathbf{S}\mathbf{S}^T = \mathbf{I}. \quad (7.41)$$

Substituting (7.41) into (7.40), gives

$$[\mathbf{S}\mathbf{D}\mathbf{S}^T\mathbf{x} + \mathbf{b}] \cdot \nabla c - \Delta c = 0. \quad (7.42)$$

where \mathbf{D} is a diagonal matrix containing the eigenvalues of \mathbf{A} , denoted by σ_1 and σ_2 . Define now the following transformation from \mathbb{R}^2 to \mathbb{R}^2 :

$$\mathbf{z} \equiv \mathbf{S}^T \mathbf{x}. \quad (7.43)$$

Then

$$\nabla_{\mathbf{x}} \equiv \nabla = \mathbf{S} \nabla_{\mathbf{z}}, \quad (7.44)$$

so that

$$\Delta_{\mathbf{x}} \equiv \Delta = \nabla_{\mathbf{x}} \cdot \nabla_{\mathbf{x}} = \nabla_{\mathbf{z}}^T (\underbrace{\mathbf{S}^T \mathbf{S}}_{\mathbf{I}}) \nabla_{\mathbf{z}} = \Delta_{\mathbf{z}}. \quad (7.45)$$

Writing (7.42) in the new coordinates (7.43),

$$[\mathbf{z}^T \mathbf{D} \mathbf{S}^T + \mathbf{b}^T] \mathbf{S} \nabla_{\mathbf{z}} c - \Delta_{\mathbf{z}} c = 0, \quad (7.46)$$

or

$$[\mathbf{z}^T \mathbf{D} + \mathbf{b}^T \mathbf{S}] \nabla_{\mathbf{z}} c - \Delta_{\mathbf{z}} c = 0. \quad (7.47)$$

Letting \mathbf{s}_1 and \mathbf{s}_2 denote the two columns of \mathbf{S} (the orthonormal eigenvectors of \mathbf{A})

$$\mathbf{S} \equiv \begin{pmatrix} \mathbf{s}_1 & \mathbf{s}_2 \end{pmatrix}, \quad (7.48)$$

(7.47) can be written as

$$[\sigma_1 z_1 + (\mathbf{s}_1 \cdot \mathbf{b})] c_{z_1} + [\sigma_2 z_2 + (\mathbf{s}_2 \cdot \mathbf{b})] c_{z_2} - [c_{z_1 z_1} + c_{z_2 z_2}] = 0. \quad (7.49)$$

Performing an additional change of variables,

$$\tilde{z}_1 \equiv \sigma_1 z_1 + (\mathbf{s}_1 \cdot \mathbf{b}), \quad \tilde{z}_2 \equiv \sigma_2 z_2 + (\mathbf{s}_2 \cdot \mathbf{b}), \quad (7.50)$$

(7.49) can be written as

$$\sigma_1 \tilde{z}_1 c_{\tilde{z}_1} + \sigma_2 \tilde{z}_2 c_{\tilde{z}_2} - \sigma_1^2 c_{\tilde{z}_1 \tilde{z}_1} - \sigma_2^2 c_{\tilde{z}_2 \tilde{z}_2} = 0. \quad (7.51)$$

(7.51) can be solved by separation of variables, that is by assuming a solution of the form:

$$c(\tilde{z}_1, \tilde{z}_2) = H(\tilde{z}_1)K(\tilde{z}_2), \quad (7.52)$$

for some $C^2(\mathbb{R})$ functions $H, K : \mathbb{R} \rightarrow \mathbb{R}$. Substituting (7.52) into (7.51), the following is obtained:

$$\frac{\sigma_1 \tilde{z}_1 H' - \sigma_1^2 H''}{H} + \frac{\sigma_2 \tilde{z}_2 K' - \sigma_2^2 K''}{K} = 0, \quad (7.53)$$

so that H and K satisfy the following ODEs, for some constant $m \in \mathbb{R}$,

$$\sigma_1^2 H'' - \sigma_1 \tilde{z}_1 H' + mH = 0, \quad (7.54)$$

$$\sigma_2^2 K'' - \sigma_2 \tilde{z}_2 K' - mK = 0. \quad (7.55)$$

Assume $\sigma_1, \sigma_2 \neq 0$. Then (7.54)–(7.55) are equivalent to:

$$H'' - \frac{1}{\sigma_1} \tilde{z}_1 H' + \frac{m}{\sigma_1^2} H = 0, \quad (7.56)$$

$$K'' - \frac{1}{\sigma_2} \tilde{z}_2 K' - \frac{m}{\sigma_2^2} K = 0. \quad (7.57)$$

The general free-space solution to ODEs of the form

$$c'' + axc' + bc = 0, \quad (7.58)$$

for constants a and b are

$$c = C_1 \Phi\left(\frac{b}{2a}, \frac{1}{2}, -\frac{1}{2}ax^2\right), \quad (7.59)$$

where $\Phi(a, b; x)$ are *degenerate hypergeometric functions* (also known as **Kummer functions**) (p. 216, case 20 of [73]). These functions are defined as the following

series:

$$\Phi(a, b; z) \equiv 1 + \frac{a}{b}z + \frac{a(a+1)}{b(b+1)}\frac{z^2}{2!} + \cdots = \sum_{k=0}^{\infty} \frac{(a)_k}{(b)_k} \frac{z^k}{k!}, \quad (7.60)$$

where $(x)_k$ denotes the *Pochhammer symbol*, given by the recursive relation

$$\begin{aligned} (x)_0 &\equiv 1, \\ (x)_n &\equiv (x)_{n-1}(x+n-1), \quad n = 1, 2, \dots \end{aligned} \quad (7.61)$$

It follows that the solutions to (7.56) and (7.57) are

$$H(z_1) = C_1 \Phi \left(-\frac{m}{2\sigma_1}, \frac{1}{2}, \frac{1}{2\sigma_1}(\sigma_1 z_1 + \mathbf{s}_1 \cdot \mathbf{b})^2 \right), \quad (7.62)$$

$$K(z_2) = C_2 \Phi \left(\frac{m}{2\sigma_2}, \frac{1}{2}, \frac{1}{2\sigma_2}(\sigma_2 z_2 + \mathbf{s}_2 \cdot \mathbf{b})^2 \right), \quad (7.63)$$

respectively, or, transforming back to the (x, y) coordinates,

$$H(\mathbf{x}) = C_1 \Phi \left(-\frac{m}{2\sigma_1}, \frac{1}{2}, \frac{1}{2\sigma_1}(\sigma_1 \mathbf{s}_1 \cdot \mathbf{x} + \mathbf{s}_1 \cdot \mathbf{b})^2 \right), \quad (7.64)$$

$$K(\mathbf{x}) = C_2 \Phi \left(\frac{m}{2\sigma_2}, \frac{1}{2}, \frac{1}{2\sigma_2}(\sigma_2 \mathbf{s}_2 \cdot \mathbf{x} + \mathbf{s}_2 \cdot \mathbf{b})^2 \right), \quad (7.65)$$

so that

$$c(\mathbf{x}) = \Phi \left(-\frac{m}{2\sigma_1}, \frac{1}{2}, \frac{1}{2\sigma_1}(\sigma_1 \mathbf{s}_1 \cdot \mathbf{x} + \mathbf{s}_1 \cdot \mathbf{b})^2 \right) \Phi \left(\frac{m}{2\sigma_2}, \frac{1}{2}, \frac{1}{2\sigma_2}(\sigma_2 \mathbf{s}_2 \cdot \mathbf{x} + \mathbf{s}_2 \cdot \mathbf{b})^2 \right). \quad (7.66)$$

The functions (7.66) can be parametrized with respect to an angle parameter by selecting, for instance,

$$m \equiv \sqrt{\sigma_1^2 + \sigma_2^2} \cos \theta_i, \quad (7.67)$$

for some angle $\theta_i \in [0, 2\pi)$. These functions are shown in Figure 7.4 as the parameter θ_i is varied for a sample BVP.

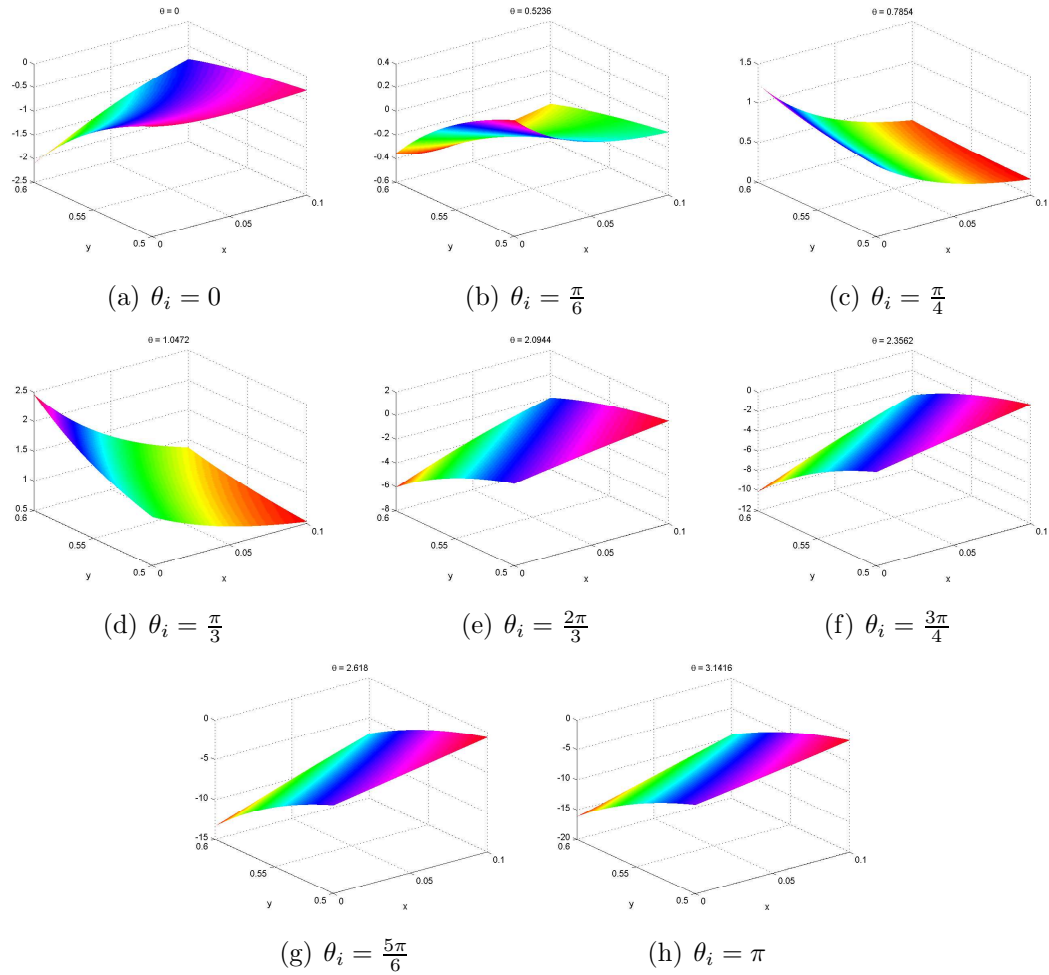


Figure 7.4: Plots of free-space solutions to (7.40) of the form (7.66) for different values of θ_i

7.4 Free-space solutions to the unsteady 2D constant-coefficient advection-diffusion equation

Consider the unsteady, constant coefficient advection-diffusion equation:

$$\frac{\partial u}{\partial t} + a_1 \frac{\partial u}{\partial x} + a_2 \frac{\partial u}{\partial y} - \kappa \left[\frac{\partial^2 u}{\partial x^2} + \frac{\partial^2 u}{\partial y^2} \right] = 0, \quad (7.68)$$

for $a_1, a_2, \kappa \in \mathbb{R}$, and $\kappa > 0$. It is possible to derive exponential free-space solutions to (7.68) that can be parameterized with respect to an angle parameter $\theta_i \in [0, 2\pi)$, similar to the exponential free-space solutions to the steady advection-diffusion equation (4.1).

Let $u = U(\xi, \eta, t)$ where

$$\xi \equiv x - a_1 t, \quad \eta \equiv y - a_2 t. \quad (7.69)$$

Then, by the chain rule,

$$\begin{aligned} \frac{\partial u}{\partial t} &= \frac{\partial U}{\partial t} + \frac{\partial U}{\partial \xi} \frac{\partial \xi}{\partial t} + \frac{\partial U}{\partial \eta} \frac{\partial \eta}{\partial t} \\ &= \frac{\partial U}{\partial t} - a_1 \frac{\partial U}{\partial \xi} - a_2 \frac{\partial U}{\partial \eta}, \end{aligned} \quad (7.70)$$

$$\frac{\partial u}{\partial x} = \frac{\partial U}{\partial \xi}, \quad \frac{\partial u}{\partial y} = \frac{\partial U}{\partial \eta}. \quad (7.71)$$

Substituting (7.70) and (7.71) into (7.68), the following heat equation for U is obtained:

$$\frac{\partial U}{\partial t} = \kappa \left[\frac{\partial^2 U}{\partial \xi^2} + \frac{\partial^2 U}{\partial \eta^2} \right]. \quad (7.72)$$

(7.72) is now solved using separation of variables. Assume a solution of the form

$$U(\xi, \eta, t) = T(t)Z(\xi, \eta). \quad (7.73)$$

Substituting (7.73) into (7.72), yields

$$\frac{1}{\kappa} T'(t)Z(\xi, \eta) = T(t) [Z_{\xi\xi} + Z_{\eta\eta}] \equiv -\lambda^2, \quad (7.74)$$

for some $\lambda \in \mathbb{R}$ (separation of variables constant, to be parameterized shortly). Dividing (7.74) by T and Z we obtain the following ODE for $T(t)$ and PDE for $Z(\xi, \eta)$:

$$T'(t) + \lambda^2 \kappa T(t) = 0, \quad (7.75)$$

$$Z_{\xi\xi} + Z_{\eta\eta} = -\lambda^2 Z. \quad (7.76)$$

It is straightforward to solve (7.75) for $T(t)$ (up to a multiplicative constant):

$$T(t) = e^{\lambda^2 \kappa t}. \quad (7.77)$$

To solve (7.76), again assume a separation of variables solution:

$$Z(\xi, \eta) = X(\xi)Y(\eta). \quad (7.78)$$

Substituting (7.78) into (7.76), gives

$$X''Y + XY'' = -\lambda^2 XY, \quad (7.79)$$

or

$$\frac{X''}{X} = -\left(\lambda^2 + \frac{Y''}{Y}\right) \equiv \mu^2, \quad (7.80)$$

for some $\mu \in \mathbb{R}$. Solving (7.80) for $X(\xi)$ and $Y(\eta)$ gives

$$X(\xi) = e^{\mu\xi}, \quad (7.81)$$

and

$$Y(\eta) = e^{\sqrt{\lambda^2 - \mu^2}\eta}. \quad (7.82)$$

Putting everything together, the solution to (7.72) is:

$$U(\xi, \eta, t) = \exp\left\{\lambda^2 \kappa t + \mu\xi + \eta\sqrt{\lambda^2 - \mu^2}\right\}. \quad (7.83)$$

The constants μ and λ can now be specified. Note that the argument of (7.83) is of the form:

$$A\xi + B\eta + (A^2 + B^2)t \quad (7.84)$$

with $A = \mu$ and $B = \sqrt{\lambda^2 - \mu^2}$. This motivates the introduction of an angle parameter θ , as for the steady advection-diffusion equation, and the definition

$$\mu \equiv k \cos \theta, \quad \sqrt{\lambda^2 - \mu^2} \equiv k \sin \theta \quad (7.85)$$

For some constant $k \in \mathbb{R}$. Substituting (7.85) and then (7.69) into (7.83), the angle-parametrized solutions to (7.68) are obtained:

$$u(x, y, t; \theta) = \exp \{ k^2 \kappa t + (k \cos \theta)(x - a_1 t) + (k \sin \theta)(y - a_2 t) \}. \quad (7.86)$$

The functions (7.86) are free-space solutions to (7.68) for any angle $\theta \in [0, 2\pi)$.

Given the availability of free-space solutions to the unsteady advection-diffusion equation (7.68), one may formulate a space-time discontinuous Galerkin (DG) method for this equation, in the same spirit of the method presented in [74] for the wave equation. Some useful references for this are [75, 76]. An interesting future research avenue would be to compare the performance of this space-time DEM for (7.68) with the performance of a space-only DEM, in which a semi-discrete form of (7.68) is obtained by discretizing (7.68) in space only and the resulting semi-discrete system is advanced forward in time using a time-integration scheme.

Bibliography

- [1] C. Farhat, I. Harari, and L.P. Franca. The discontinuous enrichment method. *Comput. Meth. Appl. Mech. Engng.*, 190:6455–2479, 2001.
- [2] C. Canuto, M.Y. Hussaini, A. Quarteroni, and T.A. Zang. *Spectral Methods: Fundamentals in Single Domains*. Springer-Verlag, Berlin, Germany, 2006.
- [3] C. Canuto, M.Y. Hussaini, A. Quarteroni, and T.A. Zang. *Spectral Methods: Evolution to Complex Geometries and Applications to Fluid Dynamics*. Springer-Verlag, Berlin, Germany, 2007.
- [4] J.C. Strikwerda. *Finite Difference Schemes and Partial Differential Equations (2nd Edition)*. SIAM, Philadelphia, PA, 2004.
- [5] R.J. LeVeque. *Finite Volume Methods for Hyperbolic Problems*. Cambridge University Press, Cambridge, UK, 2002.
- [6] T.J.R. Hughes. *The Finite Element Method: Linear Static and Dynamic Finite Element Analysis*. Dover Publications, Inc., Mineola, NY, 2000.
- [7] J. Donea and A. Huerta. *Finite Element Methods for Flow Problems*. John Wiley & Sons Ltd., West Sussex, England, 2003.
- [8] O.C. Zienkiewicz, R.L. Taylor, and P. Nathiarasu. *The Finite Element Method for Fluid Dynamics (5th Edition)*. McGraw-Hill, Woburn, MA, 2000.
- [9] D.L. Logan. *A first course in the finite element method*. Cengage Learning, 2007.

- [10] C. Johnson. *Numerical Solution of Partial Differential Equations by the Finite Element Method*. Dover Publications, Inc., Mineola, New York, 2009.
- [11] J.L. Guermond, P. Mineev, and J. Shen. An overview of projection methods for incompressible flow. *Comput. Methods Appl. Mech. Engrg.*, 195:6011–6045, 2006.
- [12] F. Brezzi and M. Fortin. *Mixed and Hybrid Finite Element Methods*. Springer-Verlag New York, Inc., New York, NY, 1991.
- [13] A. Novikov, G. Papanicolaou, and L. Ryzhik. Boundary layers for cellular flows at high pecelet numbers. *Comm. Pure Appl. Math*, 58(7):867–922, 2005.
- [14] F. Brezzi, D. Marini, and A. Russo. Applications of the pseudo residual-free bubbles to the stabilization of convection-diffusion problems. *Comput. Meth. Appl. Mech. Engrg.*, 166:51–63, 1998.
- [15] A.N. Brooks and T.J.R. Hughes. Streamline upwind/Petrov-Galerkin formulations for convection dominated flows with particular emphasis on the incompressible navier-stokes equations. *Comput. Meth. Appl. Mech. Engrg.*, 32:199–259, 1982.
- [16] I. Harari, L.P. Franca, and S.P. Oliveira. Streamline design of stability parameters for advection-diffusion problems. *J. Comput. Phys.*, 171:115–131, 2001.
- [17] A. Corsini, F. Rispoli, and A. Santoriello. A quadratic Petrov-Galerkin formulation for advection-diffusion-reaction problems in turbulence modelling. *J. Comput. Appl. Mech.*, 5:237–249, 2004.
- [18] I. Harari and T.J.R. Hughes. Galerkin/least squares finite element methods for the reduced wave equation with non-reflecting boundary conditions in unbounded domains. *Comput. Methods Appl. Mech. Engrg.*, 98:411–454, 1992.
- [19] T.J.R. Hughes, L.P. Franca, and G.M. Hulbert. A new finite element formulation for computational fluid dynamics: VIII. The Galerkin/least-squares method for advective-diffusive equations. *Comput. Meth. Appl. Mech. Engrg.*, 73(2):173–189, 1989.

- [20] L.P. Franca, S.L. Frey, and T.J.R. Hughes. Stabilized finite element methods, I. Application to the advective-diffusive model. *Comput. Meth. Appl. Mech. Engng.*, 95:253–276, 1992.
- [21] L.P. Franca and C. Farhat. Bubble functions prompt unusual stabilized finite element methods. *Comput. Meth. Appl. Mech. Engng.*, 123:299–308, 1995.
- [22] B. Delsaute and F. Dupret. A conformal Petrov-Galerkin method for convection-dominated problems. *Int. J. Numer. Method. Fluids*, 56:1077–1984, 2008.
- [23] B. Delsaute and F. Dupret. A Petrov-Galerkin method for convection-dominated problems. In *IMACS 2005 World Congress*.
- [24] F. Brezzi and A. Russo. Choosing bubbles for advection-diffusion problems. *Math. Models Meth. Appl. Sci.*, 4(4):571–578, 1994.
- [25] I. Babuška and J.M. Melenk. The partition of unity method. *Int. J. Numer. Meth. Engng.*, 40:727–758, 1997.
- [26] J.M. Melenk and I. Babuška. The partition of unity method finite element method: Basic theory and applications. *Comput. Meth. Appl. Mech. Engng.*, 139:289–314, 1996.
- [27] T.J.R. Hughes. Multiscale phenomena: Green’s functions, the Dirichlet-to-Neumann formulation, subgrid scale models, bubbles and the origins of stabilized methods. *Comput. Methods Appl. Mech. Engng.*, 127:387–401, 1995.
- [28] I. Babuška, C.E. Baumann, and J.T. Oden. A discontinuous *hp* finite element method for diffusion problems: 1-d analysis. *Comput. Math. Appl.*, 37:103–122, 1999.
- [29] C.E. Baumann and J.T. Oden. A discontinuous *hp* finite element method for the Euler and Navier-Stokes equations. *Int. J. Numer. Meth. Fluids*, 31(1):79–95, 1999.

- [30] B. Cockburn and C.W. Shu. The local discontinuous Galerkin method for time dependent convection-diffusion systems. *SIAM J. Numer. Anal.*, 35(6):2440–2463, 1998.
- [31] N.C. Nguyen, J. Peraire, and B. Cockburn. An implicit high-order hybridizable discontinuous Galerkin method for linear convection-diffusion equations. *J. Comput. Phys.*, 228:3232–3254, 2009.
- [32] N.C. Nguyen, J. Peraire, and B. Cockburn. An implicit high-order hybridizable discontinuous Galerkin method for nonlinear convection-diffusion equations. *J. Comput. Phys.*, 228:8841–8855, 2009.
- [33] A. El-Zein. Exponential finite elements for diffusion-advection problems. *Int. J. Numer. Meth. Engng.*, 62:2086–2103, 2005.
- [34] E.H. Georgoulis, E. Hall, and P. Houston. Discontinuous Galerkin methods for advection-diffusion-reaction problems on anisotropically refined meshes. *SIAM J. Scient. Comput.*, 30(1):246–271, 2007.
- [35] T.J.R. Hughes, G. Scovazzi, and L.P. Franca. Multi-scale and stabilized methods, in: E. Stein, R. De Borst, T.J.R. Hughes (Eds.), *Encyclopedia of Computational Mechanics*, Vol. 3, Chapter 2, Wiley, 2004.
- [36] F. Brezzi, L.D. Marini, and P. Pietra. Two-dimensional exponential fitting and applications to drift-diffusion models. *SIAM J. Numer. Anal.*, 26(6):1342–1355, 1989.
- [37] L. Demkowicz and J. Gopalakrishnan. A class of discontinuous petrov-galerkin methods. ii. optimal test functions. *Numer. Methods Partial Diff. Equat.*, 27(1):70–105, 2011.
- [38] C. Farhat. A Lagrange multiplier based on divide and conquer finite element algorithm. *J. Comput. Syst. Engng.*, 2/3:149–256, 1991.
- [39] C. Farhat. A saddle-point principle domain decomposition method for the solution of solid mechanics problems, in: D.E. Keyes, T.F. Chan, G. Meurant, J.S.

- Scroggs, R.G. Voigt (Eds.), Fifth International Symposium on Domain Decomposition Methods for Partial Differential Equations, Norfolk, VA, 1991, Society for Industrial and Applied Mathematics (SIAM), Philadelphia, PA, 1992, pp. 271–292.
- [40] C. Farhat, J. Mandel, and F.-X. Roux. Optimal convergence properties of the FETI domain decomposition method. *Comput. Methods Appl. Mech. Engrg.*, 115(3):367–388, 1994.
- [41] C. Farhat and F.-X. Roux. A method of finite element tearing and interconnecting and its parallel solution algorithm. *Int. J. Numer. Methods Engrg.*, 32(6):1205–1227, 1991.
- [42] C.E. Baumann and J.T. Oden. A discontinuous hp finite element method for convection-diffusion problems. *Comput. Methods Appl. Mech. Engrg.*, 175(3/4):311–341, 1999.
- [43] J.T. Oden, I. Babuška, and C.E. Baumann. A discontinuous hp finite element method for diffusion problems. *J. Comput. Phys*, 146(2):491–519, 1998.
- [44] P. Mayer and J. Mandel. The finite ray element method for the Helmholtz equation of scattering: first numerical experiments, UCD/CCM Report 111, <http://www-math.cudenver.edu/jmandel/papers/index.html>, October 1997, Updated January 1998.
- [45] D. Wang, R. Tezaur, J. Toivanen, and C. Farhat. Overview of the discontinuous enrichment method, the ultra-weak variational formulation, and the partition of unity method for acoustic scattering in the medium frequency regime and performance comparisons (in press). *Int. J. Numer. Meth. Engng.*, 2011.
- [46] R. Tezaur and C. Farhat. Three-dimensional discontinuous Galerkin elements with plane waves and Lagrange multipliers for the solution of mid-frequency Helmholtz problems. *Int. J. Numer. Meth. Engng.*, 66:796–815, 2006.

- [47] C. Farhat, R. Tezaur, and J. Toivanen. A domain decomposition method for discontinuous Galerkin discretization of Helmholtz problems with plane waves and Lagrange multipliers. *Int. J. Numer. Methods Engng.*, 78:1513–1531, 2009.
- [48] R. Tezaur, L. Zhang, and C. Farhat. A discontinuous enrichment method for capturing evanescent waves in multi-scale fluid and fluid/solid problems. *Comput. Meth. Appl. Mech. Engng.*, 197:1680–1698, 2008.
- [49] P. Massimi, R. Tezaur, and C. Farhat. A discontinuous enrichment method for three-dimensional multiscale harmonic wave propagation problems in multi-fluid and fluid-solid media. *Int. J. Numer. Meth. Engng.*, 76:400–425, 2008.
- [50] L. Zhang, R. Tezaur, and C. Farhat. The discontinuous enrichment method for elastic wave propagation in the medium-frequency regime. *Int. J. Numer. Meth. Engng.*, 55:2086–2114, 2006.
- [51] I. Babuška, B.A. Scabo, and I.N. Katz. The p -version of the fem. *SIAM J. Numer. Anal.*, 18(3):515–545, 1981.
- [52] M. Amara, R. Djellouli, and C. Farhat. Convergence analysis of a discontinuous Galerkin method with plane waves and Lagrange multipliers for the solution of Helmholtz problems. *SIAM J. Numer. Anal.*, 47(2):1038–1066, 2009.
- [53] S.P. Oliveira. *Discontinuous Enrichment Methods for Computational Fluid Dynamics*. PhD thesis, University of Colorado, Denver, CO.
- [54] A. Ern and J.-L. Guermond. *Theory and Practice of Finite Elements*. Springer-Verlag New York, Inc., New York, NY, 2004.
- [55] I. Babuška. The finite element method with Lagrange multipliers. *Numerical Math.*, 20:179–192, 1973.
- [56] C. Farhat, I. Harari, and U. Hetmaniuk. A discontinuous Galerkin method with lagrange multipliers for the solution of Helmholtz problems in the mid-frequency regime. *Comput. Meth. Appl. Mech. Engng.*, 192:1389–1419, 2003.

- [57] C. Farhat, I. Kalashnikova, and R. Tezaur. A higher-order discontinuous enrichment method for the solution of high Peclet advection-diffusion problems on unstructured meshes. *Int. J. Numer. Meth. Engng.*, 81:604–636, 2010.
- [58] I. Kalashnikova, C. Farhat, and R. Tezaur. A discontinuous enrichment method for the solution of advection-diffusion problems in high Peclet number regimes. *Fin. El. Anal. Des.*, 45:238–250, 2009.
- [59] P. Knobloch and L. Tobiska. The p_1^{mod} element: a new nonconforming finite element for convection-diffusion problems. *SIAM J. Numer. Anal.*, 41(2):436–456, 2003.
- [60] F. Brezzi. On the existence, uniqueness and approximation of saddle point problems arising from Lagrange multipliers. *Revue Francaise d'Automatique Informatique Recherche Operationnelle*, 8-R2:129–151, 1978.
- [61] E. Kreyszig. *Advanced engineering mathematics, a self-contained introduction (Maple Computer Guide), 9th edition*. Wiley, Columbus, OH, 2006.
- [62] MATLAB version R2008b, Natick, MA, The MathWorks Inc., 2008.
- [63] L.P. Franca and F.N. Hwang. Refining the submesh strategy in the two-level finite element method: application to the advection-diffusion equation. *Int. J. Numer. Meth. Engng.*, 39:161–187, 2002.
- [64] M.S. Chong, A.E. Perry, and B.J. Cantwell. A general classification of three-dimensional flow fields. *Phys. Fluids*, 2(5):765–777, 1990.
- [65] L.P. Franca and S.P. Oliveira. Resolving boundary layers with the discontinuous enrichment method. *University of Colorado, Center for Computational Mathematics (CCM) Report*, May 2003.
- [66] J. Burkardt. Cavity flow: Driven cavity flow datasets. <http://people.sc.fsu.edu/~jburkardt/datasets/datasets.html>.

- [67] N. Spillane. Numerical Solving of Natural Convection Situations, Farhat Research Group (FRG) Technical Report, May 21, 2009.
- [68] C. Farhat, P. Geuzaine, and G. Brown. Application of a three-field nonlinear fluid-structure formulation to the prediction of the aeroelastic parameters of an F-16 fighter. *Comput. Fluids*, 32:3–29, 2003.
- [69] W. Aquino, J.C. Brigham, C.J. Earls, and N. Sukumar. Generalized finite element method using proper orthogonal decomposition. *Int. J. Numer. Meth. Engng.*, 79:887–906, 2009.
- [70] J.L. Guermond and L. Quartapelle. Calculation of incompressible viscous flows by an unconditionally stable projection FEM. *J. Comput. Phys.*, 132:12–33, 1997.
- [71] J.L. Guermond and L. Quartapelle. On the approximation of the unsteady Navier-Stokes equations by finite element projection methods. *Numer. Math.*, 80:207–238, 1998.
- [72] T.J.R. Hughes and A.N. Brooks. A multi-dimensional upwind scheme with no crosswind diffusion. *Applied Mechanics Division (AMD) Am. Soc. of Mech. Engineers, Finite Element Methods for Convection Dominated Flows*, T.J.R. Hughes, ed., 34:19–35, 1979.
- [73] A.D. Polyanin and V.F. Zaitsev. *Handbook of Exact Solutions for Ordinary Differential Equations, 2nd Edition*. Chapman & Hall, Boca Raton, FL, 2003.
- [74] S. Petersen, C. Farhat, and R. Tezaur. A space-time discontinuous Galerkin method for the solution of the wave equation in the time domain. *Int. J. Numer. Meth. Engng.*, 78:275–295, 2009.
- [75] D. Meidner and B. Vexler. Adaptive space-time finite element methods for parabolic optimization problems. *SIAM J. Control Optim.*, 46(1):116–142, 2007.

- [76] K. Eriksson, C. Johnson, and S. Larsson. Adaptive finite element methods for parabolic problems. VI. Analytic semigroups. *SIAM J. Numer. Anal.*, 35:1315–1325, 1998.